UNIVERSITY OF CALIFORNIA, SAN DIEGO

Modeling Upper Mantle Rheology with Numerical Experiments
and
Mapping Marine Gravity with Satellite Altimetry

A dissertation submitted in partial satisfaction of the
requirements for the degree Doctor of Philosophy
in Earth Sciences

by

Mara M. Yale

Committee in charge:

Professor Jason Phipps Morgan, Chair
Professor Steven C. Cande
Professor Katja Lindenberg
Professor David T. Sandwell
Professor Bradley T. Werner

1997

The dissertation of Mara M. Yale is approved, and it is acceptable in quality and form for publication on microfilm:

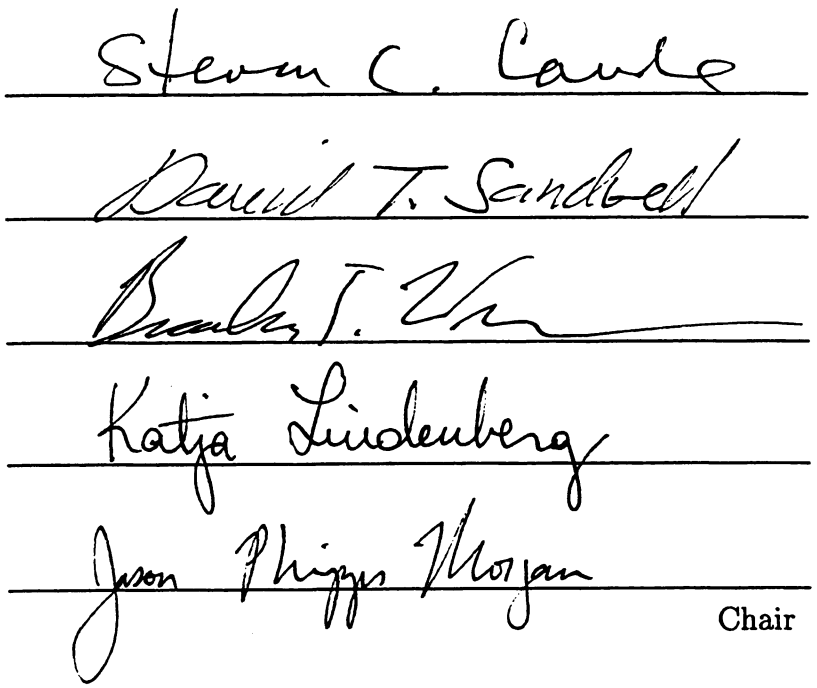

Chair

University of California, San Diego

1997

In memory of my father and Justin

Contents

List of Tables

List of Figures

ACKNOWLEDGMENTS

Jason Phipps Morgan and David Sandwell gave me the opportunity to pursue two separate fields of research. Marc Parmentier got me started and kept me going. The T-meter crew taught me much about field work and recreating. Donna Blackman reviewed Chapters 2 and 3. Jason Morgan helped sponsor my French sabbatical.

For Chapters 4 and 5, ERS-1/2 data were provided by the French Processing and Archive Facility, IFREMER-CERSAT, BP 70, 29280 Plouzane Cedex, France, TOPEX data were provided by AVISO, NASA, and CNES. John Lillibridge provided software to convert ERS-1/2 Altimeter Ocean PRoduct (OPR) data to NOAA-GDR data format. Chapter 4 benefited greatly from reviews by Richard Sailor, Gregory Neumann, and an anonymous reviewer. The research of Chapter 4 was supported by the NASA Global Geophysics Program NAGW-3035.

The text of Chapter 4, in full, is a reformatted version of the material as it appears in, Yale, M. M., D. T. Sandwell, and W. H. F. Smith, *Journal of Geophysical Research*, Vol. **100**, 15,117–15127, August 1995. I was the primary researcher and author, and David T. Sandwell and Walter H. F. Smith directed and supervised the research which forms the basis of Chapter 4.

Remko Scharroo and Delft Institute for Earth-Oriented Space Research provided ERS-1/2 orbits which were used in Chapter 5. Andrew Goodwillie shared his gravity profiles from the Pukapuka region.

My family put maps on the walls and gave me a global world view. Many healthy distractions were provided by friends and family around the world.

VITA

August 2, 1969	Born, Ithaca, New York
1991	B.S. Brown University
1991–1992	Field Geologist United States Geologic Survey
1992–1997	Research Assistant Scripps Institution of Oceanography University of California, San Diego
1997	Doctor of Philosophy University of California, San Diego

PUBLICATIONS

Yale, M.M., D.T. Sandwell, and W.H.F. Smith, 1995. Comparison of Along-Track Resolution of Stacked Geosat, ERS-1 and Topex Satellite Altimeters. *J. of Geophys. Res.*, **100**, 15,117-15,127.

Yale,M.M. and J. Phipps Morgan, 1997. Asthenosphere Flow Model of Hotspot-Ridge Interactions: a Comparison of Iceland and Kerguelen. *Earth and Plan. Sci. Lett.*, **submitted**.

Yale, M.M., A.T. Herring, D.T. Sandwell, 1997. What are the Limitations of Satellite Altimetry. *The Leading Edge*, **submitted**.

ABSTRACTS

Yale, M.M., and J. Phipps Morgan, 1996. Asthenosphere Flow Model of Hotspot-Ridge Interactions. *EOS, Trans., AGU*, **77**, F690.

Yale, M.M., and J. Phipps Morgan, 1996. Asthenosphere Flow Model of the North Atlantic. *FARA-InterRidge Mid-Atlantic Ridge Symposium Results from 15°N to 40°N*, **J. Conf. Abs. 1**, 868.

Yale, M.M., D.T. Sandwell and W.B. White, 1996. Southern Ocean mesoscale variability from 10 years of satellite altimetry. *EOS, Trans., AGU*, **77**, S79.

Yale, M.M., J. Phipps Morgan, and G. Zandt, 1995. Modeling Small-Scale Convective Instabilities in the Asthenosphere beneath California. *International Union of Geodesy and Geophysics XXI General Assembly*, **21**, A41.

Sandwell, D.T., M.M. Yale, D.C. McAdoo, W.H.F. Smith, 1995. Marine gravity from satellite altimetry over ocean and sea ice. *International Union of Geodesy and Geophysics, XXI General Assembly*, **21**, B43.

Sandwell, D.T., W.H.F. Smith, and M.M. Yale, 1994. ERS-1 Geodetic Mission Reveals Detailed Tectonic Structures. *EOS, Trans., AGU*, **75**, F155.

Yale, M.M., and D.T. Sandwell, 1994. Along-Track Resolution of Individual and Stacked ERS-1, Topex, and Geosat/ERM Profiles. *EOS, Trans., AGU*, **75**, S109.

Yale, M.M., and J. Phipps Morgan, 1993. Asthenosphere Channeling from Hotspots to Ridges?. *EOS, Trans., AGU*, **74**, F673.

Yale, M., T. MacDonald, and E.M. Parmentier, 1991. Thermal bending: a mechanism for the origin of the inside corner high and nodal deep at ridge-transform intersections. *EOS, Trans., AGU*, **72**, S261.

ABSTRACT OF THE DISSERTATION

Modeling Upper Mantle Rheology with Numerical Experiments

and

Mapping Marine Gravity with Satellite Altimetry

by

Mara M. Yale

Doctor of Philosophy in Earth Sciences

University of California, San Diego, 1997

Professor Jason Phipps Morgan, Chair

This thesis consists of modeling upper mantle rheology with numerical experiments and mapping marine gravity anomalies with satellite altimetry data. Chapter 1 introduces my reasoning for undertaking projects in two distinct fields. Chapters 2 and 3 are numerical modeling projects. Chapters 4 and 5 and the appendix are satellite altimetry projects.

Chapter 2 presents numerical modeling experiments of small-scale convection in the asthenosphere beneath California. Using the timing provided by the tectonic history and knowledge of the current thermal state from seismic tomography, our numerical experiments provide upper and lower bounds on the asthenosphere viscosity, and demonstrate the effects of rheologies that depend on temperature, pressure, and strain rate.

Chapter 3 presents a numerical model to test the asthenosphere flow paradigm in which hotspots feed the low viscosity asthenosphere, and lithosphere consumes the asthenosphere. The model is applied to two distinct regions - the Iceland hotspot centered on the Mid-Atlantic Ridge, and the Kerguelen hotspot located near the Southeast Indian Ridge. The asthenosphere flow paradigm can explain major features of hotspot-ridge interactions for both on-axis and off-axis hotspots.

Chapter 4 presents a resolution analysis of repeat satellite altimeter profiles to compare the along-track resolution capabilities of Geosat, ERS-1 and TOPEX data. On average globally, the along-track resolution (0.5 coherence) of eight-cycle stacks are approximately the same, 28, 29, and 30 km for TOPEX, Geosat, and ERS-1, respectively. TOPEX 31-cycle stacks (22 km) resolve slightly shorter wavelengths than Geosat 31-cycle stacks (24 km).

Chapter 5 presents a method to improve global gravity profiles by iterating on the current grid. We use new repeat cycle data to improve stacks (averages) for ERS-1/2 (43 cycles) and Topex (142 cycles), and then implement the method for improving gravity profiles globally. We demonstrate the maximum accuracy of our new grid by comparing the grid to ship profiles.

The appendix includes an analysis of the environmental corrections supplied with TOPEX data to evaluate which corrections may be important when using sea surface slope data for marine gravity and oceanographic variability studies.

Chapter 1

Introduction

Thoughts planted by "The Fossil Record," a course I took at Brown University from Thompson Webb III and John Imbrie, have formed much of the framework for how I think about doing science. I wrote a paper on the Milankovich cycle and Imbrie's discovery of the oxygen isotope record of long term climate change. The fundamental question was, "Which came first, theory or observations?" Other related questions concerned the biases inherent in any approach to science.

My first two experiences actually working to do science were at opposite ends of the theory-observation spectrum. At Brown, I worked for Marc Parmentier for 2 years mostly doing programming to build tools to attack problems in mantle convection. At the time, I had no idea how the models we were constructing related to the Earth. I think I took it on faith (respect for Marc and the scientific establishment) that there was a clear connection. After I left Brown, I worked for 6 months on a USGS field crew in Mammoth Lakes. There, we were collecting data from a 2 color laser geodimeter to monitor strain rates in the Long Valley Caldera. I was driving a 4WD truck around at night (when the instrument could operate) making these measurements. We sent the data by modem to Menlo Park, and our boss, John Langbein, processed it, and sent back plots of strain rate. I gained a great deal of appreciation for how to make careful, repeatable

field measurements, but didn't know what was involved in the data processing and interpretation.

I decided to go to graduate school largely because I wanted to reconcile these diverse experiences. It seemed to me that in order to make true scientific progress, theory and observation need to be in closer communication with each other. I've continued to work on both theoretical mantle convection problems, and on using geodetic methods to get a clearer picture of the Earth. Each time I shift gears from a theoretical to an observational project, I am reminded of how my thinking is influenced by the approach I am taking. My appreciation for the complexity of the world is much greater than it was when I was at Brown. I still believe that the most scientific progress occurs when people are working together to understand the world from different points of view.

My current deep question about science concerns the conflict between super-specialization and interdisciplinary collaboration. In order to do cutting edge work in any sub-field, intense specialization is required. Such a narrow focus makes many people unable to zoom out to see the big picture. Again, I think we need both, maybe not in every individual, but certainly in the community.

My thesis consists of roughly equal parts mantle convection modeling and creating gravity anomalies from satellite altimeter data.

Chapter 2

Modeling Small-scale Convective Instabilities in the Asthenosphere beneath California

2.1 Abstract

We have performed a series of 2 dimensional numerical experiments to study small-scale convection in the asthenosphere beneath California. Plate reconstructions in this region constrain the timing of the opening of a slab 'window' due to the northward migration of the Mendocino Triple Junction. Regional seismic tomographic inversions provide a snapshot of the current thermal structure of the upper mantle beneath California, showing several seismically fast 'fingers' that drip off from the lithospheric lid. Using the timing provided by the tectonic history and knowledge of the current thermal state, our numerical experiments provide upper and lower bounds on the asthenosphere viscosity, and demonstrate the effects of rheologies that depend on temperature, pressure, and strain rate. Our simulations generate cold downwellings within the upper mantle that are close in form to those observed in seismic tomographic images of the

region. Constant viscosity experiments suggest the viscosity of the upper mantle beneath California is $\sim 10^{19}$ Pa-s. Diffusion creep experiments demonstrate that flow law parameters derived in laboratory experiments create downwellings similar to those created for the constant viscosity experiments. We treat diffusion creep and dislocation creep as concurrent parallel processes, allowing the physical system to determine which creep mechanism dominates.

2.2 Introduction

California provides a unique natural laboratory for studying upper mantle convection. The tectonic history is relatively well known, and seismic tomography provides us with a snapshot of the current thermal state. The tectonic history of the western U.S. has been well studied [e.g. *Atwater*, 1970] and interpreted in terms of the thermal history beneath California [cf. *Dickinson and Snyder*, 1979, *Severinghaus and Atwater*, 1990]. The San Andreas fault began to form about 30 million years ago (Ma) when a section of the Pacific-Farallon mid-ocean ridge began to subduct beneath California. Prior to this, the entire coast of California was the site of subduction of the Farallon plate. As the Mendocino triple junction (point where the Pacific, North American and Gorda/Juan de Fuca plates meet) has migrated northward, the San Andreas Fault has lengthened to its present extent from the Salton Sea to Cape Mendocino. The sinking remnants of the Farallon plate are thought to have been replaced by hotter, upwelling asthenosphere. Seismic studies reveal that the upper mantle beneath the Western U.S. is anomalously slow seismically relative to a global average [*Laske and Masters*, 1996; *Anderson et al.*, 1992; *Van der Lee*, 1996], suggesting the presence of hot, possibly low viscosity upper mantle material. Regional seismic tomographic studies [*Benz, et al.*, 1992; *Biasi and Humphreys*, 1992; *Benz and Zandt*, 1993; *Humphreys and Clayton*, 1990; *Humphreys and Dueker*, 1994a; *Humphreys and*

Dueker, 1994b] show significant lateral variation in seismic velocity that have been interpreted as thermal anomalies related to small-scale convection [*Zandt and Carrigan*, 1993].

The upper mantle velocity structure beneath California includes several seismically fast fingers interpreted as cold downwelling blobs (Figure 2.1) [*Zandt and Carrigan*, 1993]. Features of the blobs that can be directly measured or inferred include the aspect ratio of the blobs, and the temperature contrast necessary to seismically image a blob if all of the compressional seismic velocity variation were due to temperature. In addition, the timing for the development of the blobs is constrained by the tectonic history and the tomographic images which imply that that blobs have reached at least 200 km depth within the last ~10-15 Ma. The viscous rheology controls the timing and the form that convection takes. Previous studies of upper mantle rheology include experimental studies of olivine deformation at high temperatures and pressures [*Karato and Wu*, 1993] and theoretical studies of post-glacial rebound in the western U.S. [*Bills, et al.*, 1994], Iceland [*Sigmundsson and Einarsson*, 1992], and elsewhere [*Cathles*, 1975].

We explore the effects of 3 different rheologies on the dynamics of small-scale convection beneath California. The first rheology consists of a layered viscosity structure, in which the cold lithosphere is 1000 times more viscous than the underlying asthenosphere. This allows us to bound the average asthenosphere viscosity, and serves as a reference for comparison with the more complicated rheologies. The second model rheology is diffusion creep, where the viscosity varies as a function of temperature, pressure, and grain size. The third and most complicated rheology is a combination of Newtonian diffusion creep and non-Newtonian dislocation creep, treated as concurrent parallel deformation mechanisms. The mechanism that produces the smallest viscosity dominates the flow locally.

2.3 Numerical Model

The numerical model used in this work is a 2D finite element viscous flow solver based on a penalty function method [*Reddy*, 1984], coupled with a finite difference technique for the advection and diffusion of heat [*Smolarkiewicz*, 1984]. The code was originally developed for studying mid-ocean ridge dynamics [*Jha and Parmentier*, 1995]. We have modified the code to study the dynamics of the upper mantle beneath California, incorporating several different rheologies.

The basic physical assumption is that hot asthenosphere has filled the slab gap created by the regional tectonic events [*Dickinson and Snyder*, 1979; *Severinghaus and Atwater*, 1990]. We model a 2D vertical slice running the length of California; properties are uniform in the third dimension. Our experiments all start from the same thermal state which includes a cold rigid lithosphere, and a hot asthenosphere. Initially, temperature varies as a function of depth (Figure 2.2), such that within the lithosphere there is a linear temperature gradient up to 800°C, and below the 800°C isotherm the entire asthenosphere has an initial temperature of 1325°C. This simple model allows us to explore how the asthenosphere rheology affects the form and dynamics of small-scale convection in this region, and to test non-linear viscous rheologies.

Boundary conditions for the top and bottom edges of the model box are no-slip (horizontal velocity = vertical velocity = 0) and temperature boundary conditions hold the temperature fixed at $T = T_{surface}$ for the top, and $T = T_{mantle}$ at the bottom. Both horizontal edges are symmetry planes where the free slip boundary condition is implemented by setting $(u = 0, dw/dx = 0)$, and $dT/dx = 0$. See Figure 2.3.

2.4 Rheology Theory

In the upper mantle, two deformation mechanisms are likely to be important - Newtonian diffusion creep and non-Newtonian dislocation creep. Lab experiments on olivine are performed at a range of temperatures and pressures, and the results are used to construct deformation mechanism maps [*Poirier*, 1985]. Lab experiments can bound transition curves between deformation mechanisms, but strain rates are limited to those measurable on human time scales, and must be extrapolated to geologic time scales. In the Earth, diffusion and dislocation creep may occur simultaneously within a crystal. *Gueguen and Darot* [1982] observed deformed samples of olivine with transmission electron microscopy and found evidence for both diffusion and dislocation creep which led the authors to propose the mechanisms act as concurrent parallel processes. We allow the local physical conditions in our model to determine which mechanism dominates at tectonic strain rates. Both mechanisms are temperature and pressure dependent, so for the initial temperature field used, the viscosity is high in the lithosphere, lowest at the lithosphere-asthenosphere boundary, and increases with depth as the pressure dependence dominates, Figure 2.4.

In order to implement variable viscosity within the numerical model, the viscosity must be expressed as a function of the local material properties including an assumed average grain size, and the physical state including the temperature, pressure, and stress. As we use the experimentally derived flow law parameters of *Karato and Wu* [1993], our notation follows theirs.

A general constitutive relation for polycrystalline flow is given by *Karato and Wu* [1993].

$$\dot{\varepsilon} = A \left(\frac{\sigma}{\mu}\right)^n \left(\frac{b}{d}\right)^m \exp\left[\frac{-(E+PV)}{RT}\right] \tag{2.1}$$

where $\dot{\varepsilon}$ is the strain rate, A is the preexponential factor, σ is the stress, μ is

the shear modulus (80 GPa), n is the stress exponent, b is the length of the Burgers vector (0.5 nm), d is the grain size, m is the grain-size exponent, E is the activation energy, V is the activation volume, P is the lithostatic pressure, R is the gas constant, and T is the temperature.

Within the finite element viscous flow code, we need to express the viscosity at each element in terms of local element properties. Transforming to a flow law in terms of invariants gives:

$$\sigma'_{ij} = \left\{ \sigma_E'^{(n-1)} A \left(\frac{1}{\mu}\right)^n \left(\frac{b}{d}\right)^m \exp\left[\frac{-(E+PV)}{RT}\right] \right\}^{-1} \dot{\varepsilon}_{ij} \tag{2.2}$$

where σ'_{ij} is the deviatoric stress tensor, $\dot{\varepsilon}_{ij}$ is the strain rate tensor, and the effective deviatoric stress of an element is the deviatoric stress invariant $\sigma'_E = 1/2(\sigma'_{ij}\sigma'_{ij})^{1/2}$.

Viscosity, $\eta = \sigma'_{ij}/\dot{\varepsilon}_{ij}$, can be written:

$$\eta = \sigma_E'^{(1-n)} A^{-1} (\mu)^n \left(\frac{d}{b}\right)^m \exp\left[\frac{E+PV}{RT}\right] \tag{2.3}$$

This expression for viscosity is adopted as it allows for either diffusion creep or dislocation creep, depending on the values used for the parameters. Diffusion creep is Newtonian ($n = 1$), in this case, the stress factor drops out of the viscosity expression. Dislocation creep is non-Newtonian ($n > 1$), and so the stress factor remains; but, the grain size exponent, $m = 0$, so the $(d/b)^m$ factor becomes 1.

It is likely that in the upper mantle either deformation mechanisms can dominate depending on physical conditions. If these two mechanisms are independent and simultaneously occur, then diffusion and dislocation creep can be considered to act as dashpots in series [*Poirier*, 1985]. The total strain rate is then just the sum of the two independent strain rates.

$$\dot{\varepsilon}_{total} = \dot{\varepsilon}_{diffusion} + \dot{\varepsilon}_{dislocation} \tag{2.4}$$

$$\dot{\varepsilon}_{diffusion} = \frac{\sigma}{\eta_{diffusion}} \tag{2.5}$$

$$\dot{\varepsilon}_{dislocation} = \frac{\sigma}{\eta_{dislocation}} \tag{2.6}$$

The net or effective viscosity is then given by summing the contributions from each rheology.

$$\eta_{effective} = \left[\frac{1}{\eta_{diffusion}} + \frac{1}{\eta_{dislocation}}\right]^{-1} \tag{2.7}$$

In this situation, the mechanism that gives the highest strain rate dominates creep. Figure 2.5 shows $\eta_{diffusion}$, $\eta_{dislocation}$, and $\eta_{effective}$ for the model initial state, assuming constant grain size (1 mm) and deviatoric stress (1 MPa). If stresses are small, then the dislocation creep viscosity will be large, and diffusion creep will dominate. Increasing the grain size increases the diffusion creep viscosity without changing the dislocation creep viscosity. In regions where both mechanisms give comparable viscosity, the series sum yields a smaller net viscosity than either mechanism acting alone.

The procedure for solving the viscous flow problem involves first specifying the initial temperature field to determine the viscosity structure. The viscous flow equations are then solved to determine the flow velocities including only thermal buoyancy forces. The flow velocities are used to solve the conservation of energy equations so that heat is diffused and advected, and the system advances in time. For the diffusion creep rheology, the new thermal state is used to calculate the current viscosity structure, and the procedure is repeated.

Implementing dislocation creep requires an iterative procedure at each time step because the viscosity depends on the flow. The viscosity at each node is estimated by the part of the viscosity that does not depend on stress, and flow is calculated. Then, the deviatoric stress invariant is determined from the flow at

each node, and the stress dependent part of the viscosity is calculated. The flow is calculated again based on the total viscosity, and the two step procedure is iterated to convergence, when the stresses and viscosity are self-consistent. After this stress-viscosity sub-iteration for each time step, the entire system is marched forward in time as in the case with only diffusion creep.

2.5 Results

Zandt and Carrigan [1993] used the local Rayleigh number to estimate the viscosity required to produce an instability in a given time in their flow calculations. In contrast, we specify the rheology and initial conditions and let the system evolve, which allows us to study the dynamics as blobs form. The cold lithosphere cools the top of the asthenosphere, creating a thermal boundary layer that grows into the asthenosphere. Initially imposed temperature perturbations propagate downward during this conduction phase. Once the boundary layer is thick enough that any of these temperature perturbations become unstable, the larger ones grow rapidly as sinking blobs. As a blob sinks, it generates shear forces on the base of the lithosphere that pull nearby smaller blobs toward the dominant downwelling. The width of the blobs is approximately twice the thickness of the boundary layer, and depends on asthenosphere viscosity. The results of experiments from three different rheologies are presented below with still images. To facilitate our understanding of the time-dependent dynamics, we have animated the simulations.

2.5.1 Constant Viscosity

We first performed a series of experiments using a constant viscosity structure, where $\eta_{lithosphere} = 1000\eta_{asthenosphere}$ to constrain the average viscosity of the upper mantle. This is analagous to the no-slip case for results presented by

Houseman and McKenzie [1982]. To seed the instabilities, the temperature of the top 2 rows of nodes within the asthenosphere are perturbed randomly with a 1% variation from 1325°C.

Four constant viscosity experiments with $\eta_{asthenosphere}$ ranging from 10^{18} Pa-s to 10^{21} Pa-s reveal many characteristics of blob development (Figure 2.6). The blob width increases with increasing $\eta_{asthenosphere}$. More blobs develop for the lower viscosity experiments than for the higher viscosity experiments. The time for blobs to reach ~200 km increases by a factor of 4-5 with each order of magnitude increase in $\eta_{asthenosphere}$. When $\eta_{asthenosphere} \geq 10^{21}$ Pa-s, as in Figure 2.6d, conduction persists and no asthenosphere blobs develop, placing a strong upper bound on the upper mantle viscosity beneath California. If the seismic tomography results actually represent such blob-like features that formed by thermal convection then the required asthenosphere viscosity is about 10^{19} Pa-s for instabilities to reach to 200 km within ~10 Ma. This conclusion is consistent with *Zandt and Carrigan's* [1993] analysis, and with viscosity estimates based on post glacial rebound for the Western U.S. [*Bills, et al.*, 1994], and Iceland [*Sigmundsson and Einarsson*, 1992], providing further support that the upper mantle beneath California has a viscosity significantly lower than that inferred beneath continental cratons [*Cathles*, 1975].

The lateral spacing between blobs is not well constrained by tomography because the finite size of the region limits the number of blobs. In our numerical experiments, we can ask if there is a characteristic spacing of blobs that varies as a function of viscosity. We experimented with many different random initial conditions, to ascertain if the number of blobs that form depends on viscosity rather than specific initial conditions. For different random temperature perturbations, with a range of amplitudes and distributions within the asthenosphere, we found consistent dynamics. Several blobs begin to form as the temperature perturbations propagate downward by conduction, the largest ones grow fast.

Smaller adjacent blobs are pulled toward their larger neighbors. Some of the blobs are perturbed laterally by these interactions, and blobs of comparable size merge. For many different random initial conditions, when $\eta_{asthenosphere} = 10^{19}$ Pa-s, four distinct downwellings fall to at least 200 km within a model box which is 128x48 nodes and has dimensions, 1270 km x 470 km.

Periodic initial conditions impose a fixed number of sinusoidal temperature perturbations to initiate blobs. We tried both perturbing only the top of the asthenosphere, and the entire asthenosphere, and found consistent results. Figure 2.7 shows the blobs resulting from 4, 8, and 16 initial wavelengths of temperature perturbation. In Figure 2.7a, 4 blobs form and fall vertically in the asthenosphere. In Figure 2.7b, 8 blobs form, but the structure of blobs is unstable because the edge blobs get a slight head start and then pull adjacent blobs toward themselves. Figure 2.7c shows the most unstable situation, where 16 blobs form initially, but the edge effects cause the blobs on the end to attract blobs one by one, leaving many blobs locked in the center. As the amplitude of perturbations was constant, none of the interior blobs starts with a competitive advantage over any others. Eventually, the edge blobs entrain all the blobs within their range of influence, and the interior blobs freeze, growing very slowly, until an avalanche occurs when there is enough negative buoyancy that one large downwelling forms from the many small blobs.

2.5.2 Diffusion Creep

A diffusion creep experiment illustrates how temperature and pressure influence asthenosphere blobs as they form and evolve (Figure 2.8). From the results of our constant viscosity experiments, we know that the viscosity of the upper mantle must be small enough that instabilities form, however *Karato and Wu's* [1993] value for $A_{diffusion}$ specifies a viscosity structure that generates blobs too slowly for our tectonic and tomographic constraints. Parame-

ters used are those derived experimentally for wet olivine by *Karato and Wu* [1993], but we multiply their $A_{diffusion}$ by 10, decreasing the viscosity by a factor of 10. Specifically, $A_{diffusion}$=5.3x10^{16} s^{-1}, $n_{diffusion}$=1, $d_{diffusion}$=1 mm, $m_{diffusion}$=2.5, $E_{diffusion}$=2.4x10^5 J/mol, and $V_{diffusion}$=5x10^{-6} m^3/mol. Initially, the vertical viscosity profile for these parameters is that of the dotted line on Figure 2.5. As cold blobs form and sink, their viscosity exceeds that of adjacent mantle, Figure 2.8b. Sinking blobs slow as they encounter more viscous material with increasing depth, which causes blobs to deflect laterally at shallower depths than they do for the constant viscosity experiments. The viscosity of the top of the asthenosphere determines the initiation of the instabilities, but the pressure dependence of viscosity controls how the blobs evolve.

2.5.3 Diffusion Creep + Dislocation Creep

We present results from an experiment that includes both diffusion creep and dislocation creep, treating the two mechanisms as concurrent parallel processes as described in the theory above. Parameters for diffusion creep are the same as those used for the pure diffusion creep experiment. Dislocation creep parameters also were taken from *Karato and Wu's* [1993] estimate for wet olivine rheology, but we multiply their $A_{dislocation}$ by 10 as for $A_{diffusion}$: $A_{dislocation}$=2.0x10^{19} s^{-1}, $n_{dislocation}$=3, $m_{dislocation}$=0, $E_{dislocation}$=4.3x10^5 J/mol, and $V_{dislocation}$=10x10^{-6} m^3/mol.

As for the pure diffusion creep experiment above, the cold core of blobs is more viscous than adjacent material (Figure 2.9b). Initially, stresses are small, so $\eta_{diffusion}$ dominates flow. When blobs begin to sink quickly, they generate large stresses at the base of the lithosphere and at depth where they are slowed by more viscous material (Figure 2.9c). When the stresses are large enough that $\eta_{dislocation}$ is as small as $\eta_{diffusion}$, dislocation creep is an effective flow mechanism in addition to diffusion creep. To map the regions where diffusion and dislocation

creep operate, we use the following viscosity ratio.

$$\eta_{ratio} = \log\left[\frac{\eta_{dislocation}}{\eta_{effective}}\right] \tag{2.8}$$

When $\eta_{diffusion} \ll \eta_{dislocation}$, $\eta_{ratio} > 1$; when $\eta_{diffusion} = \eta_{dislocation}$, $\eta_{ratio} = \log 2 = 0.3$; when $\eta_{diffusion} \gg \eta_{dislocation}$, $\eta_{ratio} = 0$. In Figure 2.9d, diffusion creep dominates in the red regions, while diffusion creep and dislocation creep are both equally active in the blue regions. There are few regions for this experiment where dislocation creep dominates the flow.

2.6 Discussion

The timing constraint from tomography and tectonics requires that blobs formed within the last 25 ma. As described above, the series of constant viscosity experiments suggests that the average asthenosphere viscosity must be $\sim 10^{19}$ Pa-s to satisfy the timing constraint. In our variable viscosity experiments, the asthenosphere viscosity varies as a function of depth and evolving flow patterns, such that the top of the asthenosphere has a viscosity as low as 10^{18} Pa-s and viscosity increases with depth. For both the pure diffusion creep rheology (Figure 2.8, 11.6 ma) and the combined diffusion creep and dislocation creep rheology (Figure 2.9, 14.8 ma), blobs fall to at least 200 km within the alotted time.

If thermal mechanisms are responsible for the formation of blobs imaged beneath California, the blobs must be large enough and cold enough with respect to ambient asthenosphere to be imaged seismically. End member scaling relationships between seismic velocity and temperature range from -0.5 $ms^{-1}°C^{-1}$ [*Anderson, et al.*, 1968] to -2.9 $ms^{-1}°C^{-1}$ [*Sato, et al.*, 1989]. These scalings suggest a 1% velocity anomaly in the upper mantle for temperature contrasts of 160°C and 28°C respectively. Constant viscosity experiments with $\eta_{asthenosphere} = 10^{19}$ Pa-s generate cold downwellings that are 100-125°C colder than adjacent mantle, im-

plying a maximum velocity anomaly of 0.7% and 4.5% for the two scalings. Variable viscosity experiments generate cold downwellings that have a much smaller temperature contrast with adjacent mantle, only 50-75°C, implying a maximum velocity anomaly of 0.5% to 2.7 % for the two scalings. Our results suggest that the appropriate scaling is closer to that of *Sato, et al.* [1989] for asthenosphere conditions. Variable viscosity results show that the temperature contrast between the blobs and ambient asthenosphere may be too small to account for the blobs that are imaged seismically, suggesting the blobs are not formed only by thermal mechanisms. Our experiments do not include surface plate motions, compositional or topographic variations on the lithosphere-asthenosphere boundary, but these factors would tend to focus the downwellings and enhance the temperature contrast [*Liu and Zandt*, 1996]. The pattern of flow generated by our numerical experiments could produce significant seismic anisotropy with fast seismic velocities aligned with maximum shear flow.

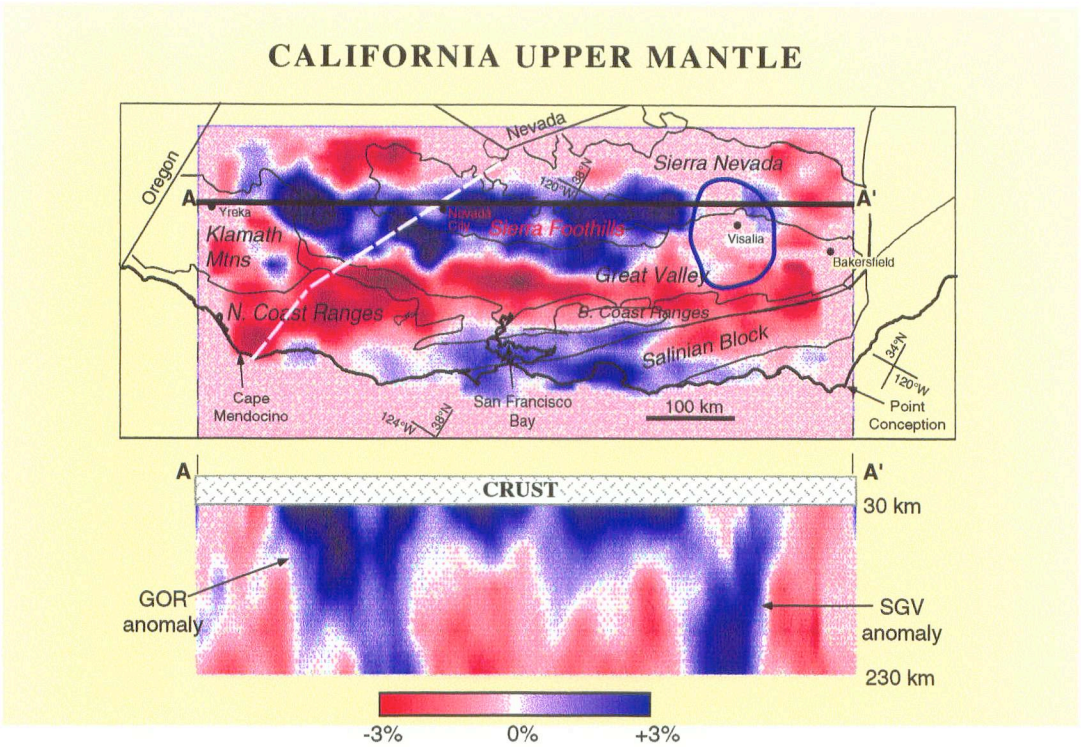

Figure 2.1: Seismic P-wave velocity anomalies in the upper mantle beneath California. In map view, dark solid lines outline major geologic provinces. The circle around Visalia represents the location and size of the Southern Great Valley (SGV) anomaly over the depth range of 150 to 190 km. The dashed white line extending from Cape Mendocino to Lake Tahoe (on the California-Nevada border) marks the southernmost extent of the subducting Gorda (GOR) plate. The cross section shows the depth extent of the GOR and SGV anomalies in the cross section AA'. Figure is based on results from *Benz and Zandt* [1993].

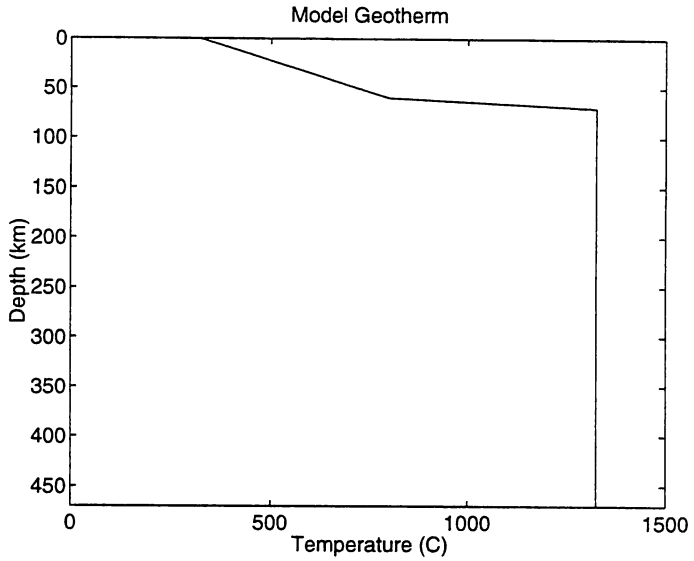

Figure 2.2: Model geotherm. All experiments start from this initial temperature state with a linear temperature gradient in the lithosphere, an abrupt temperature jump at the lithosphere-asthenosphere boundary, and constant temperature throughout the asthenosphere.

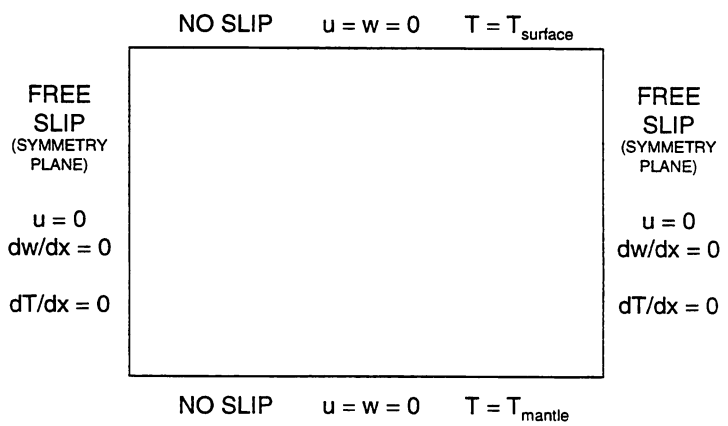

Figure 2.3: Velocity and temperature boundary conditions. Top and bottom boundaries are no slip surfaces with the temperature held constant. The side boundaries are symmetry planes for both velocity and temperature.

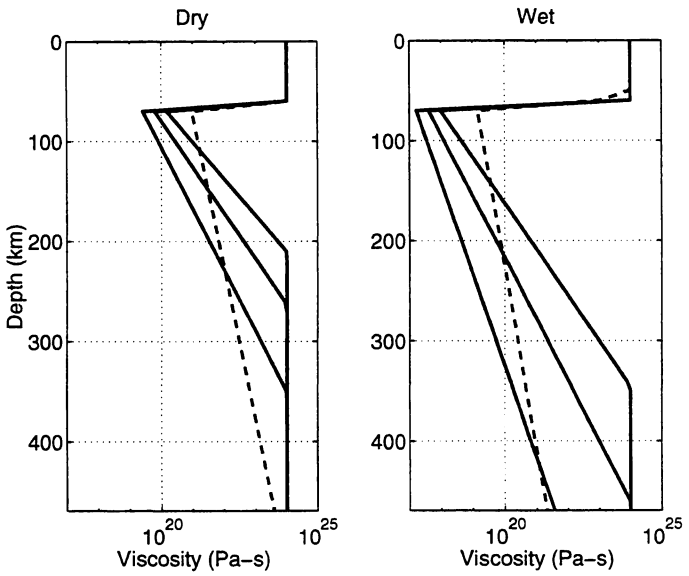

Figure 2.4: Viscosity as a function of depth for dry and wet olivine rheology, based on the flow law and parameters from *Karato and Wu* [1993], and calculated using our assumed geotherm. Dashed lines are diffusion creep viscosity. Solid lines are dislocation creep viscosity for a range of activation volumes (15, 20, $25 \times 10^{-6} m^3 mol^{-1}$ for dry and 10, 15, $20 \times 10^{-6} m^3 mol^{-1}$ for wet rheology). The reference grain size is 1 mm. The reference stress is 1 MPa.

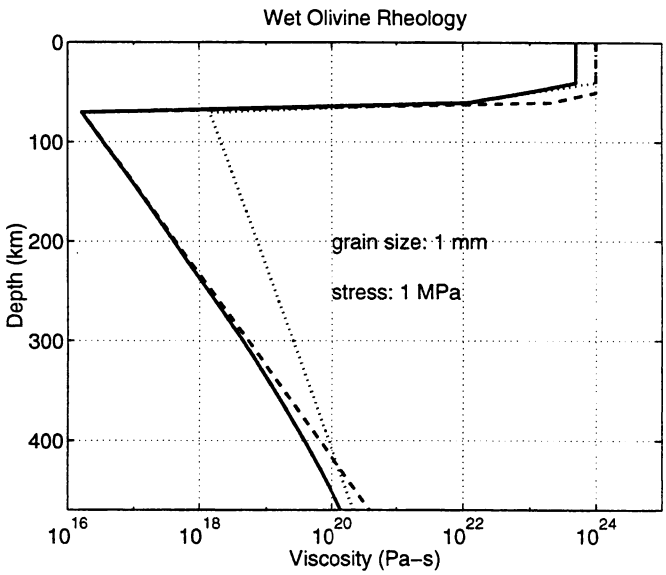

Figure 2.5: Viscosity as a function of depth for combined diffusion and dislocation creep rheology when the two mechanisms operate together as a pair of dashpots in series. The solid line is for $\eta_{effective}$, the dotted line is for $\eta_{diffusion}$, the dashed line is for $\eta_{dislocation}$. These curves were generated using our model geotherm and flow law parameters from *Karato and Wu* [1993], except that the preexponential factor, A, was multiplied by 10, decreasing the viscosity by a factor of ten. The grain size used here is 1 mm, the deviatoric stress is 1 MPa.

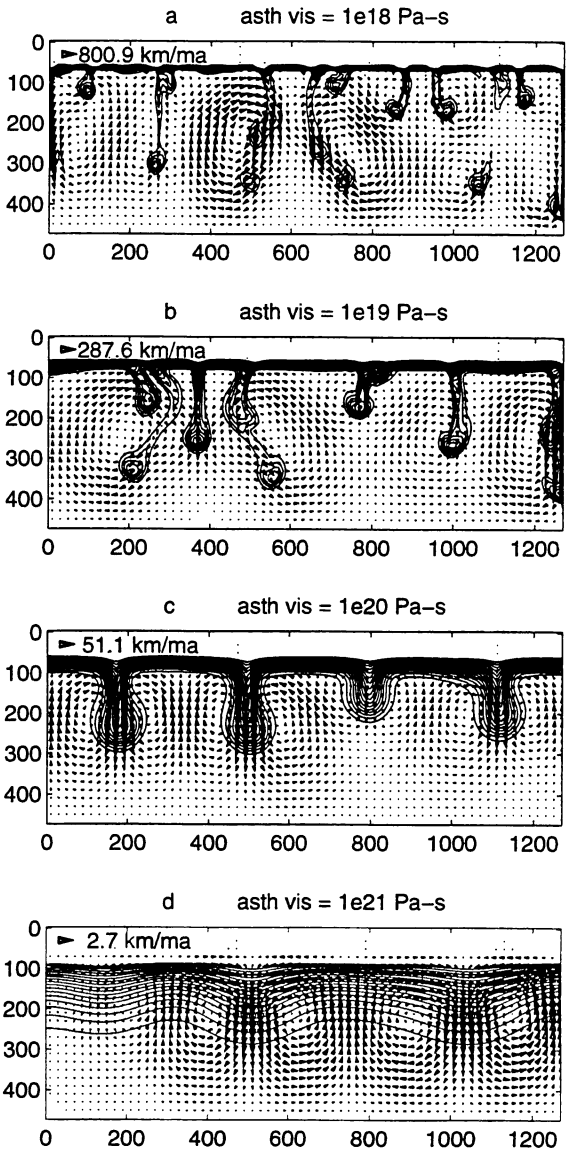

Figure 2.6: Constant viscosity experiments. For all plots, temperature contours range from 900°C to 1300°C with a contour interval of 25°C. Vector fields represent flow velocities at every other node in the computational grid. Initial conditions were the same for all 4 experiments. a) time=2 ma, $\eta_{asth} = 10^{18}$ Pa-s, $\eta_{lith} = 10^{21}$ Pa-s. b) time=10 ma, $\eta_{asth} = 10^{19}$ Pa-s, $\eta_{lith} = 10^{22}$ Pa-s. c) time=44 ma, $\eta_{asth} = 10^{20}$ Pa-s, $\eta_{lith} = 10^{23}$ Pa-s. d) time=167 ma, $\eta_{asth} = 10^{21}$ Pa-s, $\eta_{lith} = 10^{24}$ Pa-s.

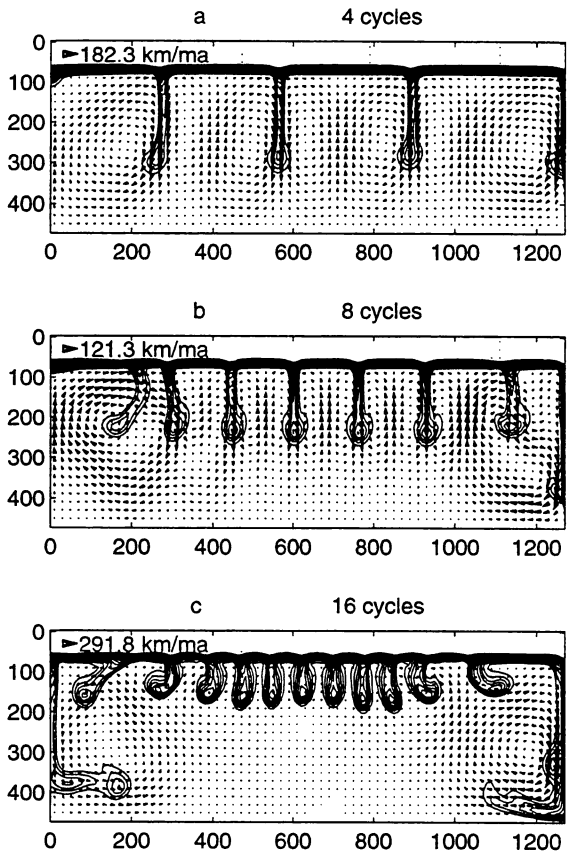

Figure 2.7: Constant viscosity, periodic initial perturbation experiments. Temperature contours and velocity field conventions are the same as for Figure 2.6. This series of experiments shows the downwellings that develop for a range of periodic initial temperature perturbations. The rheology is constant for all three experiments: $\eta_{asth} = 10^{19}$ Pa-s, $\eta_{lith} = 10^{22}$ Pa-s. a) time=4.8 ma, 4 cycles b) time=6.1 ma, 8 cycles c) time=11.7 ma, 16 cycles.

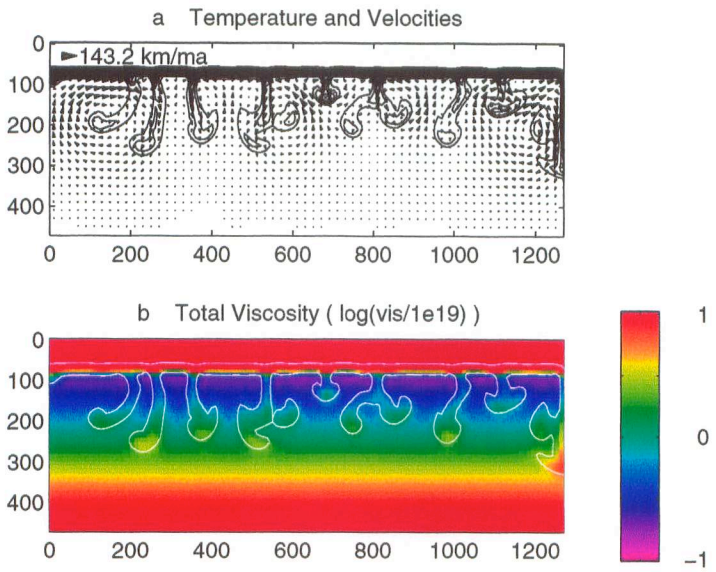

Figure 2.8: Diffusion creep rheology experiment, time=11.6 ma. a) Temperature contours and velocity field conventions are the same as for Figure 2.6. b) Viscosity - the downwelling blobs are colder and therefore more viscous than adjacent material. The range of viscosities plotted is limited to two orders of magnitude, ranging from $\eta \leq 10^{18}$ Pa-s to $\eta \geq 10^{20}$ Pa-s. For reference, the 800°C and 1300°C temperature contours are drawn in white.

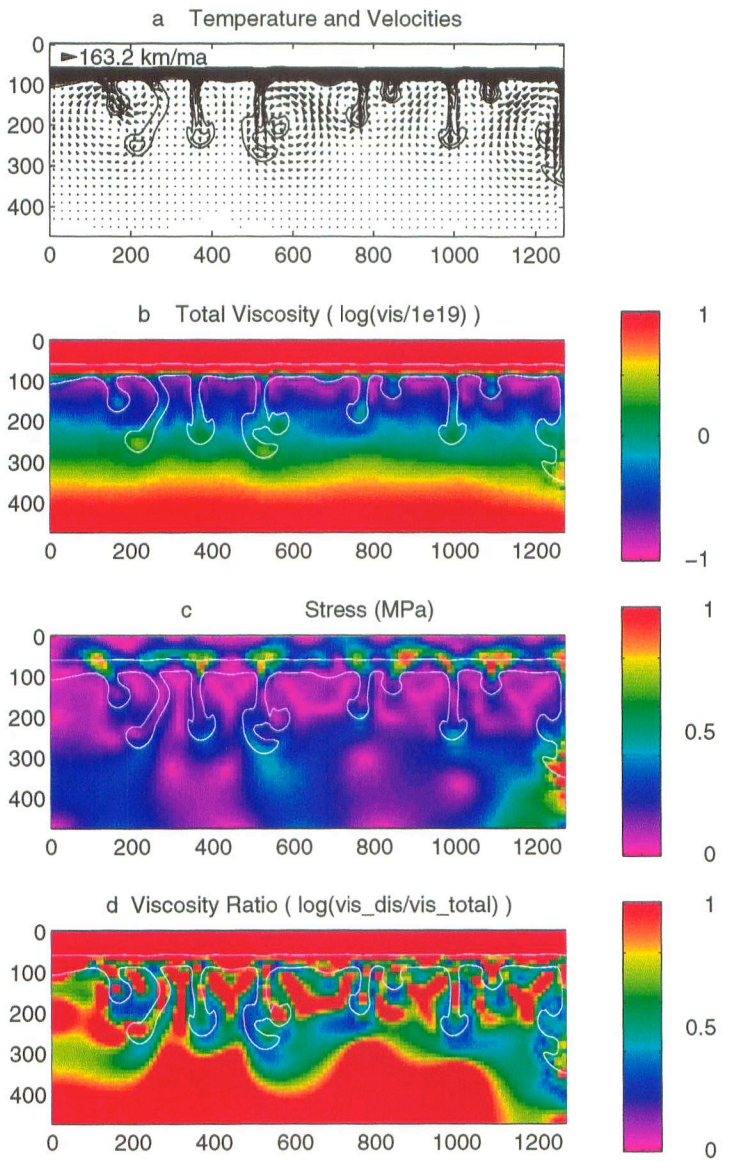

Figure 2.9: Combined diffusion and dislocation creep rheology experiment, time=14.8 ma. Plotting conventions are the same as for Figure 2.8. a) Temperature and velocity field. b) Total effective viscosity. c) Deviatoric stress invariant, $\sigma'_E = 1/2(\sigma'_{ij}\sigma'_{ij})^{1/2}$. d) Viscosity ratio, $\eta_{ratio} = \log[\eta_{dislocation}/\eta_{effective}]$, maps regions where diffusion creep and dislocation creep control the rheology as discussed in the text.

2.7 References

Anderson, D. L., T. Tanimoto and Y.-S. Zhang, 1992. Plate tectonics and hotspots: the third dimension. *Science*, **256**, 1645-1651.

Anderson, O. L., E. Schreiber, R. C. Lieberman, and N. Soga, 1968. Some elastic constant data on minerals relevant to geophysics. *Rev. Geophys.*, **6**, 491-524.

Atwater, T. M., 1970. Implications of plate tectonics for the Cenozoic tectonic evolution of western North America. *Geol. Soc. Amer. Bull.*, **81**, 3518-3536.

Benz, H. M. and G. Zandt, 1993. Teleseismic tomography; lithospheric structure of the San Andreas Fault system in northern and central California. In " *Seismic Tomography: theory and practice*", ed. H. M. Iyer and K. Hirahara, Chapman and Hall, pp. 440-465.

Benz, H. M., G. Zandt and D. H. Oppenheimer, 1992. Lithospheric Structure of Northern California from Teleseismic Images of the Upper Mantle. *J. Geophys. Res.*, **97**, 4791-4807.

Biasi, G. P. and E. D. Humphreys, 1992. P-Wave Image of the Upper Mantle Structure of Central California and Southern Nevada. *Geophys. Res. Lett.*, **19**, 1161-1164.

Bills, B. G., D. R. Currey and G. A. Marshall, 1994. Viscosity estimates for the crust and upper mantle from patterns of lacustrine shoreline deformation in the Eastern Great Basin. *J. Geophys. Res.*, **99**, 22,059-22,086.

Cathles, L. M., 1975. *The viscosity of the Earth's mantle.* Princeton University Press, Princeton, NJ.

Gueguen, Y., and M. Darot, 1982. Les dislocations dans la forstérite déformée à haute température. *Philos. Mag., A*, **45**, 419-442.

Dickinson, W. R. and W. S. Snyder, 1979. Geometry of subducted slabs related to San Andreas Transform. *J. Geol.*, **87**, 609-627.

Houseman, G. and D. McKenzie, 1982. Numerical experiments on the onset of convective instability in the Earth's mantle. *Geophys. J. R. Astr. Soc.*, **68**,

133-164.

Humphreys, E. D. and R. W. Clayton, 1990. Tomographic Image of the Southern California Mantle. *J. Geophys. Res.*, **95**, 19,725-19,746.

Humphreys, E. D. and K. G. Dueker, 1994a. Physical state of the western U.S. upper mantle. *J. Geophys. Res.*, **99**, 9635-9650.

Humphreys, E. D. and K. G. Dueker, 1994b. Western U.S. upper mantle structure. *J. Geophys. Res.*, **99**, 9615-9634.

Jha, K., E. M. Parmentier and J. Phipps Morgan, 1994. The role of mantle-depletion and melt-retention buoyancy in spreading-center segmentation. *Earth Planet. Sci. Lett.*, **125**, 221-234.

Karato, S. and P. Wu, 1993. Rheology of the upper mantle: A synthesis. *Science*, **260**, 771-778.

Laske, G. and T. G. Masters, 1996. Constraints on global phase velocity maps by long-period polarization data. *J. Geophys. Res.*, **101**, 16,059-16,076.

Liu, M. and G. Zandt, 1996. Convective thermal instabilities in the wake of the migrating Mendocino triple junction, California. *Geophys. Res. Lett.*, **23**, 1573-1576.

Poirier, J., 1985. *Creep of crystals.* Cambridge University Press, New York.

Reddy, J. N., 1984. *An introduction to the finite element method.* McGraw-Hill, New York.

Sato, H., I. S. Sacks and T. Murase, 1989. The use of laboratory velocity data for estimating temperature and partial melt fraction in the low velocity zone; comparison with heat flow and electrical conductivity studies. *J. Geophys. Res.*, **94**, 5689-5704.

Severinghaus, J. and T. Atwater, 1990. Cenozoic geometry and thermal state of the subducting slabs beneath western North America. In " *Basin and Range extensional tectonics near the latitude of Las Vegas, Nevada*", ed. B. P. Wernicke, Geol. Soc. Am., pp. 1-22.

Sigmundsson, F. and P. Einarsson, 1992. Glacio-isostatic crustal movements caused by historical volume change of the Vatnajökull Ice Cap, Iceland. *Geophys. Res. Lett.*, **19**, 2123-2126.

Smolarkiewicz, P. K., 1984. A fully multidimensional positive definite advection transport algorithm with small implicit diffusion. *Journal of Computational Physics*, **54**, 325-362.

Van der Lee, S. and G. Nolet, 1996. The S-velocity structure of the upper mantle beneath North America. *J. Geophys. Res.*, **submitted**.

Zandt, G. and C. R. Carrigan, 1993. Small-scale convective instability and upper mantle viscosity under California. *Science*, **261**, 460-463.

Chapter 3

Asthenosphere Flow Model of Hotspot-Ridge Interactions: a Comparison of Iceland and Kerguelen

3.1 Abstract

We develop a numerical model to test the asthenosphere flow paradigm in which hotspots feed the low viscosity asthenosphere, and lithosphere consumes the asthenosphere. The dynamics of this flow model are controlled by the relative position of the hotspot to the ridge, absolute plate velocities, lithosphere and asthenosphere rheologies, and tectonic boundary conditions. The model is applied to two distinct regions - the Iceland hotspot centered on the Mid-Atlantic Ridge, and the Kerguelen hotspot located near the Southeast Indian Ridge. The Iceland model generates along-ridge flow rates as high as 30 cm/yr for an asthenosphere viscosity of $5x10^{18}$ Pa-s. These flow rates are consistent with previous interpretations of the origin of southward pointing V's south of Iceland. The preferred Ker-

guelen model produces significant hotspot-to-ridge flow followed by along-ridge flow; velocities from the off-axis hotspot to the ridge are 66 cm/yr for variable viscosity asthenosphere ranging from $5x10^{18}$ to $5x10^{19}$ Pa-s. The asthenosphere flow paradigm can explain major features of hotspot-ridge interactions for both on-axis and off-axis hotspots.

3.2 Introduction

Many observations indicate that hotspots influence nearby mid-ocean ridge morphology and geochemistry, suggesting a physical link exists between hotspots and ridges. Two types of hotspot-ridge interaction have been proposed: flow from on-axis hotspots along mid-ocean ridges (Figure 3.1a) and flow from off-axis hotspots to nearby mid-ocean ridges (Figure 3.1b). *Vogt* [1971] and *Vogt and Johnson* [1972; 1975] proposed pipe-like flow southward away from the Iceland hotspot as the origin of south-pointing V-shaped bathymetric features along the Reykjanes Ridge, and *Schilling* [1973] invoked similar flow to explain the geochemical gradients found along the Reykjanes Ridge. *Morgan* [1978] suggested that several curious bathymetric lineaments between off-axis hotspots and neighboring ridges could be a consequence of channeled flow from off-axis hotspots to ridges. *Schilling* [1985] presented evidence showing short-wavelength geochemical anomalies along the South Atlantic mid-ocean ridge opposite the Ascension, St. Helena and Tristan hotspots, indicating these off-axis hotspots influenced the nearby ridge. *Small* [1995] has recently shown geophysical evidence of hotspot-ridge interactions in the Southern Ocean, including obliquely oriented aseismic ridges and gravity lineations from hotspots to ridges, and ridge jumps and asymmetric spreading that move ridges toward nearby hotspots, maintaining connections. Under a proposed paradigm for mantle convection [*Phipps Morgan et al.*, 1995], mantle plumes (or hotspots) feed the low viscosity asthenosphere, and astheno-

sphere flows to and along mid-ocean ridges where growing oceanic lithosphere consumes asthenosphere.

We develop a numerical model to test if the asthenosphere flow paradigm can account for both along-ridge flow and focused flow from off-axis hotspots to nearby ridges. Two hotspot-ridge pairs are modeled: the Iceland hotspot centered on the Mid-Atlantic Ridge (MAR) and the Kerguelen hotspot located near the Southeast Indian Ridge (SEIR). We compare model results to previous observations. If asthenosphere flow is responsible for hotspot-ridge interactions, any flow model must account for both along- ridge flow in the Iceland case and hotspot-to-ridge flow in the Kerguelen case.

Early models of asthenosphere flow attempted to conserve mass during mantle convection by returning as asthenosphere all material that plate motions carry away as lithosphere [*Schubert and Turcotte*, 1972; *Schubert et al.*, 1976; *Chase*, 1979; *Parmentier and Oliver*, 1979]. Unlike previous studies of asthenosphere flow, *Phipps Morgan and Smith's* [1992] model explicitly includes thermal lithosphere that grows with age and subducts to the deeper mantle. In their model, lithosphere growth consumes asthenosphere while plumes replenish asthenosphere. Growing lithosphere also narrows the asthenosphere channel, focusing asthenosphere flow. We adapt the *Phipps Morgan and Smith* [1992] formulation to allow for flow in any lateral direction within the asthenosphere layer. Seismic studies of radial Earth structure indicate that the "asthenosphere" is a low-velocity [*Dziewonski and Anderson*, 1981], high-attenuation [*Widmer*, 1991] region underlying oceanic lithosphere from 100-300 km depth. Rock mechanics theory and experiments suggest the shallowest hot mantle will be a low-viscosity zone where pressure effects are smallest [*Karato and Wu*, 1993]. *Phipps Morgan et al.* [1995] calculate that a 200° temperature anomaly within the asthenosphere coupled with the pressure effect implies a viscosity increase as large as 4 orders of magnitude from the asthenosphere to the underlying mesosphere. We assume

that hotspots feed the low viscosity asthenosphere and that lateral flow within the asthenosphere supplies all material for growing lithosphere. This assumption imposes a three-dimensional structure on mantle convection - hotspots efficiently transport material vertically while the asthenosphere redistributes it laterally.

3.3 Numerical Model

We assume the asthenosphere fills a low-viscosity channel bounded above by high-viscosity lithosphere and below by high-viscosity mesosphere. Hotspots replenish asthenosphere consumed by lithosphere growth as shown in Figure 3.2. Growing lithosphere consumes asthenosphere at different rates in different locations. The distribution of the hotspot sources, relative to the lithosphere sinks, creates pressure gradients that drive asthenosphere flow. For our experiments, hotspots supply exactly enough asthenosphere to feed growing lithosphere. Since the vertical extent of the asthenosphere is much smaller than its lateral extent, lubrication theory [*Batchelor*, 1967] can be used to approximate asthenosphere flow as has been done in previous studies [*Schubert and Turcotte*, 1972; *Schubert et al.*, 1976; *Chase*, 1979; *Parmentier and Oliver*, 1979; *Phipps Morgan and Smith*, 1992]. Lubrication theory provides an analytic expression for the pressure flow and shear flow at all asthenosphere depths. As we include lithosphere that grows with age, we extend the formulation of [*Phipps Morgan and Smith*, 1992] to a Cartesian geometry that includes a segmented ridge and a single hotspot source. Once the ridge-hotspot geometry is specified, a finite element formulation solves for pressure throughout the box, then asthenosphere flow and dynamic topography are calculated.

To conserve mass in the lithosphere-asthenosphere system, a pressure gradient develops within the asthenosphere. The physical reason for this dynamic flow is illustrated in a cross section in the plate-spreading direction in Figure 3.3a. The

net lithosphere plus asthenosphere flux at each horizontal position is constant: $q_s + q_p = Q_{tot}$, where q_s is the shear flux and q_p is the pressure flux. The shear flux is the vertically integrated shear flow within the lithosphere and asthenosphere, $q_s(x,y) = U(h_0 - h) + Uh/2$ where U is the absolute plate velocity, $h_0 = 200$ km is the channel thickness at the ridge, $h = h(x,y)$ is the asthenosphere channel thickness and $(h_0 - h)$ is the lithosphere thickness. We assume that the horizontal motion of the mesosphere is negligible. As the asthenosphere thickness and shear fluxes change as a function of position, the pressure flux must change to conserve mass.

Within the asthenosphere, the lubrication theory approximation to the momentum equation applies.

$$\frac{\partial}{\partial z}\left[\mu \frac{\partial \mathbf{u}}{\partial z}\right] = \nabla P \tag{3.1}$$

where z is the distance from the asthenosphere/mesosphere boundary, $\mathbf{u}$ is the vector velocity field, μ is the viscosity which is held constant throughout the asthenosphere, and ∇P is the pressure gradient. Integrating twice results in an expression for the velocity as a function of depth,

$$\boldsymbol{u} = \frac{z^2 \nabla P}{2\mu} + \boldsymbol{c}z + \boldsymbol{d} \tag{3.2}$$

where $\boldsymbol{c}$ and $\boldsymbol{d}$ are constants of integration. In the plate-spreading direction the velocity boundary conditions are $u_y(h) = U$, $u_y(0) = 0$, and the velocity profile within the asthenosphere is

$$u_y = \frac{\nabla P(z^2 - hz)}{2\mu} + \frac{Uz}{h} \tag{3.3}$$

In the ridge-parallel direction the velocity boundary conditions are $u_x(h) = 0$, $u_x(0) = 0$, and the velocity profile within the asthenosphere is

$$u_x = \frac{\nabla P(z^2 - hz)}{2\mu} \tag{3.4}$$

Integrating the velocity fields over the thickness of the asthenosphere yields the asthenosphere flux.

$$q_y = \int_0^h u_y dz = \frac{-h^3 \nabla P}{12\mu} + \frac{Uh}{2} \tag{3.5}$$

$$q_x = \int_0^h u_x dz = \frac{-h^3 \nabla P}{12\mu} \tag{3.6}$$

In the plate-spreading direction (3.5), the flux includes 2 components, pressure flux (first term) and shear flux (second term). In the ridge-parallel direction (3.6), only the pressure flux is required to carry asthenosphere material to supply growing lithosphere.

The pressure field produces dynamic topography

$$w = \frac{P(x, y)}{(\rho_m - \rho_w)g} \tag{3.7}$$

where ρ_m and ρ_w are the densities of mantle and water respectively, and g is the acceleration due to gravity.

3.3.1 Hotspot-Ridge Geometry

We can explore the dynamics of hotspot ridge interactions in a relatively small region with our model. The asthenosphere is bounded above by lithosphere, below by mesosphere, and laterally by subduction zones and continents. Each of these boundaries influences asthenosphere flow as does the hotspot-ridge geometry. The hotspot-ridge geometry establishes the position of asthenosphere source (hotspot) relative to asthenosphere sinks (growing lithosphere). The absolute plate motions fix the asthenosphere shear fluxes, and the hotspot-ridge geometry determines the pressure gradients needed to conserve mass. When a plate is

stationary (Antarctica for the Kerguelen model), the asthenosphere shear flux is zero beneath that plate and there are no asthenosphere sinks because accretion is passive. While passive accretion does not force dynamic asthenosphere flow, it does narrow the asthenosphere channel which affects the flow.

Figure 3.4 presents map views of the idealized geometries used for our models of Iceland-MAR and Kerguelen-SEIR. For the Iceland model geometry, we approximate the MAR as straight from the Charlie Gibbs Fracture Zone (FZ) to the Jan Mayen FZ, and place the hotspot on the MAR two thirds of the distance from the Charlie Gibbs FZ to the Jan Mayen FZ. Spreading is asymmetric - the North American Plate moves with an absolute plate velocity of 15 mm/yr, while the Eurasian Plate moves with a velocity of 5 mm/yr [*Morgan and Phipps Morgan*, personal communication]. For the Kerguelen model geometry, we approximate the SEIR near the Kerguelen hotspot as a three-segment ridge with the middle segment defined by the section of SEIR southeast from Amsterdam and St. Paul Islands which has jumped closer to the hotspot than adjacent portions of the SEIR [*Small*, 1995]. The hotspot lies off-axis under the stationary Antarctic Plate. Spreading is extremely asymmetric - the Indian Plate moves with a velocity of 70.7 mm/yr [*Morgan and Phipps Morgan*, personal communication].

Far from the ridge, continental tectosphere margins [*Jordan*, 1981] and subduction zones bound asthenosphere flow and consume additional asthenosphere. As our models are regional, we approximate the tectonic boundary conditions along the 4 edges of our model box to match the relevent global tectonic boundaries. The model box edges parallel to the ridge correspond to either continental margins or subduction zones. At a continental margin (Greenland and Eurasia for the Iceland model; Antarctica for the Kerguelen model), the net outflow $q_{out} = U(h_{lith}+h_{asth})$ as shown in Figure 3.3b. At the boundary, all asthenosphere must move at the same velocity as the lithosphere and continental root. At a subduction zone (Indonesia for the Kerguelen model), the net outflow $q_{out} = Uh_{lith}$

as shown in Figure 3.3c. Subduction removes only lithosphere from the system, assuming the trench is stationary and no asthenosphere is subducted. The model box edges perpendicular to the ridge correspond to fracture zones, and are treated as symmetry planes, or limits to the flow. The large age offset across major transform faults may create a dam that partially blocks asthenosphere flow [*Vogt and Johnson*, 1975]. Transform faults also bound geochemical provinces along the ridge [*Schilling*, 1986] suggesting that transforms mark a natural asthenosphere flow limit.

3.3.2 Lithosphere Rheology

In our model, lithosphere has a rheological definition - it is much more viscous than the underlying asthenosphere and is treated as being perfectly rigid. The spatial variation in the thickness of the lithosphere determines the distribution of asthenosphere sinks and the asthenosphere channel height. We experiment with 2 lithosphere definitions (Figure 3.5) to determine how each affects asthenosphere flow. The first is a purely thermal lithosphere, and the second is a combined thermal and compositional lithosphere.

Classically, lithosphere has been defined thermally [*Turcotte and Oxburgh*, 1967], as all material colder than a fixed threshold temperature. A cooling half-space model predicts that lithosphere thickness proportional to $\sqrt{age}$ describes a purely thermal lithosphere. The underlying asthenosphere channel thins away from the ridge. Perspective plots of a purely thermal lithosphere are presented in Figures 3.6a and 3.6b for Iceland and Kerguelen model geometries.

Recent experimental [*Karato*, 1986; *Hirth and Kohlstedt*, 1996] and numerical results [*Phipps Morgan*, 1997; *Parmentier*, personal communication] suggest that it is more accurate to define the lithosphere as the region that either thermal or compositional effects have strengthened. Compositional lithosphere may form when near-ridge melting depletes and strengthens the residual material [*Hirth*

and Kohlstedt, 1996; *Phipps Morgan*, 1997]. The depth of melting is assumed to define the base of the compositional lithosphere (Figure 3.5). If we define lithosphere as a mix of thermal and compositional effects, the thicker of the two fixes the effective lithosphere thickness. It is possible that migrating melt keeps the near-ridge region rheologically weak, in which case the asthenosphere is thickest at the ridge and at some distance from the ridge, where melting becomes negligible, the compositional lithosphere dominates [cf. *Phipps Morgan*, 1997]. At young seafloor ages, the base of the lithosphere will be fixed at the base of the compositional lithosphere. At seafloor ages where the thermal lithosphere is thicker than the compositional lithosphere, the thermal lithosphere defines the top of the asthenosphere channel. Figures 3.6c and 3.6d show perspective plots of combined thermal and compositional lithosphere for Iceland and Kerguelen geometries. We also experimented with the effect of a compositional lithosphere that forms instantaneously at the ridge. No figure is shown for this geometry, which is the same as that of Figures 3.6c and 3.6d except that there is no thick asthenosphere channel along the ridge.

3.3.3 Asthenosphere Rheology

In our numerical experiments, we use two different asthenosphere rheologies for each hotspot-ridge geometry: constant viscosity asthenosphere and variable viscosity asthenosphere. As asthenosphere moves away from the hotspot source, it will cool and may lose volatiles [*Valbracht et al.*, 1996], becoming more viscous. Since all asthenosphere comes from the hotspot, we can trace flow lines back to the hotspot to calculate asthenosphere age throughout the model box. We use the velocity field at a fixed depth in the interior of the asthenosphere to calculate asthenosphere age. Asthenosphere viscosity is then parameterized as a function of asthenosphere age such that asthenosphere viscosity increases linearly one order of magnitude from its zero-age injection at the hotspot until it is 30 ma

old. Asthenosphere older than 30 ma is capped at the higher viscosity. For the variable viscosity rheology, we iterate until the flow field converges. For uniform viscosity runs, the viscosity equals $5x10^{18}$ Pa-s. For variable viscosity runs, the viscosity ranges from $5x10^{18}$ Pa-s to $5x10^{19}$ Pa-s.

3.4 Results

For each numerical experiment, we prescribe the hotspot-ridge geometry, absolute plate velocities, the thickness (thickening rate) of the lithosphere, and the type and position of tectonic boundary conditions. We present the Iceland results first to illustrate the dynamics that result from an on-ridge hotspot for different types of lithosphere and for constant and variable viscosity asthenosphere. Then, we present the Kerguelen results to show the dynamics of an off-axis hotspot interacting with a nearby ridge. As for Iceland, we vary the lithosphere and asthenosphere rheologies. Runs are summarized in Table 3.1. The experiments are numbered to correspond to the plotted results of Figure 3.7 for Iceland and Figure 3.8 for Kerguelen.

Numerical simulations were performed on a 33 x 33 node grid. The distance between nodes is 80 km for the Iceland simulations, and 100 km for the Kerguelen simulations. As a resolution test on our numerical method, we performed the same simulations on grids that were twice as fine and found dynamic topography on the coarse grids were within 3% of that on the fine grids. The largest differences occur near the hotspot where the pressure gradients are steepest.

All Iceland simulations have the same geometry and asymmetric spreading as presented in Figure 3.4a. Runs 7a and 7b show that this geometry results in along-ridge flow for both thermal (Figure 3.6a) and thermal-compositional lithosphere (Figure 3.6c). Thermal-compositional lithosphere enhances along-ridge flow by providing a larger asthenosphere channel than purely thermal lithosphere.

In contrast, thermal-instantaneous-compositional lithosphere (Run 7c) results in diffuse flow by eliminating the asthenosphere channel but preserving the same distribution of sinks as for Run 7b. Finally, variable viscosity asthenosphere (Run 7d) enhances along-ridge flow over constant viscosity asthenosphere (Run 7b) for the same type of lithosphere. The asymmetric spreading forces three times more asthenosphere toward the North American Plate than toward the Eurasian Plate. Fluxes are larger in the along-ridge direction toward the Charlie Gibbs FZ than toward the Jan Mayen FZ to conserve mass as there is twice as much lithosphere consuming asthenosphere in the southern direction as in the northern direction. Both of these asymmetric effects are evident in the pattern of dynamic topography contours which clearly show flow being preferentially forced toward the Charlie Gibbs FZ and toward the North American Plate. The continental flux boundary conditions induce significantly more flow than does plate accretion at the ridge. Since the consumption along the ridge is small compared to that at the boundaries, the asthenosphere channel height dominates in controlling the flow. Asthenosphere flux is proportional to h^3 (equations 3.5 and 3.6). In all 4 Iceland experiments, asthenosphere travels along the path of minimum resistance to satisfy the consumption at the continental boundaries. For Runs 7a,b,d asthenosphere travels along the ridge and then perpendicular to the ridge to supply the flux needed at the continental margin. In Run 7c, where no near-ridge asthenosphere channel exists, asthenosphere travels directly to the continental margin.

Kerguelen simulations have the same geometry as presented in Figure 3.4b. Since spreading along the SEIR is so asymmetric, we present model simulations for Kerguelen that have both symmetric and asymmetric spreading in order to illustrate the dramatic effect asymmetric spreading has on asthenosphere flow. The simulations of Figure 3.8 progress from diffuse to more focused flow in alphabetical order. Runs 8a-e include a continent boundary condition for both the

Antarctic and Indian Plates, while Run 8f includes a subduction boundary condition for the Indian Plate. In Runs 8a and 8d, artificial absolute velocities are imposed so that the half-spreading rate at the ridge equals the true half-spreading rate, 35 mm/yr, but the spreading is symmetric. The other four simulations include the true absolute plate velocities of Figure 3.4b. Runs 8a, 8b and 8c present the flow resulting from a purely thermal lithosphere (Figure 3.6b). Comparing Run 8a to 8b reveals the effect of severe asymmetric spreading. When the Antarctic Plate is stationary, the asthenosphere flows toward the rapidly moving Indian Plate. Run 8c adds variable viscosity asthenosphere which forces the asthenosphere toward the SEIR in a more focused pattern than for uniform viscosity flow of Run 8b. Runs 8d, 8e and 8f have thermal-compositional lithosphere (Figure 3.6d) and variable viscosity asthenosphere. The ridge channel created by the thermal-compositional lithosphere allows asthenosphere to travel along the SEIR after it reaches the ridge. Asymmetric spreading causes Run 8e to have more focused flow than Run 8d. The subduction boundary condition of Run 8f increases along-ridge transport as asthenosphere is drawn from the hotspot to feed the ridge segments further from the hotspot. The dynamic topography contours illustrate the degree of focusing of flow from the Kerguelen Hotspot toward and along the SEIR.

We tested thermal-instantaneous-compositional lithosphere for the Kerguelen geometry and the resulting flow was diffuse as for Iceland Run 7c. These experiments illustrate that the thickness of the asthenosphere has a much more dramatic effect on the pattern of asthenosphere flow than the distribution of asthenosphere sinks does.

3.5 Discussion

Table 3.1 presents the maximum pressure-driven asthenosphere velocities and the range of dynamic topography generated for all simulations of Figures 3.7 and 3.8. Dynamic pressure velocities scale with the reciprocal of viscosity. Doubling the viscosity will decrease the velocities by a factor of two. The maximum along-ridge velocities of Runs 7a,b,d are consistent with *Vogt's* [1971] estimates.

The results presented here are for an instantaneous situation where the asthenosphere volume is constant and the hotspot and ridge positions are fixed. In reality, we know that ridges migrate and hotspot strength may vary through time. If an ocean basin grows and the hotspot strength remains constant, the asthenosphere will be thinner across the entire ocean basin. This would cause the asthenosphere flow velocities to increase assuming that everything else remained constant. If the hotspot strength increases, the asthenosphere will thicken to accommodate the increased flux, and asthenosphere flow velocities will decrease.

Both *Ribe et al.* [1995] and *Ito et al.* [1996] present on-ridge plume models that show a cool-broad plume could support the topography observed near Iceland better than a hot-narrow plume which produces excess topography. *Wolfe et al.* [1997] present seismic data that argues for a hot-narrow plume ($\sim$ 150 km radius). If the excess flux produced by a hot-narrow plume were channeled along the ridge, the topography of these 'hot-narrow' models would be more consistent with the observed topography.

Kincaid et al. [1996] explain off-axis hotspot-ridge interactions by buoyant hotspot material flowing up the base of the sloping lithosphere toward a ridge. *Sleep* [1996] also depends on the sloping base of the lithosphere to generate lateral flow within the plume head. If the lithosphere slope is small or zero due to a compositional lithosphere [*Hirth and Kohlstedt*, 1996; *Phipps Morgan*, 1997] then no flow would result from an off-axis hotspot to a nearby ridge according to these models.

Our asthenosphere flow models produce flow patterns, velocities, and support topography that are consistent with observations for both on-ridge (Iceland-MAR) and off-axis (Kerguelen-SEIR) hotspot-ridge geometries. In the Iceland case, shear and pressure flux carry material away from the on-ridge hotspot to supply the growing lithosphere on both sides of the MAR. The Kerguelen Hotspot, located beneath the stationary Antarctic Plate, must supply enough asthenosphere to the ridge to accommodate the large shear and pressure fluxes generated by the rapidly moving Indian Plate. Hotspot-ridge geometry and absolute plate velocities determine asthenosphere flow in our model. These numerical results suggest that the asthenosphere flow paradigm [*Phipps Morgan et al.*, 1995] is consistent with two types of hotspot-ridge interactions.

Run	U_1 mm/yr	U_2 mm/yr	Asth. Viscosity	Lith Type	max $u_x^{pressure}$ mm/yr	max $u_y^{pressure}$ mm/yr	total dyn. topo. meters
7a	15	5	uniform	1	321	192	179
7b	15	5	uniform	2	231	201	152
7c	15	5	uniform	3	78	69	152
7d	15	5	variable	2	264	237	710
8a	35	35	uniform	1	996	1132	871
8b	70	0	uniform	1	996	1164	986
8c	70	0	variable	1	996	1440	2550
8d	35	35	variable	2	1004	1192	2295
8e	70	0	variable	2	1012	1336	3260
8f	70	0	variable	2	460	664	1459

Table 3.1:

U_1=absolute plate velocity of upper plate in Figures 3.4, 3.7, 3.8.

U_2=absolute plate velocity of lower plate in Figures 3.4, 3.7, 3.8.

Lithosphere: 1=thermal lithosphere, base of lithosphere defined by sqrt(age); 2=thermal-compositional lithosphere, lithosphere is thicker of the two, near ridge region has a thin lithosphere ; 3=thermal-instantaneous-compositional-lithosphere, no near-ridge asthenosphere channel.

Viscosity: uniform=asthenosphere viscosity constant at $5x10^{18}$ Pa-s; variable=asthenosphere viscosity varies as a function of asthenosphere age as described in text, viscosity ranges from $5x10^{18}$ Pa-s to $5x10^{19}$ Pa-s.

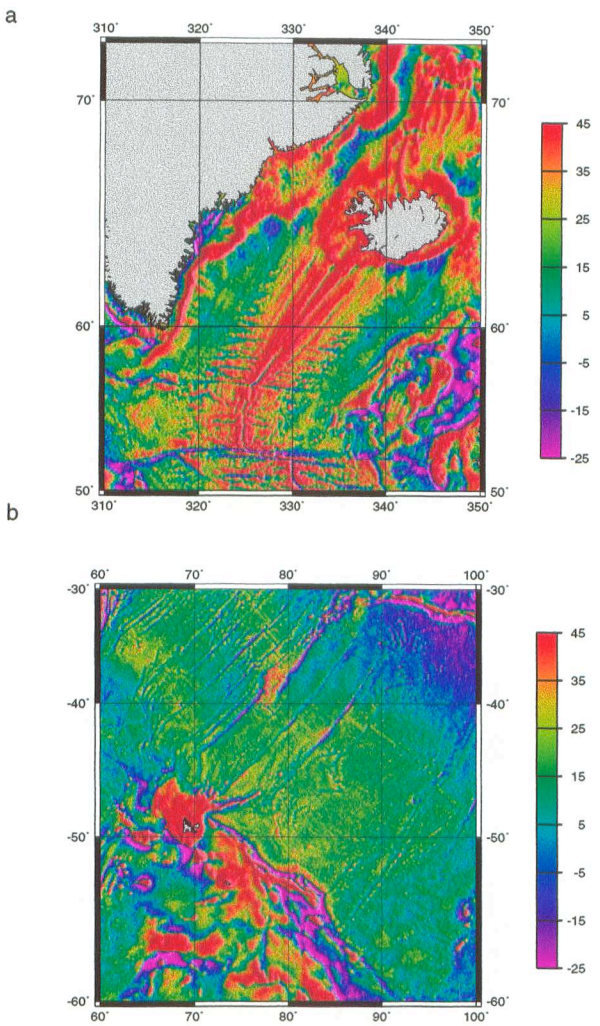

Figure 3.1: Free air gravity anomaly (milligals) extracted from *Sandwell and Smith* [1995] global grid derived from satellite altimetry data. (a) Iceland and the Mid-Atlantic Ridge. V-shaped ridges pointing southwest from Iceland indicate rapid along-ridge flow. (b) Kerguelen and the Southeast Indian Ridge. Volcanic ridges point from Kerguelen toward the Southeast Indian Ridge, suggesting flow from this off-axis hotspot to the ridge. Maps were created using the GMT software [*Wessel and Smith*, 1991].

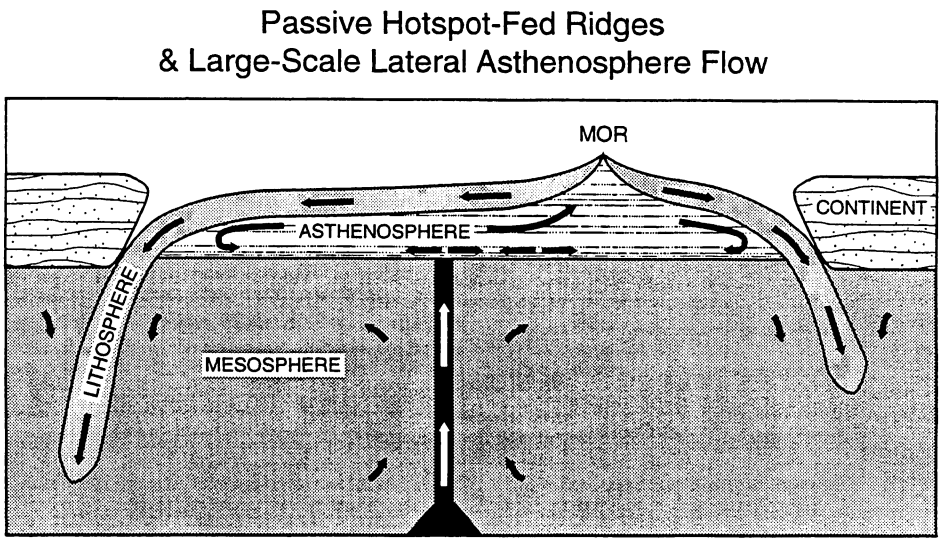

Figure 3.2: Cartoon of proposed mantle convection paradigm [*Phipps Morgan et al.*, 1995] where ridges are passive, and a low viscosity asthenosphere effectively decouples the lithosphere from the mesosphere beneath the ocean basins. Hotspots feed the asthenosphere that is consumed through plate accretion. Lithosphere subducts returning material to the deep mantle.

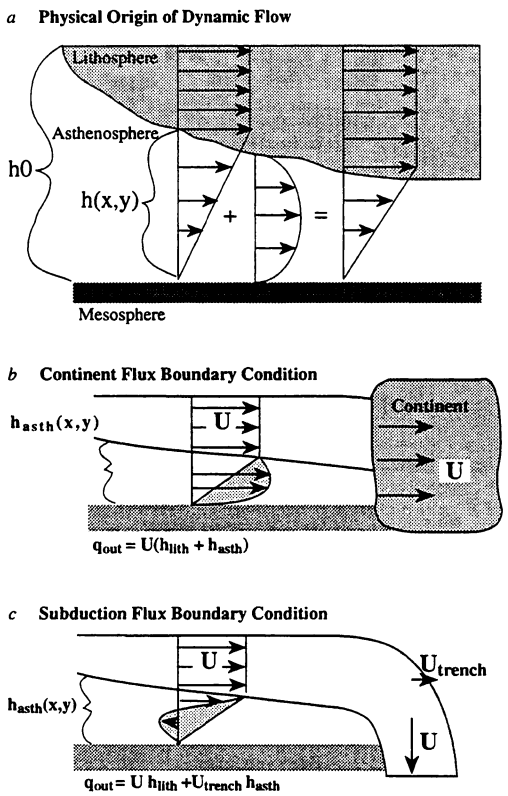

Figure 3.3: (a) Physical cause of dynamic asthenosphere flow. The lithosphere grows as it cools, consuming asthenosphere. In the plate-spreading direction, the net flux of lithosphere plus asthenosphere is constant. To conserve mass, a dynamic pressure gradient develops within the asthenosphere that drives the parabolic pressure flow. (b) Continental flux boundary condition. At an ocean-continent boundary, the net asthenosphere plus lithosphere flux equals the absolute plate motion times the total thickness of lithosphere and asthenosphere (c) Subduction zone boundary condition. Assuming that only lithosphere subducts, the net flux at a subduction boundary equals the absolute plate velocity times the lithosphere thickness.

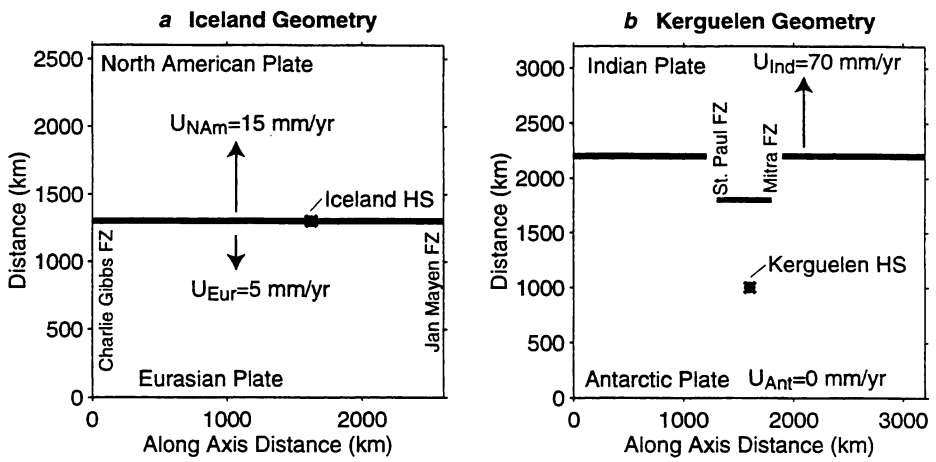

Figure 3.4: (a) Map view of Iceland model geometry. The heavy solid line shows the position of the MAR. The asterisk marks the Iceland hotspot location. The North American plate moves three times as fast as the Eurasian plate with respect to the hotspot reference frame. (b) Map view of Kerguelen model geometry. The three-segment approximation to the SEIR is indicated by the heavy solid line. The Kerguelen hotspot is located beneath the stationary Antarctic plate while the Indian plate moves rapidly away from the hotspot.

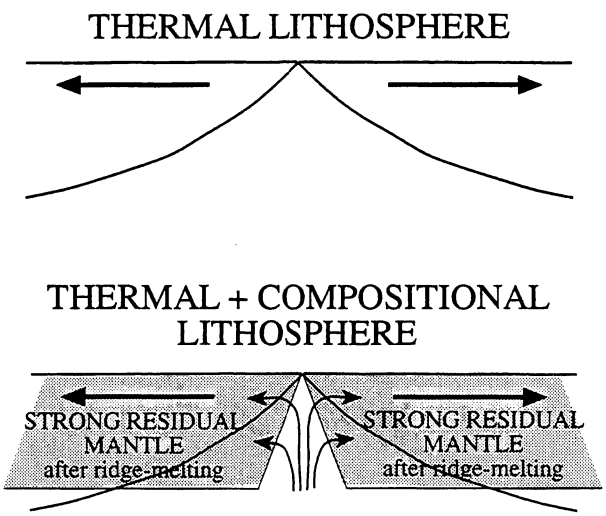

Figure 3.5: (a) Thermal lithosphere. Lithosphere cools as it ages, thickening at a rate dependent on the square root of age. Lithosphere cooler than a fixed temperature is rigid and acts as an upper boundary for the asthenosphere. (b) Thermal-compositional lithosphere. Compositional lithosphere forms near the ridge axis when melting depletes and strengthens residual material. The lithosphere is then defined as the region made rigid either by thermal or compositional effects. In this case, the asthenosphere channel is thinner near the ridge than in the purely thermal lithosphere case.

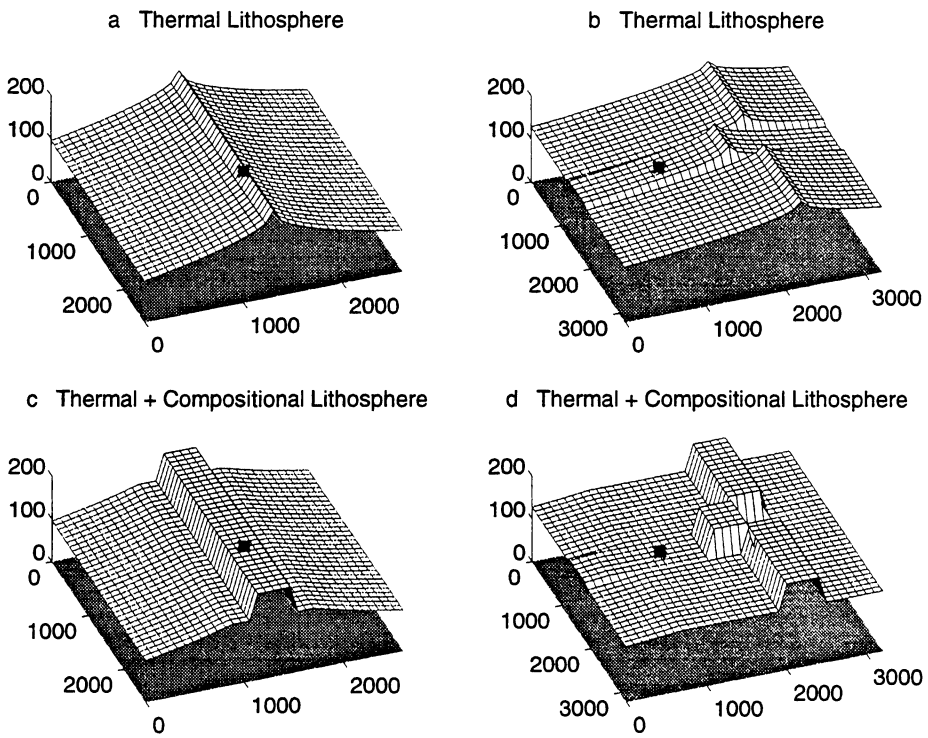

Figure 3.6: Perspective views of model geometries used in our numerical modeling. Gray region indicates the top of the mesosphere. Mesh indicates the position of the base of the lithosphere . The asthenosphere fills the region between the lithosphere and mesosphere. Asterisks mark position of hotspots. (a) Iceland model geometry for a purely thermal lithosphere. (b) Kerguelen model geometry for a purely thermal lithosphere. (c) Iceland model geometry for thermal-compositional lithosphere. (d) Kerguelen model geometry for thermal-compositional lithosphere.

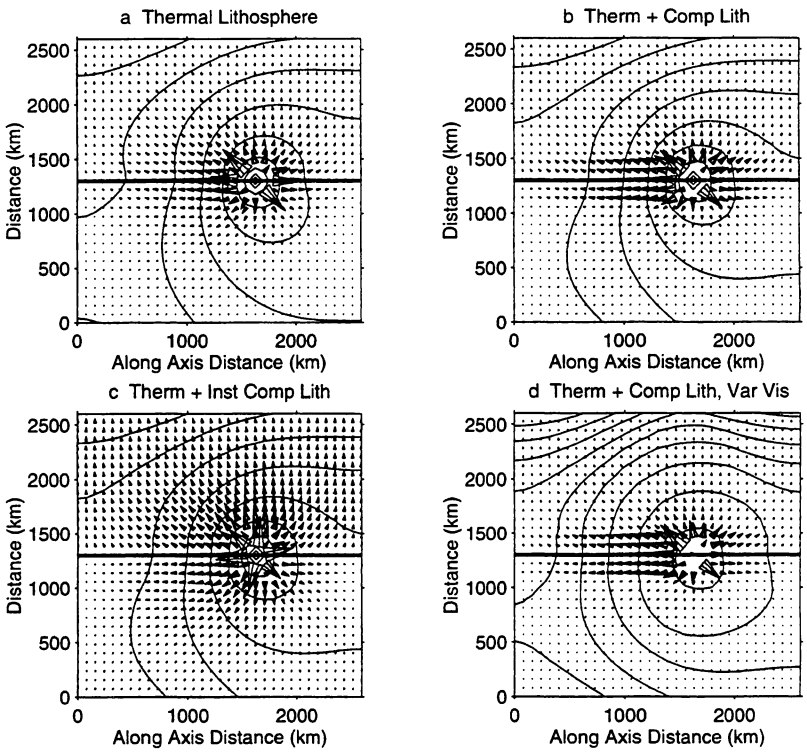

Figure 3.7: Iceland experiments. The heavy solid line shows the position of the ridge. Contours indicate dynamic topography and the contour interval is one tenth the total range for each simulation. The vector field represents the shear flux plus pressure flux at each node. The largest fluxes, which occur near the hotspot, have been masked out so that the more of the dynamic range can be seen. Fluxes for all 4 plots are scaled the same and the maximum fluxes plotted equal 2×10^4 mm^2/yr.(a) Thermal lithosphere, uniform viscosity asthenosphere. (b) Thermal-compositional lithosphere, uniform viscosity asthenosphere. (c) Thermal-instantaneous-compositional lithosphere, uniform viscosity asthenosphere. (d) Thermal-compositional lithosphere, variable viscosity asthenosphere.

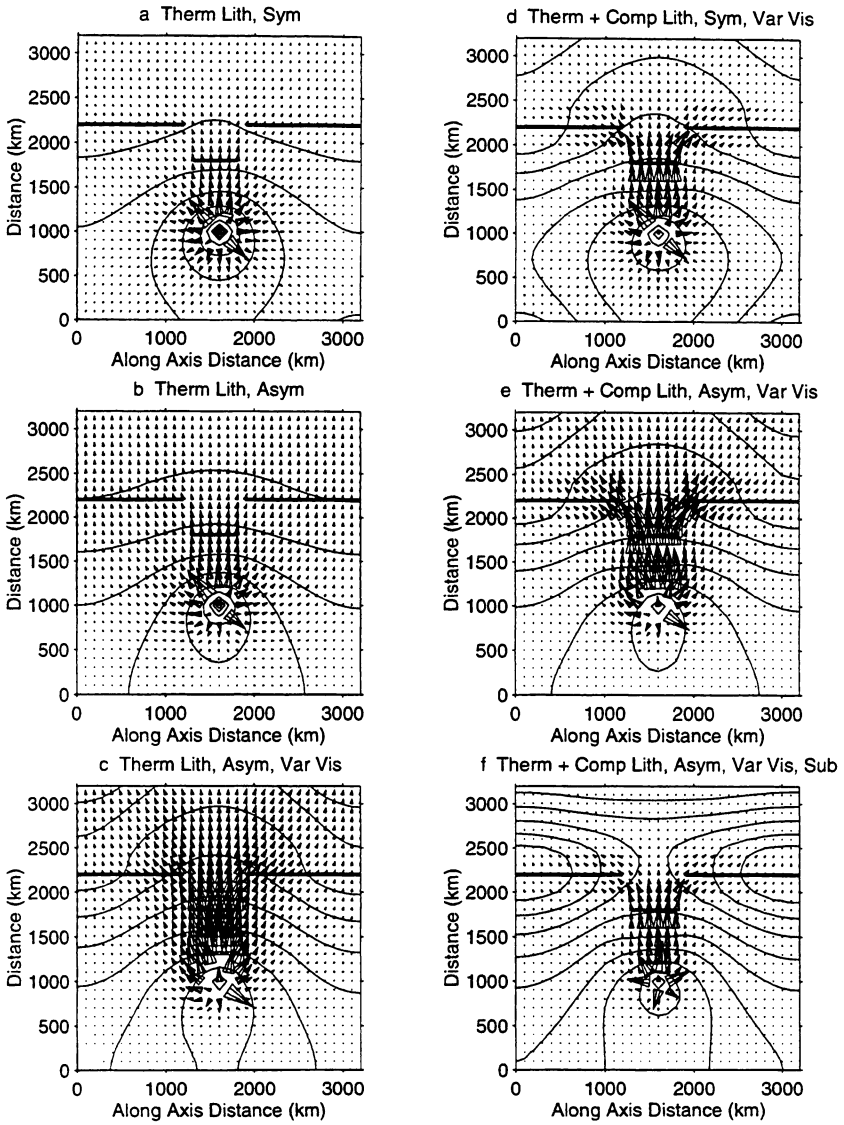

Figure 3.8: Kerguelen experiments. Plotting conventions are the same as for Figure 3.7. Maximum fluxes plotted equal 7x10^4 mm^2/yr. (a) Therm. lith., sym. spreading, uniform vis. asth. (b) Therm. lith., asym. spreading, uniform vis. asth. (c) Therm. lith., asym. spreading, variable vis. asth. (d) Therm-comp lith., sym. spreading, variable vis. asth. (e) Therm-comp lith., asym. spreading, variable vis. asth. (f) Therm-comp lith., asym. spreading, variable vis. asth., subduction zone boundary condition bounds top of Indian Plate.

3.6 References

Batchelor, G. K., 1967. *An Introduction to Fluid Dynamics.* Cambridge Univ. Press, Cambridge.

Chase, C. G., 1979. Asthenospheric counterflow: A kinematic model. *Geophys. J. R. Astron. Soc.*, **56**, 1-18.

Dziewonski, A. and D. L. Anderson, 1981. Preliminary reference Earth model. *Phys. Earth Planet. Inter.*, **25**, 297-356.

Hirth, G. and D. L. Kohlstedt, 1996. Water in the oceanic upper mantle: implications for rheology, melt extraction and the evolution of the lithosphere. *Earth Planet. Sci. Lett.*, **144**, 93-108.

Ito, G., J. Lin and C. W. Gable, 1996. Dynamics of mantle flow and melting at a ridge-centered hotspot: Iceland and the Mid-Atlantic Ridge. *Earth Planet. Sci. Lett.*, **144**, 53-74.

Jordan, T. H., 1981. Continents as a chemical boundary layer. *Philos. Trans. R. Soc. Lond. A*, **301**, 359-373.

Karato, S., 1986. Does partial melting reduce the creep strength of the upper mantle. *Nature*, **319**, 309-310.

Karato, S. and P. Wu, 1993. Rheology of the upper mantle: A synthesis. *Science*, **260**, 771-778.

Kincaid, C., J. G. Schilling and C. Gable, 1996. The dynamics of off-axis plume-ridge interaction in the uppermost mantle. *Earth Planet. Sci. Lett.*, **137**, 29-43.

Morgan, W. J., 1978. A second type of hotspot island. *J. Geophys. Res.*, **132**, 7-22.

Parmentier, E. M. and J. E. Oliver, 1979. A study of shallow mantle flow due to the accretion and subduction of lithospheric plates. *Geophys. J. R. Astron. Soc.*, **57**, 1-22.

Phipps Morgan, J., 1997. The generation of a compositional lithosphere by mid-

ocean ridge melting and its effect on subsequent off-axis hotspot upwelling and melting. *Earth Planet. Sci. Lett.*, **146**, 213-232.

Phipps Morgan, J., et al., 1995. Observational hints for a plume-fed, sub-oceanic asthenosphere and its role in mantle convection. *J. Geophys. Res.*, **100**, 12753-12767.

Phipps Morgan, J. and W. H. F. Smith, 1992. Flattening of the seafloor depth-age curve as a response to asthenospheric flow. *Nature*, **359**, 524-527.

Ribe, N. M., U. R. Christensen and J. TheiBing, 1995. The dynamics of plume-ridge interaction, 1: Ridge-centered plumes. *Earth Planet. Sci. Lett.*, **134**, 155-168.

Sandwell, D. T. and W. H. F. Smith, 1995. *Marine Gravity from Satellite Altimetry*. Geological Data Center, Scripps Inst. of Oceano., 9500 Gilman Dr., La Jolla, CA 92093-0223, anonymous ftp to baltica.ucsd.edu.

Schilling, J.-G., 1973. Iceland mantle plume: Geochemical study of Reykjanes Ridge. *Nature*, **242**, 565-571.

Schilling, J.-G., 1985. Hotspot-migrating ridge interaction in the South Atlantic. *Nature*, **313**, 187-191.

Schilling, J.-G., 1986. Geochemical and isotopic variation along the Mid-Atlantic Ridge axis from 79° N to 0° N. In " *The Geology of North America, Vol. M, The Western North Atlantic Region*", ed. P. R. Vogt and B. E. Tucholke, Geol. Soc. Am., pp. 137-156.

Schubert, G., C. Froidevaux and D. Yuen, 1976. Oceanic lithosphere and asthenosphere: Thermal and mechanical structure. *J. Geophys. Res.*, **81**, 3525-3540.

Schubert, G. and D. L. Turcotte, 1972. One-dimensional model of shallow mantle convection. *J. Geophys. Res.*, **77**, 945-951.

Sleep, N. H., 1996. Lateral flow of hot plume material ponded at sublithospheric depths. *J. Geophys. Res.*, **101**, 28065-28083.

Small, C., 1995. Observations of ridge-hotspot interactions in the Southern

Ocean. *J. Geophys. Res.*, **100**, 17931-17946.

Turcotte, D. L. and E. R. Oxburgh, 1967. Finite amplitude convective cells and continental drift. *Journal of Fluid Mechanics*, **28**, 29-42.

Valbracht, P. J., et al., 1996. Isotopic tracing of volcanic source regions from Hawaii: decoupling of gaseous from lithophile magma components. *Earth Planet. Sci. Lett.*, **144**, 185-198.

Vogt, P. R., 1971. Asthenosphere Motion Recorded by the Ocean Floor South of Iceland. *Earth Planet. Sci. Lett.*, **13**, 153-160.

Vogt, P. R. and G. L. Johnson, 1972. Seismic reflection survey of an oblique aseismic basement trend on the Reykjanes Ridge. *Earth Planet. Sci. Lett.*, **15**, 248-254.

Vogt, P. R. and L. Johnson, 1975. Transform Faults and Longitudinal Flow Below the Midoceanic Ridge. *J. Geophys. Res.*, **80**, 1399-1428.

Wessel, P. and W. H. F. Smith, 1991. Free software helps map and display data. *Eos Trans. AGU*, **72**, 441-446.

Widmer, R., G. Masters and F. Gilbert, 1991. Spherically symmetric attenuation within the Earth from normal mode data. *Geophys. Jour. Int.*, **104**, 541-553.

Wolfe, C. et al., 1997. The anatomy of a mantle plume: Seismic structure of the Iceland hotspot. *Nature*, **385**, 245-247.

Chapter 4

Comparison of Along-Track Resolution of Stacked Geosat, ERS-1, and Topex Satellite Altimeters

Reformatted from: Yale, M. M., D. T. Sandwell, and W. H. F. Smith, *Journal of Geophysical Research*, Vol. **100**, 15,117–15127, August 1995.

4.1 Abstract

Cross-spectral analysis of repeat satellite altimeter profiles was performed to compare the along-track resolution capabilities of Geosat, ERS-1 and TOPEX data. Geophysical Data Records were edited, differentiated, low-pass-filtered, and resampled at 5 Hz. All available data were then loaded into three-dimensional files where repeat cycles were aligned along-track (62 cycles of Geosat/Exact Repeat Mission; 16 cycles of ERS-1, 35-day orbit; 73 cycles of TOPEX). The coherence versus wave number between pairs of repeat profiles was used to estimate

along-track resolution for individual cycles, eight-cycle-average profiles, and 31-cycle-average profiles (Geosat and TOPEX only). Coherence, which depends on signal to noise ratio, reflects factors such as seafloor gravity amplitude, regional seafloor depth, instrument noise, oceanographic noise, and the number of cycles available for stacking (averaging). Detailed resolution analyses are presented for two areas: the equatorial Atlantic, a region with high tectonic signal and low oceanographic noise; and the South Pacific, a region with low tectonic signal and high oceanographic variability. For all three altimeters, along-track resolution is better in the equatorial Atlantic than in the South Pacific. Global maps of along-track resolution show considerable geographic variation. On average globally, the along-track resolution (0.5 coherence) of eight-cycle stacks are approximately the same, 28, 29, and 30 km for TOPEX, Geosat, and ERS-1, respectively. TOPEX 31-cycle stacks (22 km) resolve slightly shorter wavelengths than Geosat 31-cycle stacks (24 km). The stacked data, which are publicly available, will be used in future global gravity grids, and for detailed studies of mid-ocean ridge axes, fracture zones, seamounts, and seafloor roughness.

4.2 Introduction

Recently, marine geophysics has been greatly advanced by accurate gravity maps derived from satellite altimetry data [*McAdoo and Marks*, 1992a; *Sandwell*, 1992; *Sandwell and Smith*, 1992; *Marks, et al.*, 1993] . Many applications such as charting and modeling of seamounts, mid-ocean ridges, and fractures zones require the best short-wavelength resolution possible. High-resolution gravity maps depend on both the resolution of the individual profiles and the profile spacing. Even though altimeter profile spacing is very dense in some ocean areas (currently south of 30° S), the best gravity field resolution is still slightly worse than can be obtained from modern shipboard measurements [*Neumann et al.*, 1993] . The

resolution and accuracy of the individual profiles can be improved by averaging (stacking) along repeated ground tracks because the random noise component is suppressed during averaging. Stacking is possible for Geosat, ERS-1, and TOPEX since they were/are in an exact repeat orbit for at least part of their mission. Each satellite has a unique orbit that governs the spacing of the ground tracks as well as the repeat cycle duration. Optimal coverage, and thus the best two-dimensional (2-D) gravity resolution, is obtained by combining ground tracks from multiple satellites (Figure 4.1a). However, to intelligently combine the data from the different satellites, it is necessary to understand the resolution capabilities of each altimeter.

As in previous studies, we compare profiles that repeat to within about 1 km along the same ground track in order to assess the quality of the data [*Brammer*, 1979] . The difference between a pair of repeat profiles provides an estimate of the noise, while the coherence between repeat profiles provides a measure of the along-track resolution. Previous repeat-track analyses have shown improvement in along-track resolution with each new altimeter due to improved technology; Geos 3 75 km [*Brammer*, 1979; *Marks and Sailor*, 1986] , Seasat 50 km [*Marks and Sailor*, 1986; *Sailor*, 1982] , Geosat individual profiles 30 km [*Born et al.*, 1987; *Sandwell and McAdoo*, 1988], and ERS-1 individual profiles 30 km [*McAdoo and Marks*, 1992b]. Geosat was the first altimeter to be maintained in an exact repeat orbit for a long period (3 years) of time. Stacking many Geosat repeat profiles significantly improves accuracy and resolution so that wavelengths longer than about 20 km can be resolved [*Sandwell and McAdoo*, 1990].

In this study we assess the accuracy and resolution of both single profiles and stacked profiles from Geosat, ERS-1, and TOPEX, using the same methods so that all three altimeters can be directly compared. For each altimeter we assess the improvement gained by stacking and illustrate the many factors that control resolution including: gravity signal, oceanographic and instrument noise, ocean

depth, and number of cycles available for stacking.

A major focus of our study is to understand the noise characteristics of the ERS-1 altimeter. While the TOPEX altimeter is technologically the most sophisticated and thus potentially has the best resolution, the ERS-1 35-day repeat orbit has the greatest spatial coverage and track density, making it the most valuable for detailed geophysical studies. Moreover, in April 1994, ERS-1 was placed in an orbit with a 168-day repeat cycle (16-km cross-track spacing). These new data will be the primary source of unclassified gravity information in areas north of 30° S. South of 30° S the gravity field is well constrained by declassified Geosat Geodetic Mission Data [*Marks et al.*, 1993] with 4-km cross-track spacing. Thus the noise characteristics of ERS-1 must be well understood prior to constructing gravity grids. In particular, we wish to establish how factors such as ocean wave height influence data quality so optimal schemes for editing, filtering, and gridding the data can be designed.

The paper consists of two main parts: a data analysis section where preprocessing and stacking methods are presented and the characteristics of each data set are compared; and a resolution section that explains the procedures used and then directly compares the spectra and resolution results from analyses of all three altimeters, globally and in regions of high and low signal to noise ratios.

4.3 Data Analysis

4.3.1 Satellite Characteristics

The satellite characteristics are summarized in Table 4.1. Since these satellite altimeters orbit Earth many times each day (14.3 for Geosat and ERS-1; 12.7 for TOPEX), the duration of one repeat cycle is inversely related to the cross-track spacing at the equator. Figure 4.1a shows the ground tracks of all three satellites around Hawaii, illustrating the unique orbit of each satellite.

The Geosat altimeter was in a 17-day repeat cycle for 3 years; we use the first 62 cycles of Geosat Geophysical Data Record (GDR) data from November 7, 1986, to October 28, 1989 [*Cheney et al.*, 1991] . The ERS-1 altimeter was in a 35-day repeat cycle for 17 cycles. We use cycles 2-17 of ERS-1 data from May 19, 1992, to November 30, 1993. The first 35-day cycle of ERS-1 data was not included because its ground track deviated by 2-3 km from the other 16 cycles. Ground tracks of all 35-day ERS-1 data are shown in Figure 4.1b. Coverage is nearly complete between $\pm 81.5°$, except in some regions of permanent sea ice (Weddell Sea, Arctic Ocean).

The TOPEX/POSEIDON mission is in a 10-day repeat cycle for the life of the satellite. TOPEX and POSEIDON are two distinct altimeters that share an antenna, so only one altimeter is operating at any time. POSEIDON is an experimental altimeter operated by Centre National d'Etude Spatiale (CNES) which was initially turned on for part of each cycle and subsequently turned on for a few entire cycles. To maintain a consistent data set related to the TOPEX altimeter, we exclude the POSEIDON data. We use cycles 1-78 of TOPEX GDR data, from September 22, 1992 to November 5, 1994, excluding POSEIDON only cycles (20, 31, 41, 55, 65).

	Repeat Cycle Duration, days	Cross-Track Spacing, km	Latitude Range
Geosat	17	164	$\pm 72.0°$
ERS-1	35	80	$\pm 81.5°$
TOPEX	10	315	$\pm 66.0°$

Table 4.1: Satellite Characteristics

4.3.2 Preprocessing

The 1 s^{-1} GDRs contain 10 sea surface height measurements, environmental corrections, and preprocessing flags. The GDRs for each satellite were edited on the basis of prior experience with Seasat data [*Marsh and Martin*, 1982] and with Geosat data [*Sandwell and McAdoo*, 1990]. Different editing criteria are applied to ERS-1 data because it is noisier than the Geosat and TOPEX data, and we show below that the noise increases as a function of significant wave height (SWH). Several of the preprocessing flags were used to eliminate 1 s^{-1} records. Data flagged as land or ice were eliminated from all three data sets. Geosat and TOPEX were both edited when the SWH was greater than 8 m or less than 0.1 m; ERS-1 was edited for SWH greater than 6 m or less than 0.01 m. Geosat and TOPEX were both edited for high and low automatic gain control (AGC); Geosat data were eliminated for AGC greater than 35 dB or less than 15 dB; TOPEX data were edited for AGC greater than 64 dB; ERS-1 GDRs did not contain AGC, and thus no AGC editing was performed on the ERS-1 data.

A procedure was used to eliminate outliers among the 10 sea surface height measurements within each 1 s^{-1} record by fitting a line to the trend of the 10 sea surface height measurements and calculating the standard deviation about this line, σ_h [*Cheney et al.*, 1991] . Geosat and TOPEX were both edited when σ_h exceeded 0.15 m; ERS-1 was edited for σ_h greater than 0.25 m.

Throughout our analysis we are interested in wavelengths shorter than 100 km where environmental corrections (tides, ionosphere, wet/dry troposphere) presumably have no signal. We tested the effect of adding corrections to the TOPEX data and found that corrected and uncorrected TOPEX deflection of the vertical data had a coherence greater than 0.5 for wavelengths longer than about 4 km, which is significantly shorter than we can resolve with the altimetry data.

A low-pass Parks-McClellan filter, designed with the MATLAB Signal Pro-

cessing Toolbox, is applied to the 10 s^{-1} data, and then the filtered data are resampled at 5 s^{-1} (Figure 4.2). This prestack filter is intended to suppress the high-amplitude, short wavelength noise associated with the first difference operation that comes next. Initially, the same filter was applied to all three data sets, and it was evident that the ERS-1 data were noisier than Geosat and TOPEX data. To suppress this noise, we reprocessed the ERS-1 data with a longer filter that starts to cut off at longer wavelengths. Later, we show that these prestack filters do not attenuate signals in the band resolved by the altimeters.

After filtering, sea surface height profiles were converted to along-track sea surface slope (along-track vertical deflection) for the remainder of the analysis, according to the method of *Sandwell and McAdoo* [1990] . This conversion uses the first difference operation, which acts as a high-pass filter, amplifying short-wavelength gravity anomalies and suppressing long-wavelength orbit errors, oceanography, and environmental errors. Slope profiles of arbitrary lengths and having arbitrary data gaps can be averaged without first adjusting the DC level of each profile. Because of orbit and other long-wavelength errors, height profiles cannot be averaged this way [*Sandwell and McAdoo*, 1990]. Later, stacked slope profiles can be integrated to recover stacked height profiles with an undetermined DC level.

4.3.3 Stacking

After editing, filtering, and resampling, the 5 s^{-1} data from each satellite were loaded into two three-dimensional (3-D) stack files, one for ascending ground tracks and one for descending ground tracks. The characteristics of each satellites orbit (Table 4.1) determine the dimensions of these files (Table 4.2).

Prior to loading the stack files, we developed a model (average) ground track for each satellite, based on an idealized circular orbit [*Sandwell*, 1992] . A number of representative cycles were used to constrain the important model parameters

	Number of Equator Crossings	Number of Cycles	Number of Along-Track Bins
Geosat	244	62	16000
ERS-1	501	16	17000
TOPEX	127	73	17000

Table 4.2: Stack File Dimensions

(orbit inclination and first ascending equator crossing longitude). For all three satellites the across-track deviation of the actual track from the model track was generally less than 1 km. Because the idealized orbit accounts for neither the ellipticity of the actual orbit, nor the perturbing effects of Earth's oblateness, along-track deviations from the model track are sometimes larger than the along-track bin width of 1.3 km. In these cases, the model track was used to determine the approximate bin number, and then the data point was placed in the proper nearby bin. For each cycle of data, the vertical deflection and the along- and across-track deviations between the actual and model location were stored in the stack file. For ERS-1, SWH was also stored in order to assess its effect on altimeter noise. When all of the available cycles have been inserted into the stack file, we are ready to average the profiles.

The stack files provide a convenient structure for manipulating these very large data bases. To stack data, we specify which cycles to average and the range of equator crossing longitudes over which to perform the averaging. At every position along-track, we use all available cycles, among those specified, to calculate first the median deflection of the vertical and then the median absolute deviation. Points that deviate from the median by more than 3 times the median deviation are edited, following a robust method for eliminating outliers [*Rousseeuw and Leroy*, 1987]. From the remaining N points we calculate (and store) the mean

and standard deviation ($N > 3$). Figure 4.3 illustrates the stacking of a short profile that crosses the Mid-Atlantic Ridge near the equator for all three satellites. Only eight of the available cycles are included for each satellite to show the relative quality of the data after it has been edited and filtered. (For Figure 4.3 only, Geosat and TOPEX individual cycles were filtered additionally before plotting so that individual cycles from each satellite have the same frequency content.) Stacked profiles based on the eight cycles shown and on all available data are also presented.

4.3.4 Global Characteristics of Stacks

We stacked all available ascending and descending data for each satellite and determined global measures of the number of cycles stacked and the standard deviation of each stack. The number of cycles stacked as a function of position was calculated by finding the block median of the number of cycles stacked along all the tracks that intersect each 1° Mercator cell, and then empty cells were filled by a nearest-neighbor interpolation algorithm [*Wessel and Smith*, 1991] . Figure 4.4 shows global maps of the number of cycles stacked for each satellite. The latitude range (Table 4.1) covered by Geosat and TOPEX is ice-free for at least part of the year, while the extended range of ERS-1 is limited by permanent ice coverage in some areas [*Laxon and McAdoo*, 1994] . Each map of the number of cycles stacked shows variations that depend on the altimeter. Geosat has patches of fewer cycles that are due to oscillations in the antenna direction with respect to nadir. ERS-1 has stripes of fewer cycles that are due to data loss when downloading to ground stations. TOPEX has a very regular pattern of stripes that look like ground tracks, where about 10 fewer cycles are stacked than in adjacent areas, due to excluding POSEIDON data from early TOPEX/POSEIDON cycles.

Global maps of the standard deviation about the stack for each satellite were made in the same way as described above for the maps of the number of cycles

stacked. Figure 4.5 presents a global map of ERS-1 standard deviation about the stack. This map shows a very strong latitudinal dependence, with the highest standard deviation in the southern oceans, and the lowest near the equator. Maps of geographic variation in standard deviation for the other two altimeters (not shown) exhibit the same strong latitudinal dependence, while the magnitude of the standard deviation depends on how the data were filtered before stacking. The strong latitudinal dependence suggests a correlation between weather/sea state and noise in the altimeter measurements.

Global maps of average SWH (not shown) as measured by ERS-1 and other altimeters demonstrate a geographic pattern that is almost identical to the global map of geographic standard deviation of the stack shown in Figure 4.5. This strong apparent connection between SWH and variation of the stack motivated us to look at the deviation from the stack as a function of SWH. We stacked all available data from ERS-1 cycles 2-17 and then calculated the absolute deviation of each cycle from the stack and computed mean and median deviations in 0.05 m SWH bins. As illustrated in Figure 4.6, the median absolute deviation from the stack increases approximately by a factor of 2 over the range of SWH. The absolute deviation increases rapidly for SWH>6 m, and thus these data were edited.

4.4 Resolution

We follow the repeat track method for determining the resolution of altimetry data from each satellite [*Sandwell and McAdoo*, 1990] . As explained in previous studies, sea surface height measurements consist of several components, including time invariant geoid undulations and permanent long-wavelength oceanography and time-varying "noise" due to oceanographic variability, orbit error, and measurement error. Repeating altimeter profiles measure a common sea surface

height signal plus "noise" which varies among repeat profiles. While ocean circulation contributes to part of the permanent sea surface topography, it consists primarily of a long-wavelength ($>$ 1000 km), low-amplitude ($<$ 1 μrad) signal [*Levitus*, 1982]. We are interested in resolving wavelengths shorter than 100 km; thus permanent oceanography will not limit our resolution capabilities. Our use of vertical deflection profiles instead of sea surface topography profiles changes the amplitude and shape of the power spectra but does not affect the coherence estimates [*Sandwell and McAdoo*, 1990].

For each satellite, the repeat track method was performed on pairs of randomly selected individual cycles, and on pairs of eight-cycle stacks spanning approximately the same seasons. In addition, pairs of 31-cycle stacks of Geosat and TOPEX data were analyzed. After explaining the procedure used in all resolution analyses, detailed spectra are presented for each satellite in two areas, then results of all resolution analyses are discussed.

Data from a pair of repeat profiles are extracted from the large 3-D stack files such that corresponding points are always available, ensuring that the profiles are properly aligned, and any small data gaps are common to both profiles. We apply the *Welch* [1967] method of power and cross-spectral estimation with 50% overlap. All available profiles are split into 256 point segments (340 km for Geosat and ERS-1, 300 km for TOPEX), offset 128 points from adjacent segments. For each segment, $s_1(x)$ and $s_2(x)$ are the deflection of the vertical for the two profiles where x is the along track distance, and the noise is approximated by $d(x) = [s_1(x) - s_2(x)]/\sqrt{2}$. We first detrend and apply a Hanning window to s_1, s_2, and d before calculating the discrete Fourier transform of each. Next, we estimate the power spectral density (PSD) of s_1, s_2, and d and the cross spectrum of s_1 and s_2. Finally, power spectra and cross spectra from all available segments are averaged. The average PSDs of s_1, s_2 , and d are given by

$$P_{11} = \frac{1}{N}\sum_{i=1}^{N}(S_1 S_1^*)_i$$

$$P_{22} = \frac{1}{N}\sum_{i=1}^{N}(S_2 S_2^*)_i$$

$$P_{noise} = \frac{1}{N}\sum_{i=1}^{N}(DD^*)_i$$

respectively; and the average cross spectral density is given by

$$P_{12} = \frac{1}{N}\sum_{i=1}^{N}(S_1 S_2^*)_i.$$

Capital letters denote the Fourier transform of the detrended and windowed profiles, i indicates the segment number, N is the number of segments. P_{11} and P_{22} provide a measure of the power in the signal plus the noise, while P_{noise} provides an estimate of the noise that differs between s_1 and s_2. The coherence is given by $\rho(k) = |P_{11}|^2 / (P_{11} P_{22})$.

Resolution is given by the wavelength, $\lambda = 1/k$ where the coherence falls to 0.5 (signal-to-noise ratio of 2.414). A model coherence is parametrically fit to the actual coherence, using the entire curve to determine the resolution [*Smith and Sandwell*, 1994] . In most of the analyses presented, resolution estimates are based on averaging the spectra from several hundred segments; however, averaging as few as 20 segments yields sufficiently smooth coherence curves for parametric fitting.

In the eight-cycle stack comparison, for ERS-1, $s_1(x)$ is an average of cycles 2-9, $s_2(x)$ is an average of cycles 10-17; for Geosat and TOPEX, $s_1(x)$ and $s_2(x)$ are averages of eight cycles that span the same period of the year as the ERS-1 eight-cycle stacks.

4.4.1 Area 1 and Area 2 Results

For each satellite, we use all available profiles pairs for resolution analyses in two geographic areas, area 1 in the equatorial Atlantic and area 2 in the South Pacific (Figure 4.1b). Profiles used run from southeast to northwest; Geosat and ERS-1 profiles are ascending as their orbits are both retrograde, while TOPEX profiles are descending as TOPEX is in a prograde orbit. Profiles in area 1 cross several prominent fracture zones and the Mid-Atlantic Ridge providing large signal, while noise is relatively low (Figure 4.5) and coverage is nearly complete (Figure 4.4) for all three satellites. All of these effects combine to make the signal to noise ratio high in area 1, and we expect the resolution in this region to represent the best possible with each altimeter. In contrast to area 1, the seafloor in area 2 is relatively smooth, and profiles cross few fracture zones, providing a relatively low tectonic signal while noise is relatively high (Figure 4.5), and includes a long wavelength component of oceanographic "noise" due to the variability of the Antarctic Circumpolar Current (ACC) and associated storms and waves.

The results of the resolution analyses of individual cycles and half stacks in area 1 and area 2 are presented in Figure 4.7. Several features of the spectra and coherence estimates are common to data from the three satellites in both areas. For both individual cycles and half stacks, P_{11} decreases as a function of increasing wave number until the signal becomes negligible with respect to the noise; the dip in power at the lowest wave numbers is due to detrending and Hanning windowing. P_{noise} increases as a function of increasing wave number. At long wavelengths, where the signal to noise ratio is high, P_{11}^{cycle} and P_{11}^{stack} are close; differences are due to data gaps in the cycle pair. At shorter wavelengths, the noise dominates the signal so P_{11} and P_{noise} are parallel and nearly coincident. One can see from Figure 4.7 that the reduction in the P_{noise}^{stack} at high frequencies is approximately equal to the number of cycles available in each half-stack, which varies geographically and among satellites (Figure 4.4). Since the coherence de-

pends on the signal to noise ratio, noise reduction due to stacking improves the resolution for all three altimeters in both areas.

The lower signal and higher noise in area 2 are clearly revealed in Figure 4.7. The magnitude of P_{11} in area 2 is not as high as in area 1, even at long wavelengths, due to the lack of signal. Stacking does not reduce P_{noise} by as much as in area 1, because for each satellite, the average number of cycles available for stacking in area 2 is lower than the average number available in area 1. P_{noise} for both cycle and half-stack analyses for all satellites has a bump at long wavelengths that reflects variations in the ACC between the two cycles and two half stacks. The coherence plots in area 2 reflect the component of long-wavelength oceanography that is contributing to the noise spectrum, as individual cycles and half stacks are significantly less coherent at the longest wavelengths than in area 1.

Quantitative evaluation of resolution is achieved by examining the coherence plots in the second and fourth rows of Figure 4.7. For all three satellites ρ_{stack} is greater than ρ_{cycle}. Results from areas 1 and 2 and global averages of all ascending and descending profiles from each satellite are summarized in Table 4.3. In addition to reflecting oceanographic variations between profiles in a pair, the resolution of individual cycles reflects the quality of the 5 s^{-1} data after filtering, while the resolution of the half stacks reflects a combination of the quality of the 5 s^{-1} data and improvement due to robust editing and averaging during stacking. When all three satellites are compared on an equal basis (eight-cycle stack), they all have approximately the same globally averaged resolution.

In all stack comparisons, TOPEX resolution is the best. TOPEX noise levels are lower for individual cycles and noise reduction is greatest for TOPEX, probably because of its uniform track density (Figure 4.4). TOPEX does show lower P_{11} than the other satellites in both areas, suggesting that its sparsely spaced tracks missed some high-amplitude features that Geosat and ERS-1 tracks crossed.

	Area 1		
	Cycle	Stack 8	Stack 31
Geosat	33	26	20
ERS-1	38	26	-
TOPEX	34	24	19
	Area 2		
	Cycle	Stack 8	Stack 31
Geosat	52	38	27
ERS-1	50	33	-
TOPEX	43	31	23
	Global Average		
	Cycle	Stack 8	Stack 31
Geosat	38	29	24
ERS-1	43	30	-
TOPEX	37	28	22

Table 4.3: Summary of Along-Track Resolution Estimates

4.4.2 Global Results

As the results from area 1 and area 2 indicate substantial geographic variations in resolution, we have created global resolution maps to present the true data quality of eight-cycle stacks for ERS-1 and 31-cycle stacks for Geosat and TOPEX. For each 10°x10°geographic bin, we average the power and cross spectra for all segments centered within the bin, compute a coherence curve $\rho(k)$, and find k where $\rho = 0.5$. The resulting k values are gridded and presented as maps of resolution for each satellite in Figure 4.8. In addition to geographic variations in noise and the number of cycles available, regional ocean depth is also an important factor in determining resolution of altimetry data. Upward continuation

from the deep seafloor (2-6 km) attenuates the amplitude of vertical deflection measured at the sea surface. For example, a signal having a 20-km wavelength is attenuated by a factor of 0.2 when the ocean depth is 5 km.

Comparing the maps from the three satellites reveals that the along-track resolution is somewhat lower for ERS-1 relative to Geosat and TOPEX, due to having fewer ERS-1 cycles to average. The Geosat and TOPEX maps reveal along-track resolution in the range 20-25 km; however, the ERS-1 map is predominantly in the range 25-33 km. For each satellite the maps have some common dark patches that correspond to shallow regions with high tectonic signal and low oceanographic noise (Figure 4.5): the Mid-Atlantic Ridge, the Seychelles region, the Central Indian Ridge, and the western Pacific, near New Guinea. The resolution is lowest near land and at high latitudes, where fewer cycles were available for stacking. The Geosat map has patches of higher resolution in the Pacific that correspond to the regions where more cycles were available for stacking (Figure 4.4).

4.5 Summary

These resolution studies highlight the many factors that are important in determining along-track resolution of satellite altimetry data. Ultimately, the resolution is determined by the signal to noise ratio which includes both satellite-independent components and satellite-dependent components. Factors that are geographically determined and satellite-independent include seafloor roughness, ocean depth, and sea surface variability. The sea surface is in a continual state of flux due to changes in seasonal weather patterns and changes in global ocean circulation. Each satellite altimeter is unique in design and therefore each has instrument specific errors including instrument noise, tracking algorithm noise, and orbit determination errors. While random instrument noise and orbit errors

are not geographically dependent, we discovered that high sea state increases the uncertainty in the measurement of sea surface height. When the sea is rougher as at high latitudes, the radar pulse is scattered more, and tracking of the return pulse is less accurate.

Stacking or averaging many repeat cycles improves the resolution for all three satellite altimeters. Globally averaged coherence results for stacked Geosat, ERS-1, and TOPEX data are summarized in Figure 4.9 and Table 4.3. Stacking decreases the effect of instrument and oceanographic noise and therefore increases the signal to noise ratio. Geosat and TOPEX individual cycle data are less noisy than ERS-1 data, and there are more cycles available for averaging Geosat and TOPEX relative to ERS-1, which provides greater noise reduction and a more robust median for eliminating outliers. The number of cycles available for stacking varies by satellite and also varies geographically for each satellite, further complicating the issue of separating geographic signal and noise contributors. Globally, the along-track resolution of Geosat and TOPEX stacks are approximately the same (24 and 22 km, respectively) while the resolution of ERS-1 stacks are slightly worse (30 km). The stacked data described here provide highly accurate profiles for creating global gravity grids and for performing detailed gravity studies of fracture zones, mid-ocean ridge axes, propagating rifts, and seamounts. Global stacked deflection of the vertical profiles from Geosat (62 cycles), ERS-1 (16 cycles), and TOPEX (62 cycles) are available via anonymous ftp from arch.ucsd.edu.

4.6 Acknowledgments

The text of this chapter, in full, is a reformatted version of the material as it appears in, Yale, M. M., D. T. Sandwell, and W. H. F. Smith, *Journal of Geophysical Research*, Vol. **100**, 15,117–15127, August 1995. I was the primary

researcher and author, and David T. Sandwell and Walter H. F. Smith directed and supervised the research which forms the basis of this chapter.

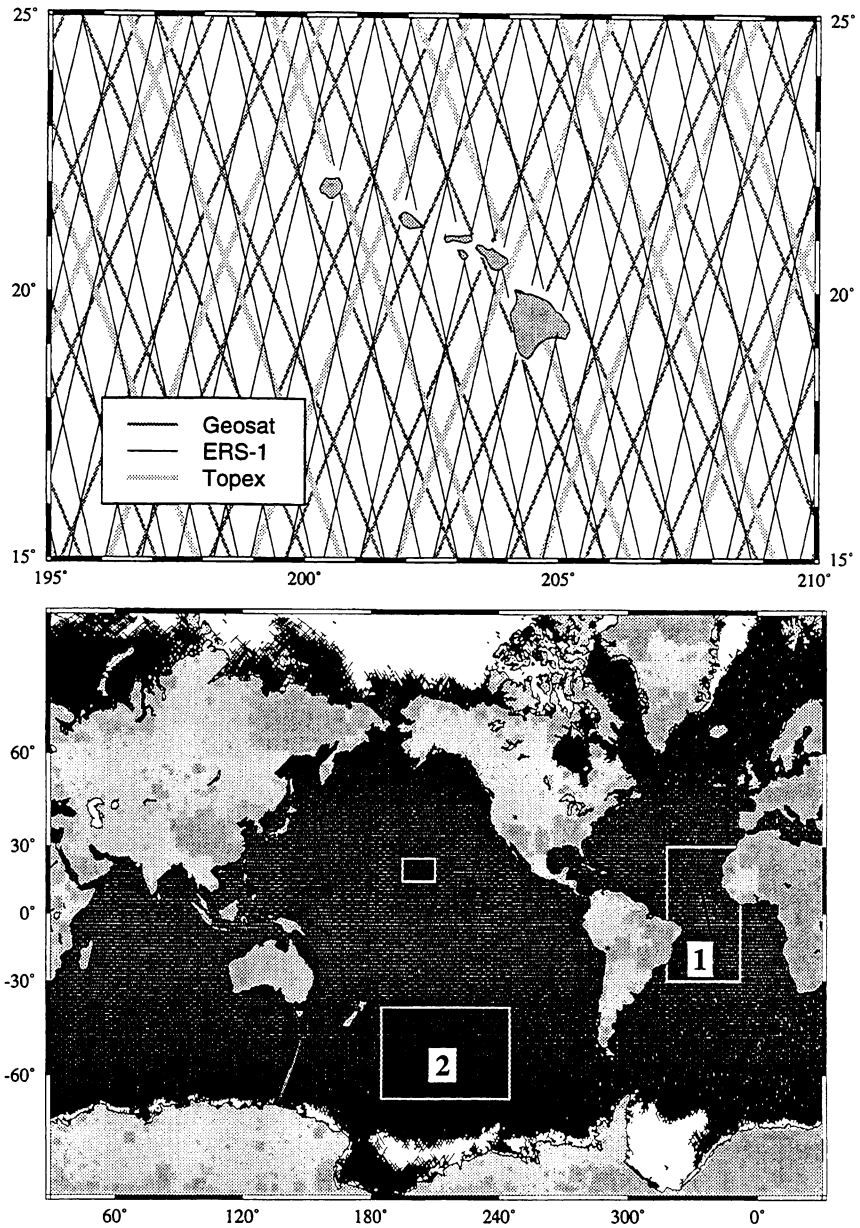

Figure 4.1: Ground Tracks. (a) Ground tracks for Geosat, ERS-1, and TOPEX for the region surrounding Hawaii, indicated in Figure 4.1b. (b) Ground tracks of ERS-1 35-day orbit. Data within regions 1 and 2 are used in the resolution analyses presented in Figure 4.7 and Table 4.3. The thick line in area 1 is the location of profiles in Figure 4.3.

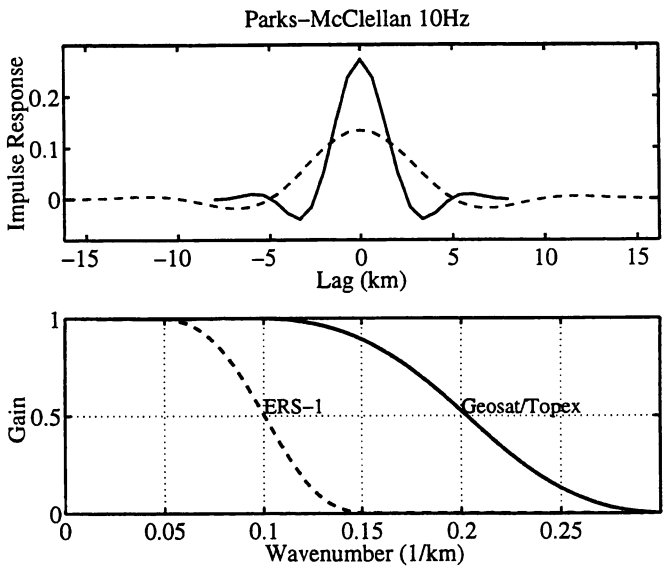

Figure 4.2: Filters applied to 10 Hz data (solid, Geosat and TOPEX; dashed, ERS-1). (Top) The impulse response; (bottom) the gain. ERS-1 data are noisier and thus require a longer filter (49 points versus 25 points for Geosat and TOPEX).

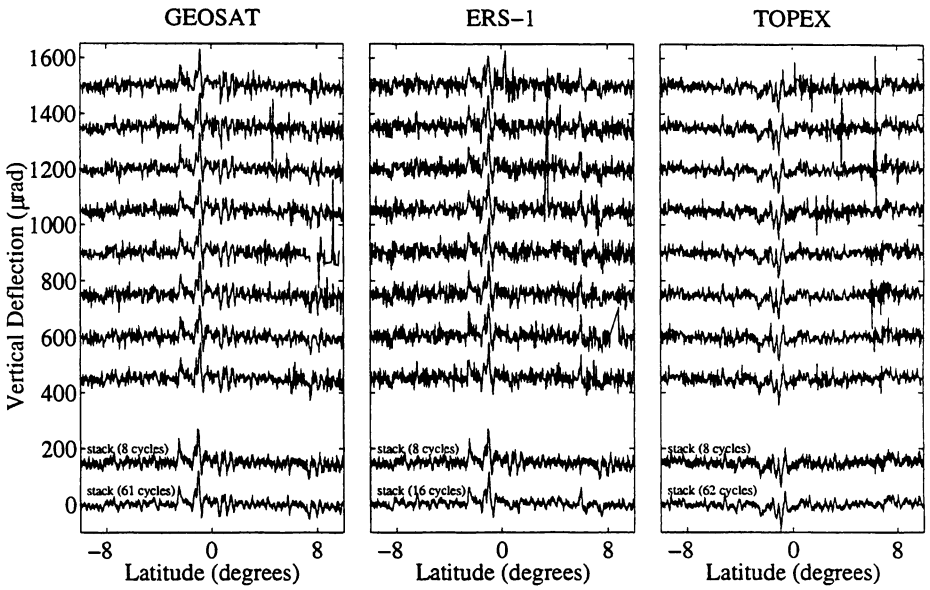

Figure 4.3: Individual and stacked vertical deflection profiles for a track crossing the Mid-Atlantic Ridge (thick line in area 1, Figure 4.1b). Only eight of the available individual cycles are shown for each satellite. TOPEX profiles have opposite sign from Geosat and ERS-1 because TOPEX was in a prograde orbit while the other satellites were in retrograde orbit. The ERS-1 stack is less well determined because ERS-1 has the fewest cycles to stack. Note that individual ERS-1 data are noisier than Geosat and TOPEX data when all contain the same frequency content.

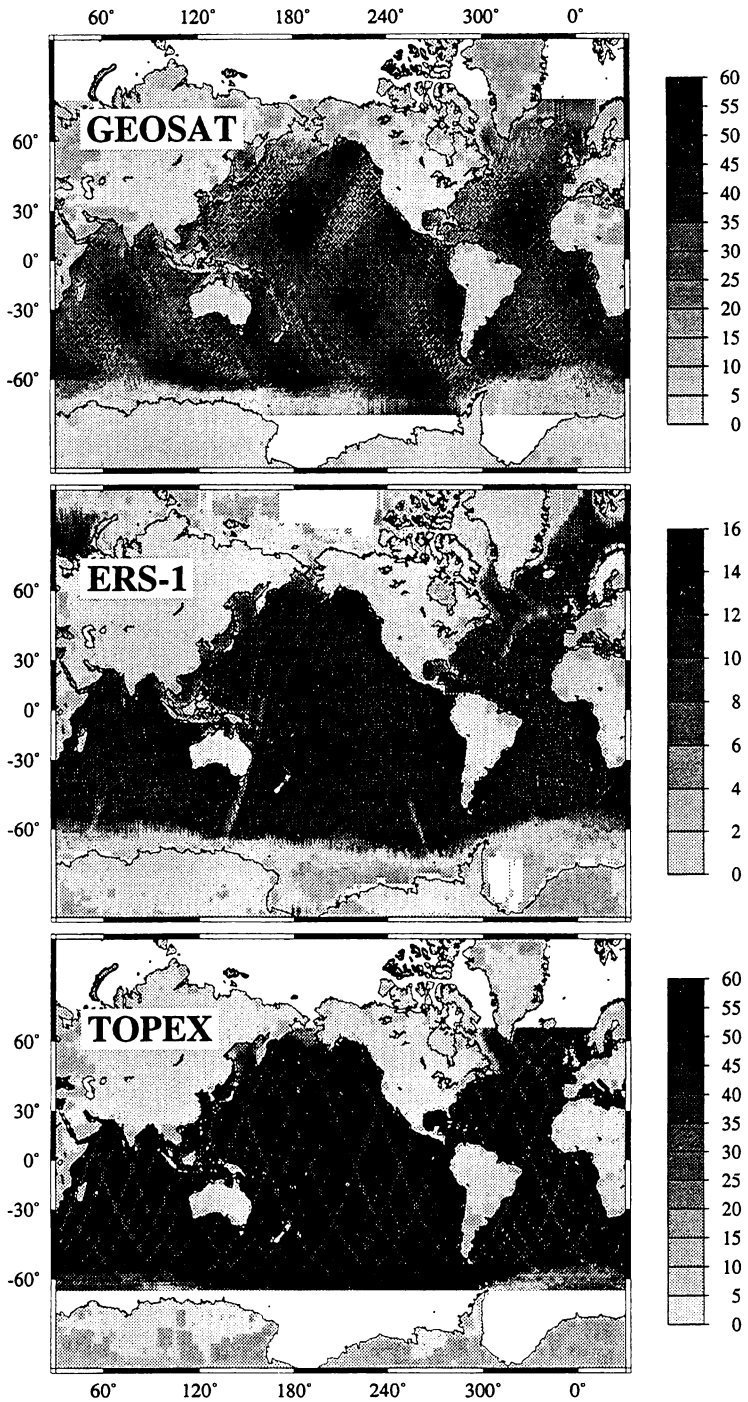

Figure 4.4: Number of cycles in stack for each of the satellites. Geosat, 62 possible cycles; ERS-1, 16 possible cycles; TOPEX, 62 possible cycles.

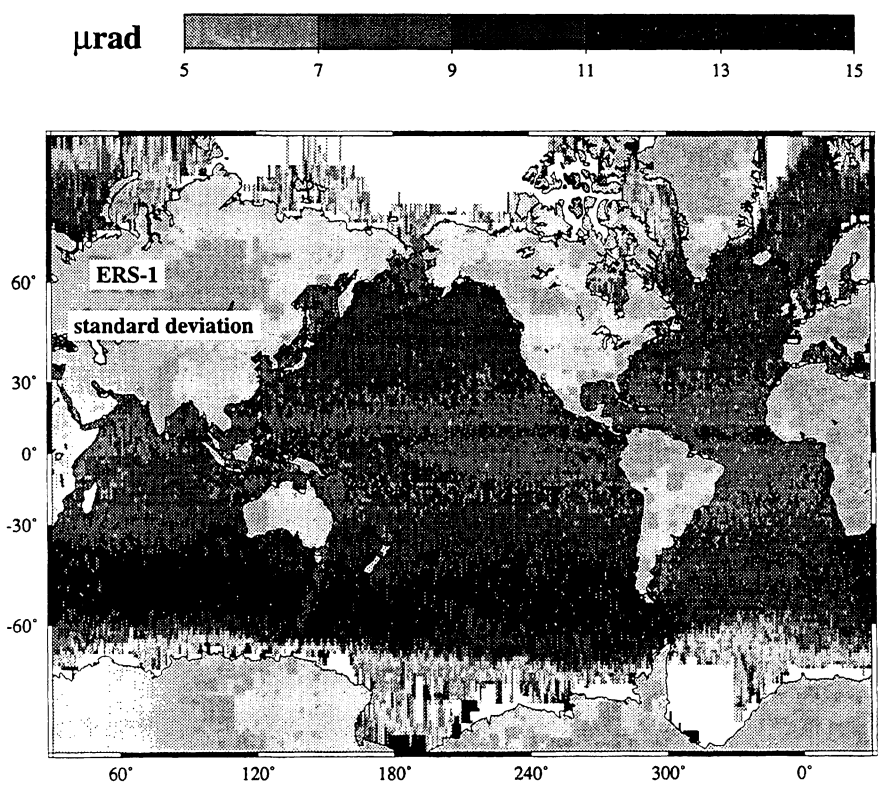

Figure 4.5: Standard deviation about the mean (stack) for ERS-1, reflects short-wavelength altimeter noise and altimeter noise due to high sea-state.

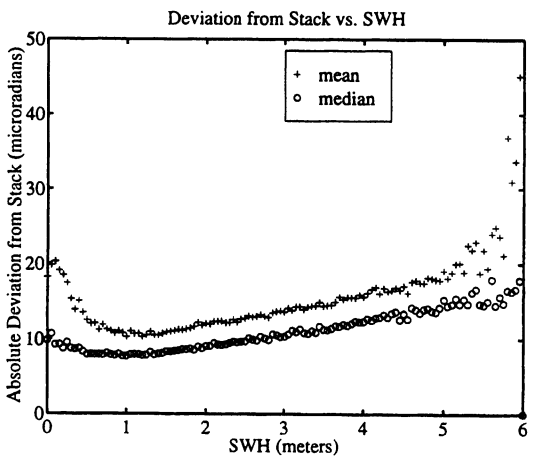

Figure 4.6: Absolute deviation from the stack versus significant wave height for ERS-1.

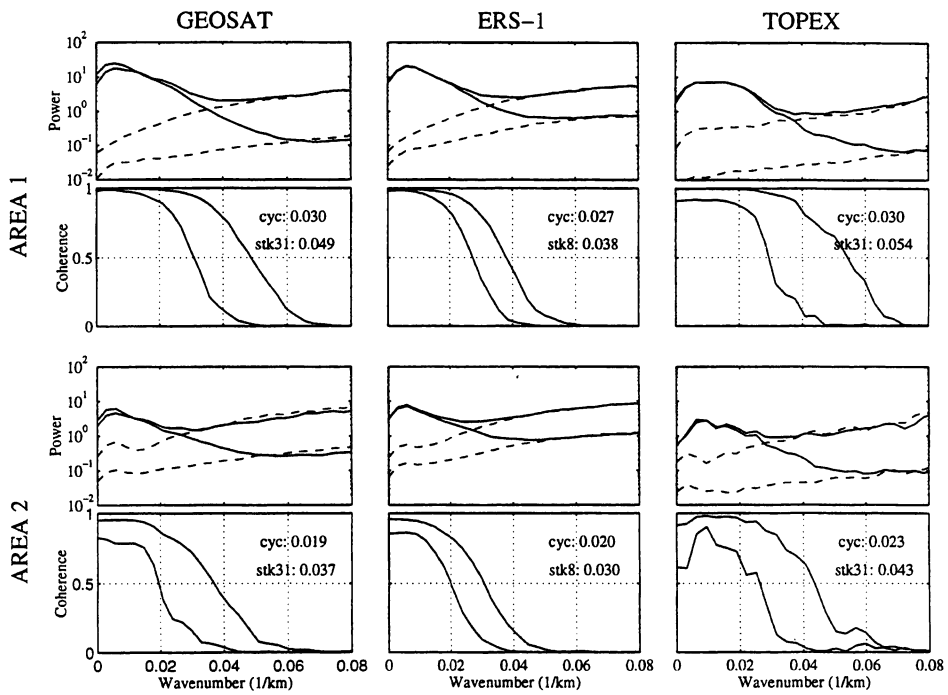

Figure 4.7: Power spectra and coherence curves for individual cycles and half stacks of Geosat (31 cycles), ERS-1 (8 cycles), and TOPEX (31 cycles) in area 1 (high signal, low noise) and area 2 (low signal, high noise); Figure 4.1b shows locations. Solid lines are power in the signal plus the noise, and dashed lines are power in the noise; the upper solid and dashed line are for an individual cycle pair, while the lower solid and dashed line are for a pair of half stacks. The wave number where the coherence is 0.5 is indicated on each coherence plot for individual cycles and half stacks.

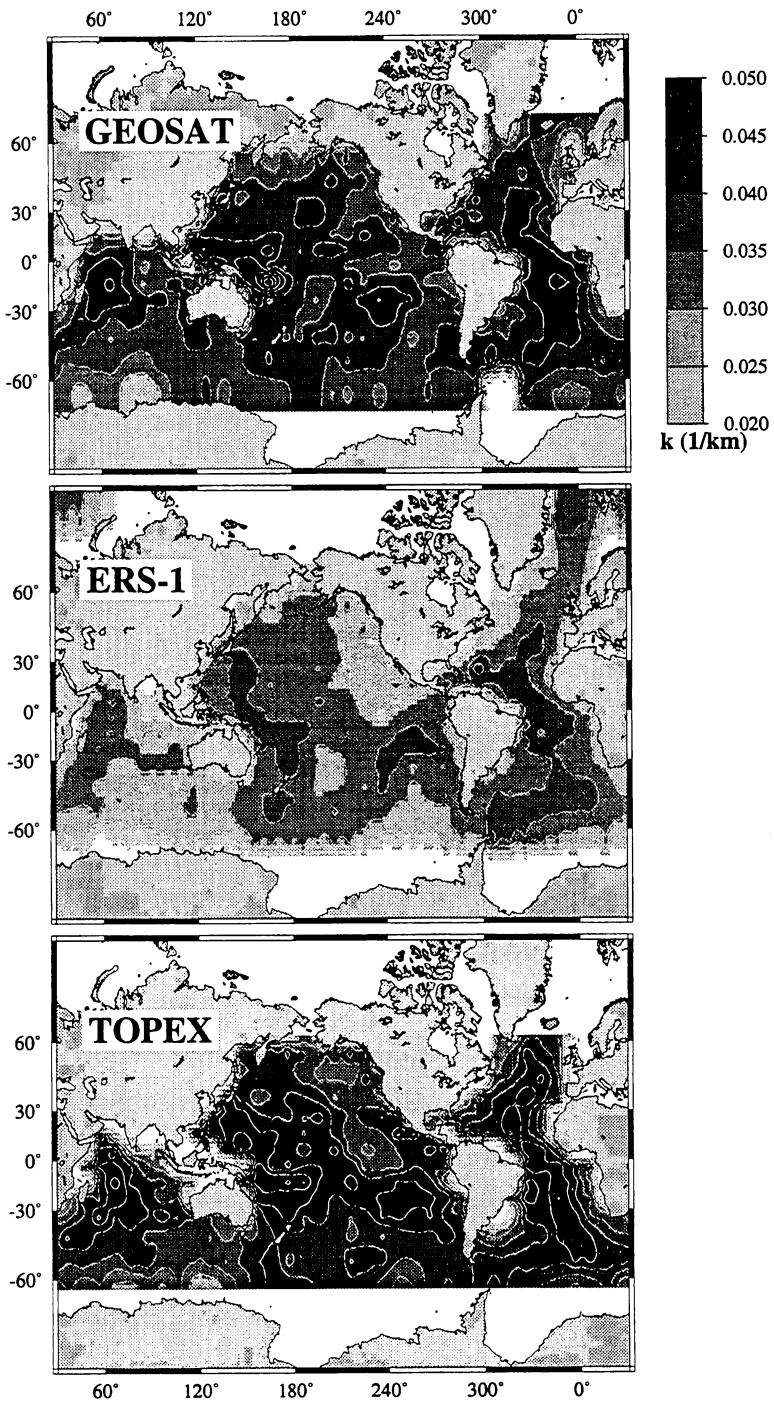

Figure 4.8: Resolution (0.5 coherence) as a function of geographic position. Shorter wavelengths are resolved in darker areas.

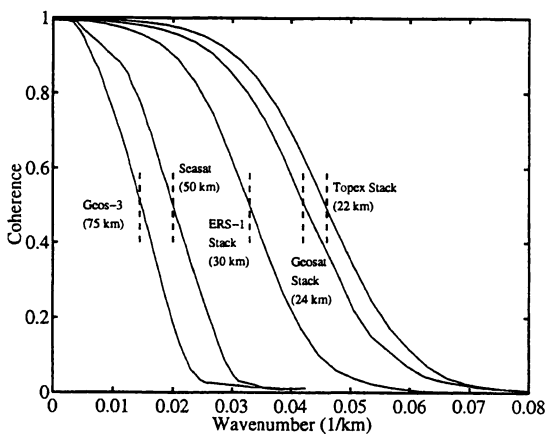

Figure 4.9: Comparison of coherences for single profiles of GEOS-3 and Seasat, along with stacked ERS-1 (eight cycles), Geosat (31 cycles), and TOPEX (31 cycles) profiles. GEOS-3 and Seasat results are from Marks and Sailor [1986]. Stacked Geosat, ERS-1, and TOPEX results are global averages.

4.7 References

Born, G. H., J. L. Mitchell, and G. A. Heyler, 1987. Design of the Geosat exact repeat mission. *Johns Hopkins APL Tech. Dig.*, **8**, 260-266.

Brammer, R. F., 1979. Estimation of the ocean geoid near the Blake Escarpment using GEOS-3 satellite altimetery data. *J. Geophys. Res.*, **84**, 3843-3851.

Cheney, R. E., et al., 1991. *The Complete Geosat Altimeter GDR Handbook.* National Geodetic Survey, NOAA, Rockville, MD.

Laxon, S., and D. McAdoo, 1994. Arctic Ocean gravity field derived from ERS-1 satellite altimetry. *Science*, **265**, 621-624.

Levitus, S., 1982. *Climatological Atlas of the World Ocean.* U.S. Dep. of Commer., Rockville, MD.

Marks, K. M., and R. V. Sailor, 1986. Comparison of GEOS-3 and Seasat altimeter resolution capabilities. *Geophys. Res. Lett.*, **13**, 697-700.

Marks, K. M., D. C. McAdoo, and W. H. F. Smith, 1993. Mapping the Southwest Indian Ridge with Geosat. *Eos Trans. AGU*, **74**, 81.

Marsh, J. G., and T. V. Martin, 1982. The Seasat altimeter mean sea surface model. *J. Geophys. Res.*, **87**, 3269-3280.

McAdoo, D. C., and K. M. Marks, 1992a. Gravity fields of the southern ocean from Geosat data. *J. Geophys. Res.*, **97**, 3247-3260.

McAdoo, D. C., and K. M. Marks, 1992b. Resolving marine gravity with ERS-1 satellite altimetry. *Geophys. Res. Lett.*, **19**, 2271-2274.

Neumann, G. A., D. W. Forsyth, and D. Sandwell, 1993. Comparison of marine gravity from shipboard and high-density satellite altimetry along the Mid-Atlantic Ridge, 30.5° -35.5° S. *Geophys. Res. Lett.*, **20**, 1639-1642.

Rousseeuw, P. W., and A. M. Leroy, 1987. *Robust Regression and Outlier Detection.* John Wiley, New York, 329 pp.

Sailor, R. V., 1982. Determination of the resolution capabilities of the Seasat radar altimeter, observations of the geoid spectrum, and detection of seamounts,

report, Atlantic Sci. Corp..

Sandwell, D. T., 1992. Antarctic marine gravity field from high-density satellite altimetry. *Geophys. J. Int.*, **109**, 437-448.

Sandwell, D. T., and D. C. McAdoo, 1988. Marine gravity of the southern oceans and Antarctic margin from Geosat. *J. Geophys. Res.*, **93**, 10,389-10,396.

Sandwell, D. T., and D. C. McAdoo, 1990. High-accuracy, high-resolution gravity profiles from 2 years of the Geosat exact repeat mission. *J. Geophys. Res.*, **95**, 3049-3060.

Sandwell, D. T., and W. H. F. Smith, 1992. Global marine gravity from ERS-1, Geosat and Seasat reveals new tectonic fabric. *Eos Trans. AGU*, **73 (44) Fall Meet. Suppl.**, 133.

Smith, W. H. F., and D. T. Sandwell, 1994. Bathymetric prediction from dense satellite altimetry and sparse shipboard bathymetry. *J. Geophys. Res.*, **99**, 21803-21824.

Welch, P. D., 1967. The use of fast Fourier transforms for the estimation of power spectra: a method based on time averaging over short, modified periodograms. *IEEE Trans. Audio Electroacoust.*, **15**, 70-73.

Wessel, P. and W. H. F. Smith, 1991. Free software helps map and display data. *Eos Trans. AGU*, **72**, 441-446.

Chapter 5

Improved Marine Gravity Profiles from Geosat, ERS-1/2 and Topex Satellite Altimeters

5.1 Abstract

We have developed a method to improve global gravity grids by iterating on the current grid derived from Geosat and ERS-1 geodetic mission data and repeat cycle data. The *Sandwell and Smith* [1997] V7.2 global gravity grid maximizes the 2-D resolution by combining dense individual altimeter profiles with sparse but more accurate stacked profiles. However, to make the best 2-D grid, data were averaged and filtered such that some of the 1-D resolution was lost along repeat profiles. A 1-D transformation retains full resolution along stacked profiles, but assumes that the gravity field is aligned perpendicular to the profile. We use the 2-D gravity grid to constrain the gravity field along the profile for all but the shortest wavelengths. The 1-D transformation is then applied to the difference between the stacked profiles and the 2-D grid along the same ground tracks.

We use new repeat cycle data to improve stacks (averages) for ERS-1/2 (43

cycles) and Topex (142 cycles), and then implement the method for improving gravity profiles globally. We demonstrate the maximum accuracy of our new grid by comparing the grid to ship profiles, aligned with ERS track lines that cross the Pukapuka volcanic ridges in the Pacific. The improved grid reduces the RMS difference ($\sim 3\mu$rads) between ship and satellite profiles by 6-11% overall and the new method recovers up to 20% more amplitude of sharp gravity features than the V7.2 grid.

These highly accurate profiles and grids are useful for detailed studies of seamounts and lithospheric flexure. Improvement will be greatest in shallow regions where the short wavelength gravity anomalies are attenuated less. Greatest improvements will be achieved by combining available shipboard gravity profiles with these new stacked profiles and the V7.2 grid. New satellite gravity grids may also be differenced from ship gravity to determine absolute dynamic topography across sharp ocean fronts.

5.2 Introduction

Satellite altimetry has allowed marine geodesists and geophysicists to recover the marine gravity field globally at 10 km resolution [*Sandwell and Smith*, 1997]. Their most recent global gravity grid V7.2 was created by combining data from the Geosat and ERS-1 satellites. Each satellite operated in a geodetic mission, covering the Earth with closely spaced ground tracks (Geosat, 6 km; ERS-1, 8 km) and in a repeat cycle mode, covering the Earth many times with more sparsely spaced ground tracks. The repeat mode allows for stacking or averaging many repeat profiles which improves along-track resolution over individual profiles [*Yale et al.*, 1995]. *Yale et al.* [1995] compared the resolution of individual and stacked profiles for three satellites, Geosat, ERS-1 and Topex, and the results were used to design post-stack filters for gridding the two-dimensional (2-D) gravity field.

In creating the V7.2 grid, data from the different satellites were combined to make the grid isotropic. Some information along the repeat profiles was lost in this process. We present a method for using the V7.2 grid to improve along-track resolution and accuracy of stacked profiles. The method is implemented on global datasets of stacked profiles from Geosat, ERS-1/2, and Topex. ERS-1/2 and Topex have continued to operate in a repeat cycle mode providing more cycles for stacking than were available in our previous study [*Yale et al.*, 1995]. Using many more profiles in the stack improves the signal to noise ratio, especially for the noisier ERS data.

5.3 Data

We restack ERS 35-day repeat cycle data using all available cycles (43). At the time of the *Yale et al.* [1995] resolution analysis, we only had 16 cycles of ERS-1 data. Since that time, ERS-2 was launched in April 1995, and ERS-2 and ERS-1 operated simultaneously in a tandem mission, repeating the same ground track one day apart. We use 28 cycles of ERS-1 data: 17 cycles from the first 35-day phase of the mission, phase C cycles 2-18 from May 15, 1992 to December 26, 1993, and 11 cycles from the tandem phase of the mission, phase G cycles 2-4 and 6-13 from April 7, 1995 to June 1, 1996. We use 15 cycles of ERS-2 data: cycles 2-16 from June 16, 1995 to November 23, 1996, starting during the tandem mission. Data from ERS-1 phase C cycle 1 was excluded as its orbit deviated by 2-3 km from the other orbits. For all ERS data, we incorporate the most recent orbits calculated by Delft Institute for Earth-Oriented Space Research which are based on their new gravity model DGM-E04 and provides orbits with a radial precision of 5 cm [*Scharroo et al.*, 1997].

We restacked the Topex 10-day repeat cycle data (142 cycles) using all Topex cycles from 1-156 from September 22, 1992 to December 18, 1996. Poseidon only

cycles are excluded (20, 31, 41, 55, 65, 79, 91, 97, 103, 114, 126, 138, 150) as is cycle 118, when there was a problem with the altimeter.

We follow the same editing and preprocessing steps as described in *Yale et al.* [1995] creating new stacked profiles of vertical deflection for ERS and Topex. Geosat stacked vertical deflection profiles are those created by *Yale et al.* [1995] with 66 cycles.

The most important environmental correction to sea surface slope is the ocean tide (see appendix on Topex Corrections). The Center for Space Research (CSR) composite ocean tide model V3.0 [*Bettadpur and Eanes*, 1994] is superior to the tides supplied with the ERS and Topex data. We applied the CSR V3.0 tide model to ERS and Topex data. The CSR V3.0 model was also applied to Geosat and ERS-1 geodetic mission data before creating the global gravity grid V7.2 [*Sandwell and Smith*, 1997].

We repeated the significant wave height (SWH) analysis [*Yale et al.*, 1995] for ERS-1/2 data with our more robustly determined stack and conclude that our previous decision to edit ERS-1 data with SWH greater than 6 m is valid. This cutoff eliminates less than 0.9% of the ERS data which on average deviates from the stack by more than 15 μrads.

Maps of the number of cycles stacked for all three satellites are presented in Figure 5.1. The ERS stacks now have approximately 40 cycles globally which compares well with Geosat stacks. Topex stacks have more than 100 cycles globally and the noise on these profiles will be the smallest of the three satellite orbits, however the large track spacing makes the Topex tracks less useful for gridding than ERS and Geosat profiles. As shown by *Yale et al.* [1995], the power of the noise falls off approximately linearly with the number of cycles stacked.

5.4 Iteration on Gravity Grid

After creating the new stacked profiles, we use them to iterate on the *Sandwell and Smith* [1997] V7.2 global gravity grid. The procedure is similar to that used by *Small and Sandwell* [1992] however instead of subtracting only a spherical harmonic model of the gravity field, we subtract the V7.2 gravity grid as the best estimate of the 2-D gravity field. We then perform the one-dimensional (1-D) transformation described below in equation (5.12) and add the residual gravity back to the V7.2 grid.

The geoid height $N(\mathbf{x})$, gravity anomaly $\Delta g(\mathbf{x})$, and other measurable quantities are related to the gravitational potential $\phi(\mathbf{x}, z)$ [*Heiskanen and Moritz*, 1967]. We assume that all of these quantities are deviations from a reference Earth model so a flat Earth approximation can be used for the gravity computation (5.11). In the following equations, the position $\mathbf{x} = (x, y)$, and the wavenumber $\mathbf{k} = (k_x, k_y)$ where $k_x = 1/\lambda_x$ and λ_x is wavelength. To a first approximation, the geoid height is related to the gravitational potential by Brun's formula

$$N(\mathbf{x}) \cong \frac{1}{g_0}\phi(\mathbf{x}, 0) \tag{5.1}$$

where g_0 is the average acceleration of gravity (9.81 ms^{-2}). The gravity anomaly is

$$\Delta g(\mathbf{x}) = -\frac{\partial \phi(\mathbf{x}, 0)}{\partial z} \tag{5.2}$$

The east component of vertical deflection is

$$\eta(\mathbf{x}) \equiv -\frac{\partial N}{\partial x} \cong \frac{-1}{g_0}\frac{\partial \phi}{\partial x} \tag{5.3}$$

The north component of vertical deflection is

$$\xi(\mathbf{x}) \equiv -\frac{\partial N}{\partial y} \cong \frac{-1}{g_0}\frac{\partial \phi}{\partial y} \tag{5.4}$$

Laplace's equation relates these three partial derivatives of the gravitational potential.

$$\frac{\partial^2 \phi}{\partial x^2} + \frac{\partial^2 \phi}{\partial y^2} + \frac{\partial^2 \phi}{\partial z^2} = 0 \tag{5.5}$$

Substitution of (5.2),(5.3) and (5.4) into Laplace's equation (5.5) yields

$$\frac{\partial \Delta g}{\partial z} = -g_0 \left[\frac{\partial \eta}{\partial x} + \frac{\partial \xi}{\partial y}\right] \tag{5.6}$$

Vertical gravity gradient can be computed from grids of east and north vertical deflection [*Rummel and Haagmans*, 1990].

Following *Haxby et al.* [1983], the differential equation (5.6) reduces to an algebraic equation when Fourier transformed. The forward and inverse Fourier transforms are

$$F(\mathbf{k}) = \int_{-\infty}^{\infty}\int_{-\infty}^{\infty} f(\mathbf{x}) \exp[-i2\pi(\mathbf{k}\cdot\mathbf{x})] d^2\mathbf{x} \tag{5.7}$$

$$f(\mathbf{x}) = \int_{-\infty}^{\infty}\int_{-\infty}^{\infty} F(\mathbf{k}) \exp[i2\pi(\mathbf{k}\cdot\mathbf{x})] d^2\mathbf{k} \tag{5.8}$$

The Fourier transform of equation (5.6) is

$$\frac{\partial \Delta g(\mathbf{k}, z)}{\partial z} = -i2\pi g_0 [k_x \eta(\mathbf{k}) + k_y \xi(\mathbf{k})] \tag{5.9}$$

Solving Laplace's equation in the wavenumber domain yields the upward continuation formula, which relates the gravity anomaly at the Earth's surface to the gravity anomaly at some elevation z.

$$\Delta g(\mathbf{k}, z) = \Delta g(\mathbf{k}, 0) \exp[-2\pi|\mathbf{k}|z] \tag{5.10}$$

5.5 Analysis of new grid and stacks

These new profiles can be used to refine the grids of gravity globally. We examine an area including the Pukapuka volcanic ridges to assess the improved accuracy and short wavelength resolution of the new grids (Figure 5.2). This region was surveyed [*Sandwell et al.*, 1995] and modeled [*Goodwillie*, 1995] as a zone of unusually low elastic plate thickness, possibly indicating diffuse extension of the lithosphere. In this region there are eight profiles which are aligned closely with satellite repeat tracks (Figure 5.3). This is a region where the new gravity profiles will likely show the most improvement because the ridges have very narrow gravity expressions which are not well resolved in the V7.2 grid. In addition, the ridges are nearly perpendicular to the satellite tracks so the 1-D approximation is good. The improvement in profiles is hard to resolve at the scale of Figure 5.2, although the residual grid (Figure 5.4) shows the short wavelength information captured by the stacked altimeter profiles.

We extract gravity from the new grid V7.2plus along the eight ship profiles to compare ship and satellite gravity. Profiles 3 and 4 lie precisely on ERS tracks. These profiles show the most improvement over the gravity grid V7.2 (Figures 5.5 and 5.6) which included a 16 cycle stack of ERS-1 data. The new 43 cycle stack recovers more of the amplitude of the short wavelength volcanic ridges. For Profile 3, the new grid recovers 10% more of the amplitude of the highest peak than does V7.2. For profile 4, both large amplitude peaks are recovered more by the V7.2plus grid than by the V7.2 grid, 12% for the southern peak and 20% for the northern peak. We computed the RMS difference between the V7.2 profile and the ship profile and between the V7.2plus profile and the ship profile. For profiles 3 and 4, the RMS differences decreased 6% and 11% respectively when using grid 7.2plus. See Table 5.1. The mean offset between ship profiles and satellite profiles is probably due to ship profiles being inadequately corrected for the absolute gravity at their tie points [*Wessel and Watts*, 1988].

We also examined the other 6 profiles in this region. These profiles were not perfectly aligned along repeat tracks and therefore largely sample the V7.2 grid. All profiles show the same trend of increasing the amplitude of the highest peaks. The RMS difference sometimes increases as for profiles 5 and 8. This is probably due to the unfiltered short wavelength altimeter noise introduced by the stacked profiles; the V7.2 grid retains wavelengths longer than 25 km while the stacked profiles retain wavelengths longer than 18 km.

We present the new grid for the Caspian Sea to demonstrate the value of additional data in a remote region. Repeat satellite ground tracks for the three orbits are shown in Figure 5.7. The grid of residual gravity is presented to illustrate where the profiles add information (Figure 5.8). There are a couple of worrisome features in this residual grid along two descending Geosat tracks. In the west, a large residual anomaly just north of the peninsula is probably due to some land data which our editing missed. In the southeast, a Geosat track and a Topex track are nearly coincident, and differences between the two force the gridding algorithm to create a sharp jump in the residual grid. To make a final improved grid for this region or other similar land-locked regions would require manual editing of problematic data. One of the advantages of this approach is that each profile can be examined for outliers. Then the stacked profiles can be gridded together with available shipboard gravity profiles and sparse samples from the V7.2 grid to create the best accuracy and resolution. Petroleum exploration companies are particularly interested in this approach. To observe the improvement in the grid for this region, compare the V7.2 grid (Figure 5.9) to the new grid (Figure 5.10).

	Ship-V7.2		Ship-V7.2plus		
Profile	Mean (mgal)	RMS (mgal)	Mean (mgal)	RMS (mgal)	% change RMS
1	10.0	3.15	10.1	3.21	1.67
2	9.7	3.59	9.4	3.65	1.60
3	18.6	3.69	18.7	3.44	-6.18
4	18.2	3.78	18.4	3.40	-11.22
5	18.1	3.29	18.2	3.75	12.06
6	20.2	4.72	19.6	4.66	-1.28
7	-2.1	3.43	-2.3	3.45	0.77
8	19.0	3.00	19.7	3.29	8.73

Table 5.1: The large mean differences are due to incorrect DC level of ship data [*Wessel and Watts*, 1988].

5.6 Summary

Sandwell and Smith [1997] showed their V7.2 grid has an RMS accuracy of 3-6 mgal depending on the proximity to a stacked profile. This is consistent with an independent RMS accuracy estimate (3-9 mgal) of the V7.2 grid performed by *Marks* [1996]. The eight profiles examined in the Pukapuka region reflect the most accurate portions of the V7.2 grid, with the smallest RMS difference between ship and satellite gravity. The method we present here for iterating on the V7.2 grid with stacked profiles improves the amplitude recovery of short wavelength gravity anomalies, where stacked profiles are available. The best improvement from our new grid is likely to be in shallow regions where the upward continuation from the seafloor is minimized, and the shortest wavelength anomalies can be resolved at the sea-surface.

We are experimenting with different along-track, post stack filters to retain

the shortest possible wavelengths along track, while eliminating noise. We are awaiting ship profiles from Edcon Inc. which we will use to further evaluate the improved ERS-1/2 profiles in the Gulf of Mexico, and to tune the low pass filters.

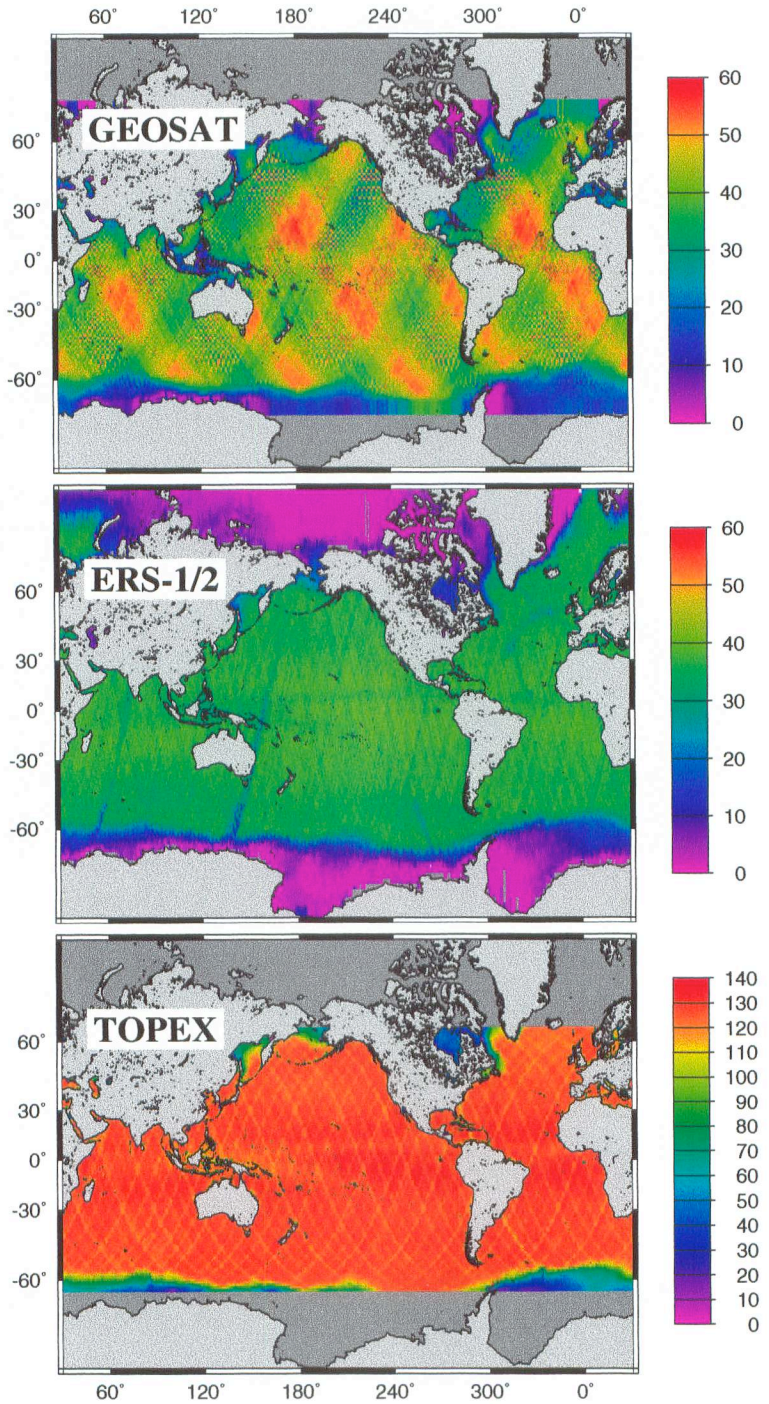

Figure 5.1: Number of cycles in stack for each of the satellites. Geosat, 62 possible cycles; ERS-1/2, 43 possible cycles; TOPEX, 142 possible cycles.

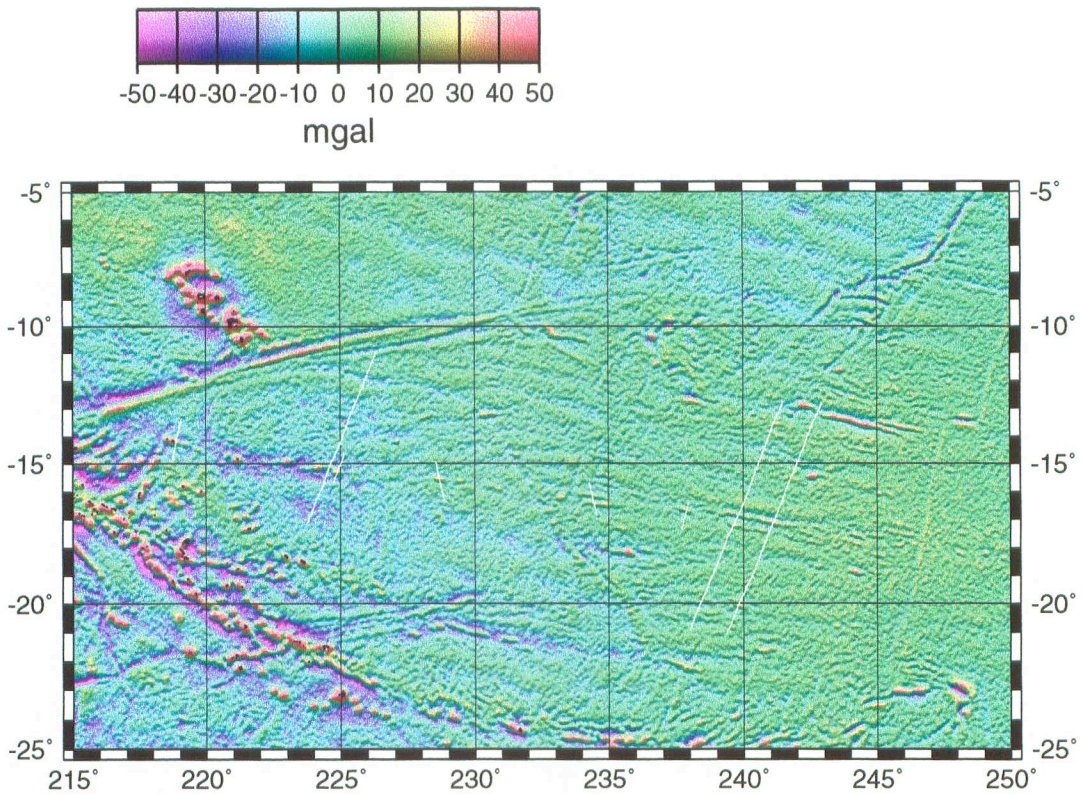

Figure 5.2: Improved gravity grid for Pukapuka volcanic region in the Pacific Ocean. White lines indicate eight ship tracks which are compared to satellite gravity; the profiles are numbered 1-8 from east to west.

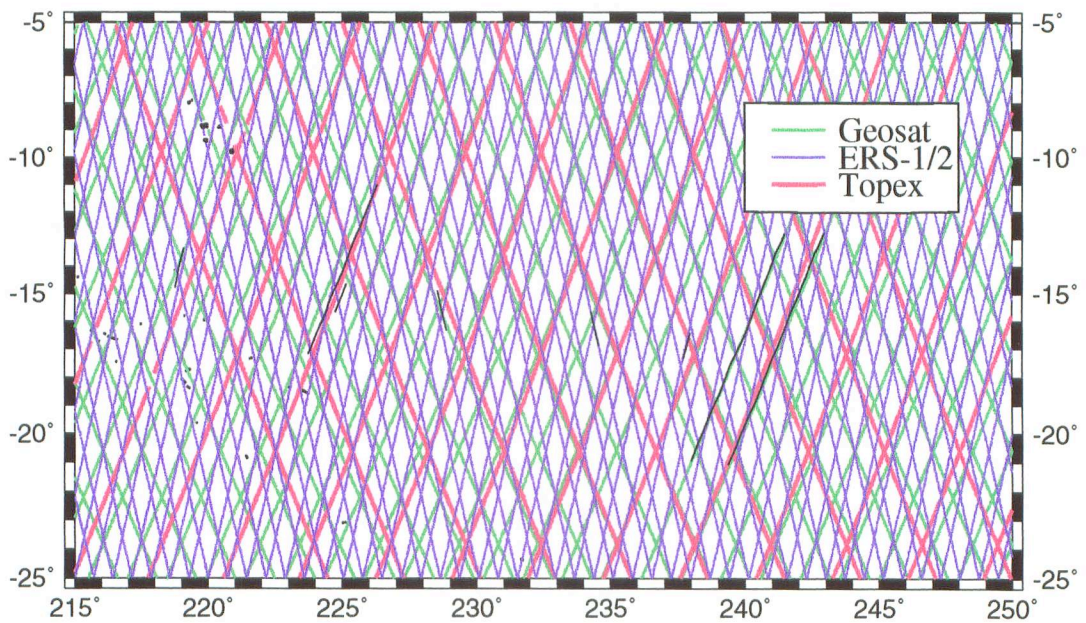

Figure 5.3: Satellite ground tracks for repeat profiles in the Pukapuka region illustrate the density of coverage and intersection of different satellites. Short black lines are the eight ship tracks shown in white in Figure 5.2.

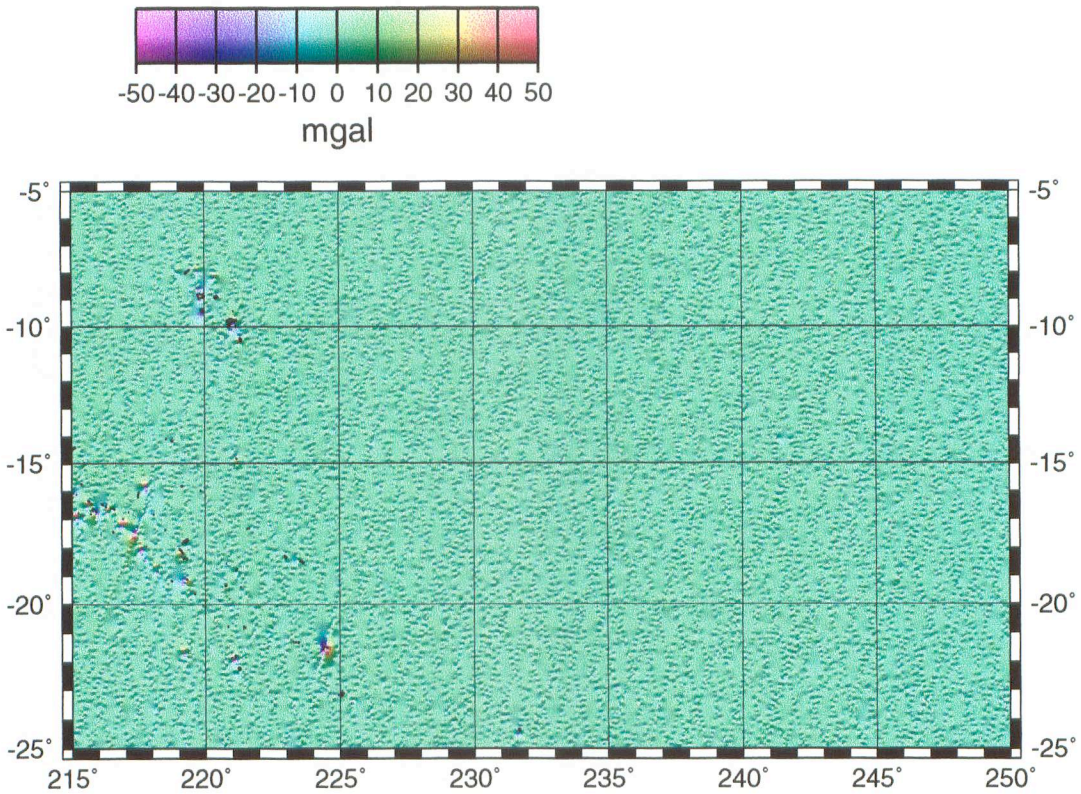

Figure 5.4: Grid of residual gravity anomalies for the Pukapuka region show that the largest residuals occur near the seamounts in the southwestern corner of the region, where the short wavelength gravity anomalies have the largest amplitudes.

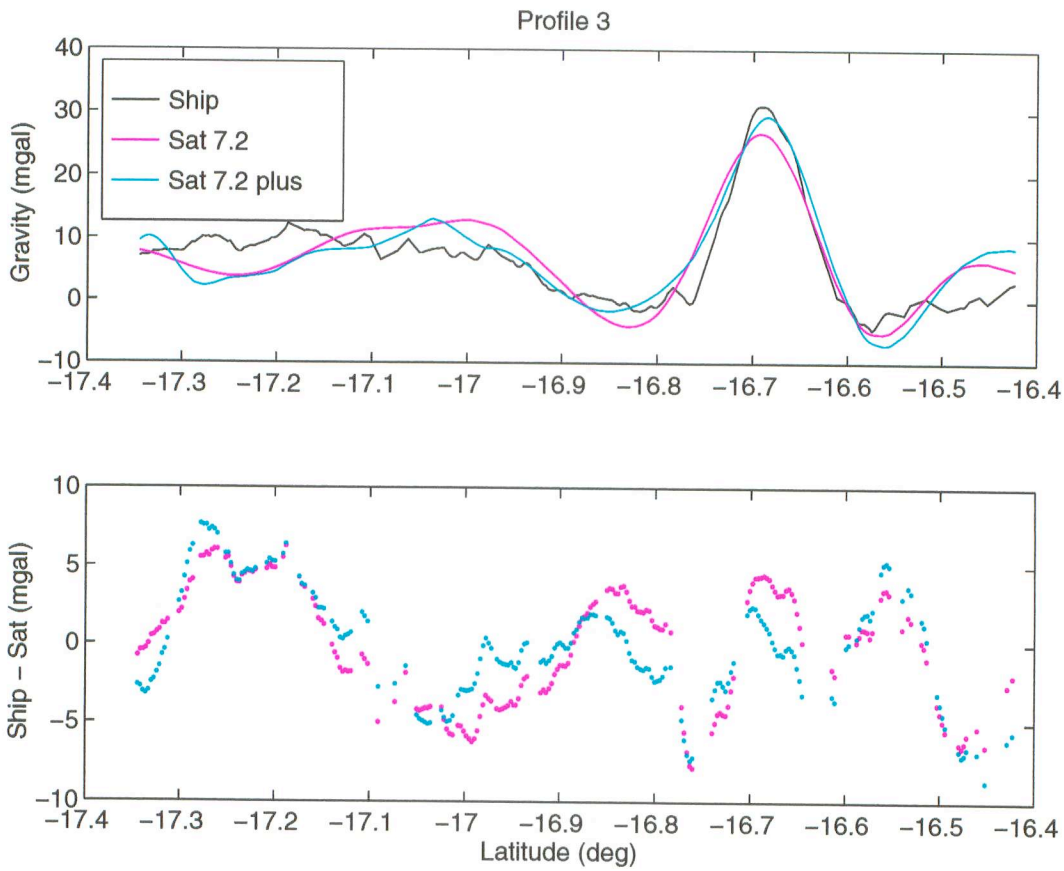

Figure 5.5: Comparison between ship gravity and satellite gravity along Profile 3 in the Pukapuka region. The improved satellite profile (blue) recovers more of the amplitude of the peak than does the V7.2 profile (red).

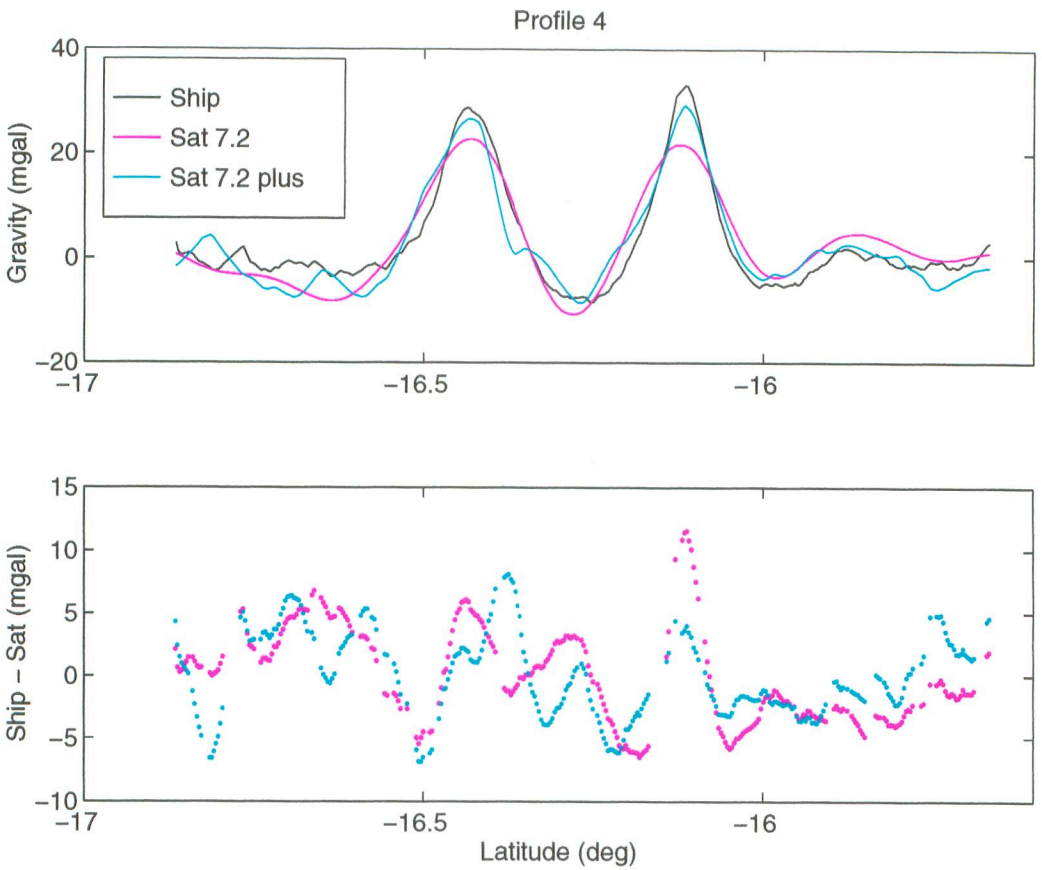

Figure 5.6: Comparison between ship gravity and satellite gravity along Profile 4 in the Pukapuka region. The improved satellite profile (blue) recovers more of the amplitude of both peaks than does the V7.2 profile (red).

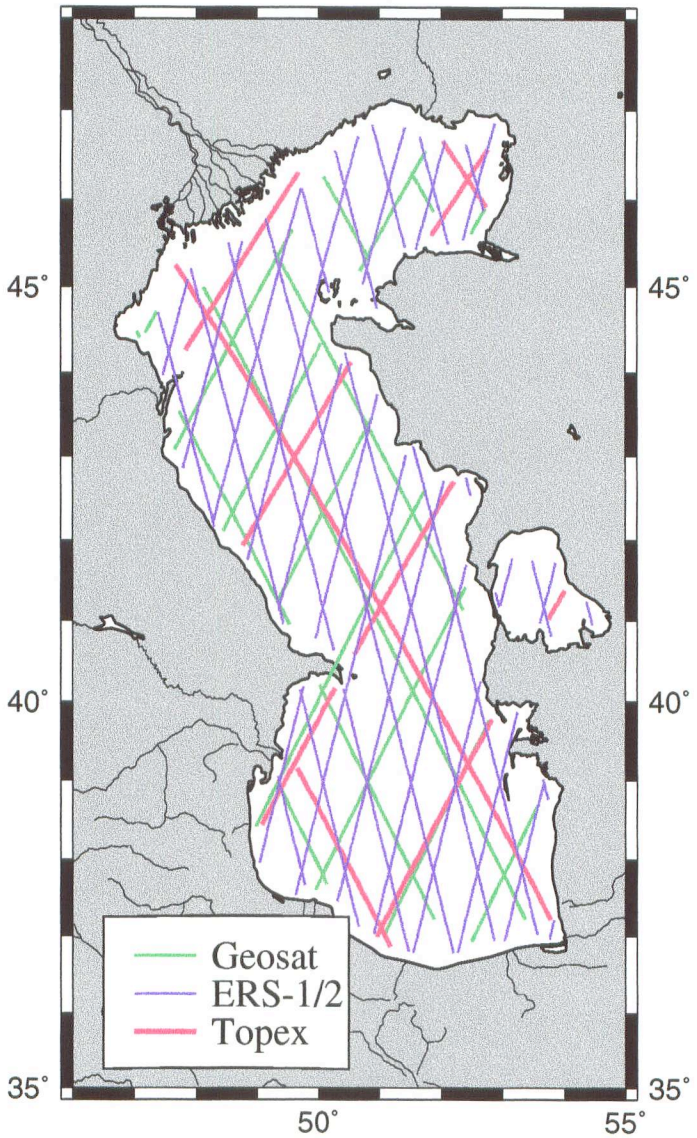

Figure 5.7: Satellite ground tracks for repeat profile in the Caspian Sea are needed to interpret the residual gravity profiles shown in the following figures.

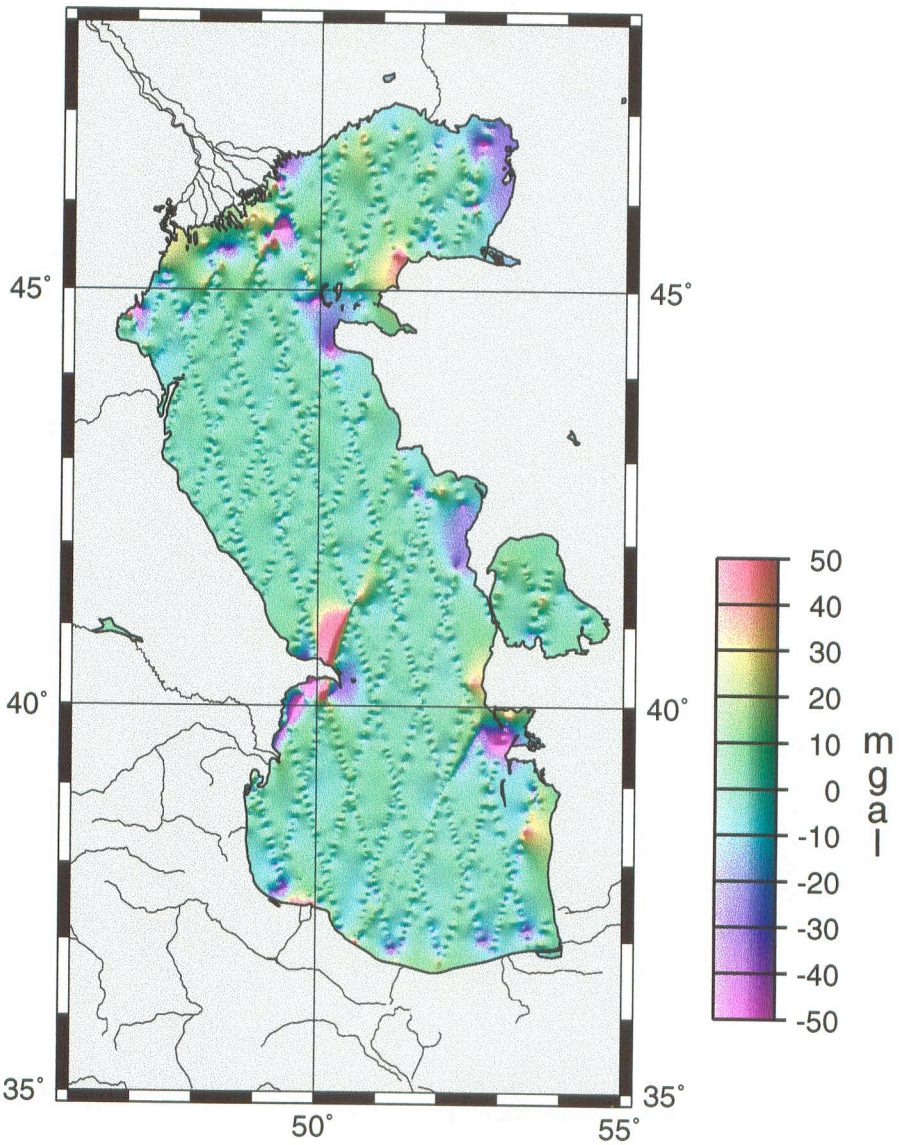

Figure 5.8: Residual gravity grid in Caspian Sea.

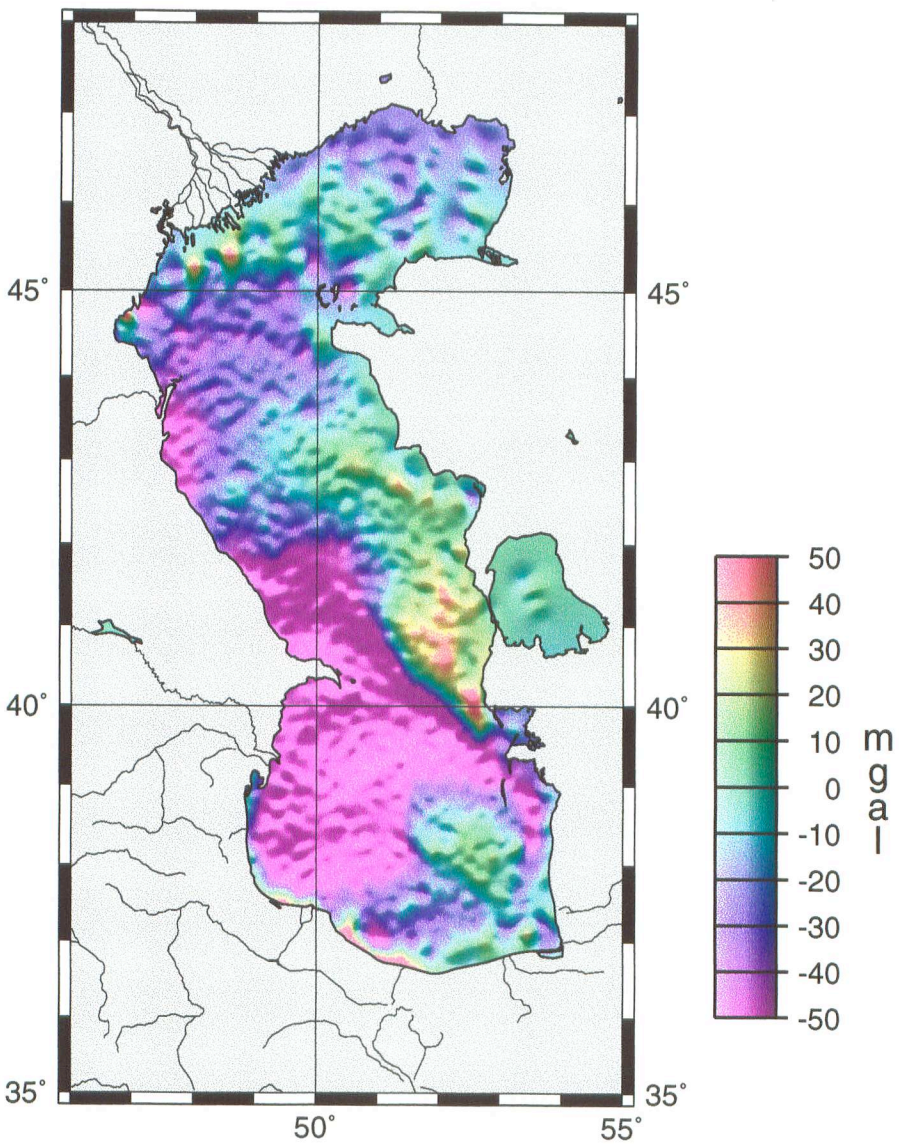

Figure 5.9: Gravity grid V7.2 in Caspian Sea.

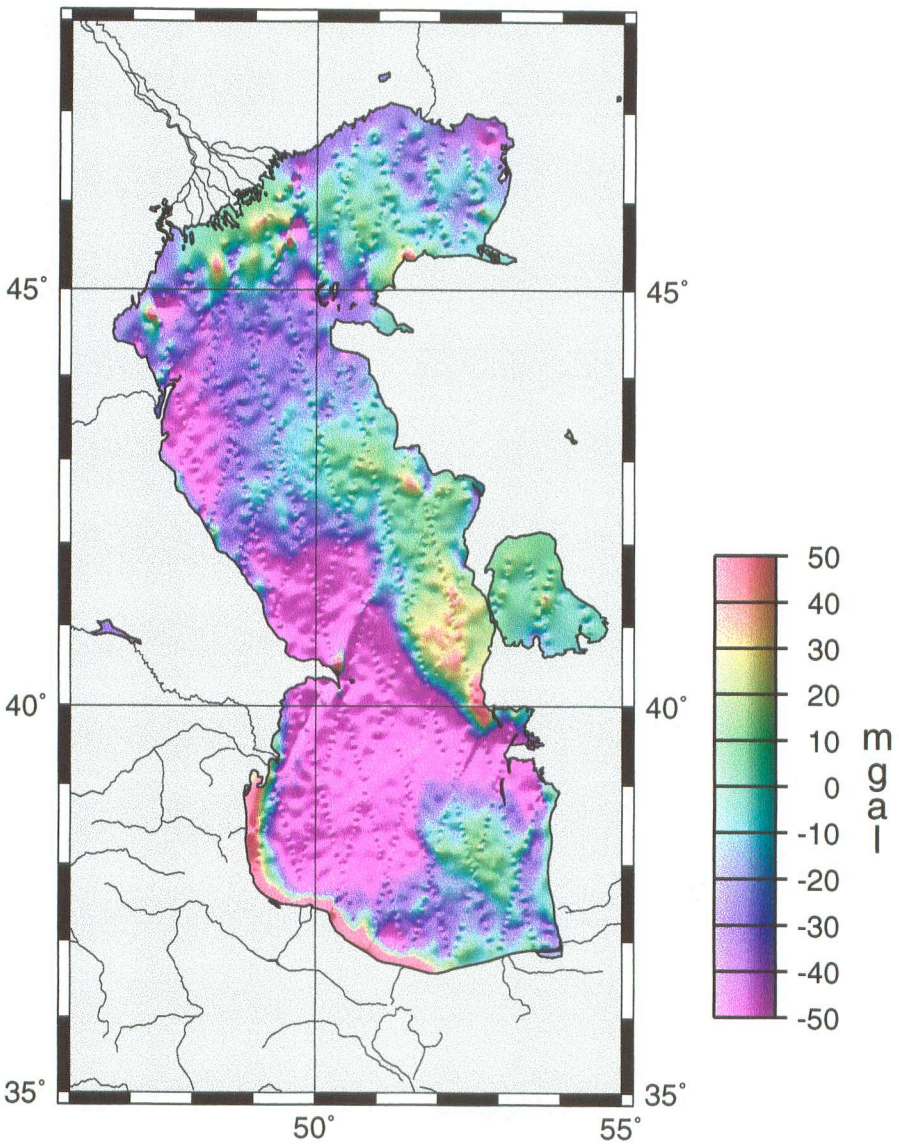

Figure 5.10: Improved gravity grid (V7.2plus) in Caspian Sea.

5.7 References

Bettadpur, S.V., and R.J. Eanes, 1994. Geographic representation of radial orbit perturbations due to ocean tides: Implications for satellite altimetry. *J. Geophys. Res.*, **99**, 24,883-24,898.

Haxby, W.F., G.D. Kramer, J.L. LaBrecque, and J.K. Weissel, 1983. Digital images of combined oceanic and continental data sets and their use in tectonic studies. *EOS Trans. Amer. Geophys. Un.*, **64**, 995-1004.

Goodwillie, A.M., 1995. Short-wavelength gravity lineations and unusual flexure results at the Puka Puka volcanic ridge system. *Earth Planet. Sci. Lett.*, **136**, 297-314.

Heiskanen, W.A. and H. Moritz, 1967. *Physical Geodesy*. W. H. Freeman & Co., San Francisco.

Marks, K.M., 1996. Resolution of the Scripps/NOAA marine gravity field from satellite altimetry. *Geophys. Res. Lett.*, **23**, 2069-2072.

Rummel, R., and R.H.N.Haagmans, 1990. Gravity gradients from satellite altimetry. *Marine Geodesy*, **14**, 1-12.

Sandwell, D.T., and W.H.F. Smith, 1997. Marine Gravity Anomaly from Geosat and ERS-1 Satellite Altimetry. *J. Geophys. Res.*, **102**, 10,039-10,054.

Sandwell, D.T., E.L. Winterer, J. Mammerickx, R.A. Duncan, M.A. Lynch, D.A. Levitt, and C.L. Johnson, 1995. Evidence for diffuse extension of the Pacific plate from Pukapuka ridges and cross-grain gravity lineations. *J. Geophys. Res.*, **100**, 15,087-15,099.

Scharroo, R., P. Visser, and G. Mets, 1997. TOPEX-class Orbits for the ERS Satellites. *J. Geophys. Res. (Oceans)*, **submitted**, ERS Special Section.

Wessel, P. and A.B. Watts, 1988. On the accuracy of marine gravity measurements. *J. Geophys. Res.*, **93**, 393-413.

Yale, M.M., D.T. Sandwell, and W.H.F Smith, 1995. Comparison of along-track resolution of stacked Geosat, ERS 1, and TOPEX satellite altimeters. *J.*

Geophys. Res., **100**, 15,117-15,127.

Appendix A

Evaluation of TOPEX Environmental Corrections

A.1 Introduction

I have performed an analysis of the environmental corrections supplied with TOPEX data to evaluate which corrections may be important when using sea surface slope data for marine gravity and oceanographic variability studies. Sea surface slope variability varies geographically. In the quietest oceanic regions, the variability is 1 μrad [*Sandwell and Zhang*, 1989]. If correction slopes exceed 0.5 μrad, they may significantly affect the resulting estimates of sea surface slope variability.

A.2 Procedure

For one cycle (cycle 17) of the TOPEX mission, I output the measurement time, latitude, longitude, and the slopes of the supplied environmental corrections including: ocean tide, solid earth tide, dry troposphere, wet troposphere, inverted barometer, ionosphere, electromagnetic bias (embias). The slope of each correc-

tion is the difference between corrections given each second, divided by 5.8 km. (Topex travels at 5.8 km/s over the ground.) I plot histograms of the absolute value of the slope of each correction. The correction slope amplitudes are then averaged in 1°x1° cells, and gridded to create maps showing the geographic distribution of areas with anomalously high correction slopes.

A.3 Evaluation

The only correction we must apply is the ocean tide. Slopes of the ocean tide correction exceed 2 μrad on most of the continental shelves (Figure A.1). In order to apply this correction, we must know the time of each measurement. We then use a global tide model to calculate the tidal corrections.

The maps and histograms for the solid earth tide (Figures A.3 and A.4), dry troposphere (Figures A.5 and A.6), wet troposphere (Figures A.7 and A.8), and inverted barometer (Figures A.9 and A.10) reveal that the amplitude of correction slopes for these environmental corrections are less than 0.5 μrad almost everywhere.

TOPEX has a dual frequency altimeter which is supposed to be capable of measuring the delay due to the ionosphere. The map of the ionosphere corrections slopes (Figure A.11) reveals a pattern that looks like a map of sea state. The ionosphere correction slopes are high at high latitudes, and lower in the calmer equatorial waters. In contrast the map of slopes of ionospheric corrections supplied by the Bent model of the ionosphere (Figure A.14) shows several bands of higher slope in the equatorial region where the electrojet causes a significant change in the number of electrons present in the ionosphere. In order to test whether the ionosphere slope corrections measured with the dual frequency altimeter are valid, I filtered the correction slopes with a 5 point boxcar filter, then mapped the correction slopes in the same way as previously. The map of

the filtered correction slopes is flat, with most correction slopes at or below 0.5 μrad (Figure A.13).

In order to measure the delay due to the ionosphere, the travel time must be measured very accurately at two different frequencies. When the sea state is rougher, the return pulses are scattered more, and the accuracy of the travel time determination is diminished.

The embias correction is also measured by modeling the returned waveform to determine the Significant Wave Height (SWH) (Figure A.16). As for the ionosphere, we filtered the embias correction slopes with a 5 point boxcar, and the map of the filtered correction slopes (Figure A.18 is flat with most correction slopes below 0.5 μrad.

In order to explain the strong latitudinal dependence of the ionosphere correction slopes and embias correction slopes in terms of electron content of the ionosphere and wave height, respectively, would require large changes over 5.8 km, consistently in regions of high sea state. It seems more likely that the high sea state decreases the measurement accuracy, and thus the corrections are poorly determined.

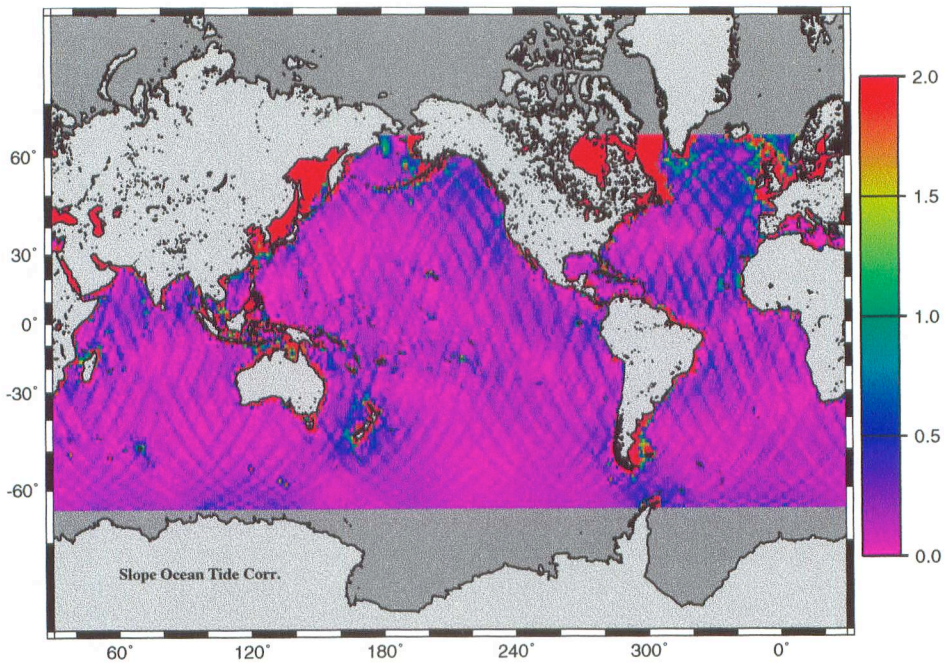

Figure A.1: Map of ocean tide correction slopes

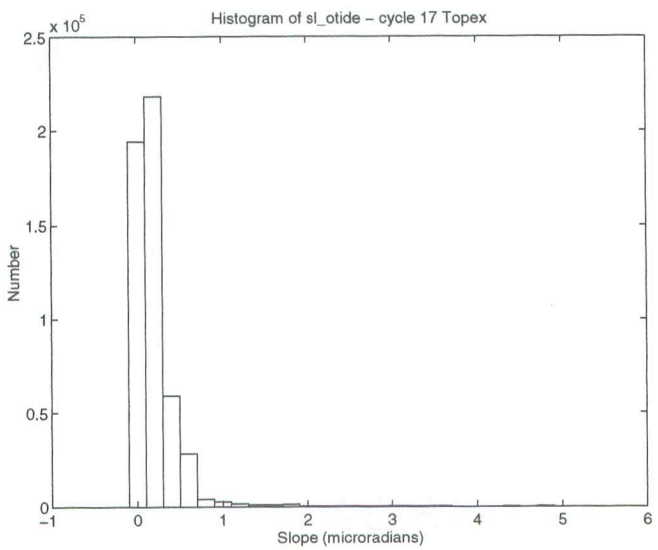

Figure A.2: Histogram of ocean tide correction slopes

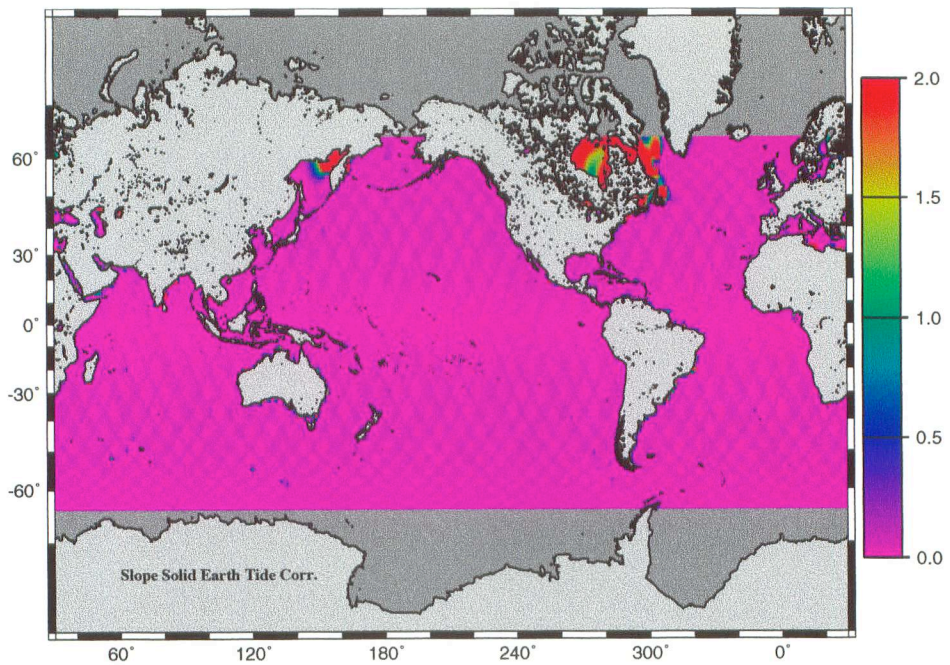

Figure A.3: Map of solid Earth tide correction slopes

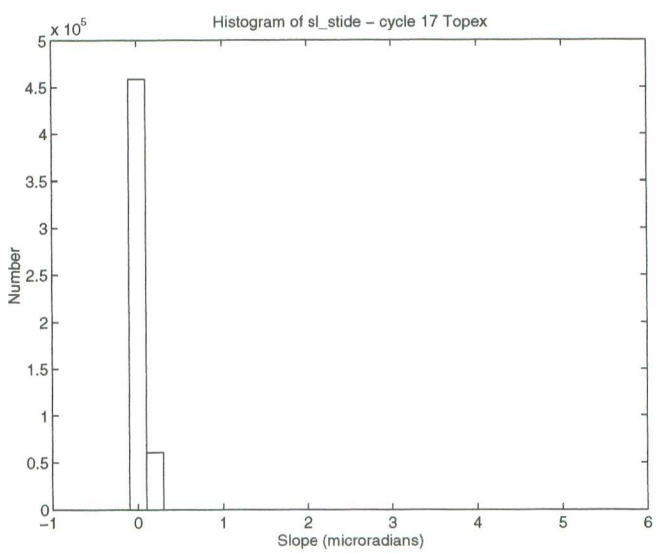

Figure A.4: Histogram of solid Earth tide correction slopes

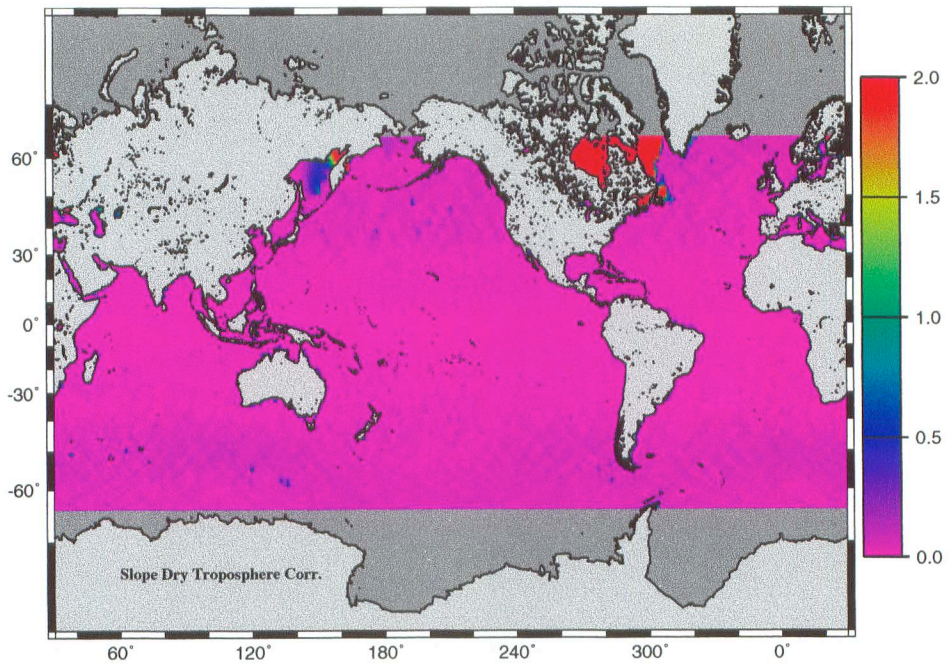

Figure A.5: Map of dry troposphere correction slopes

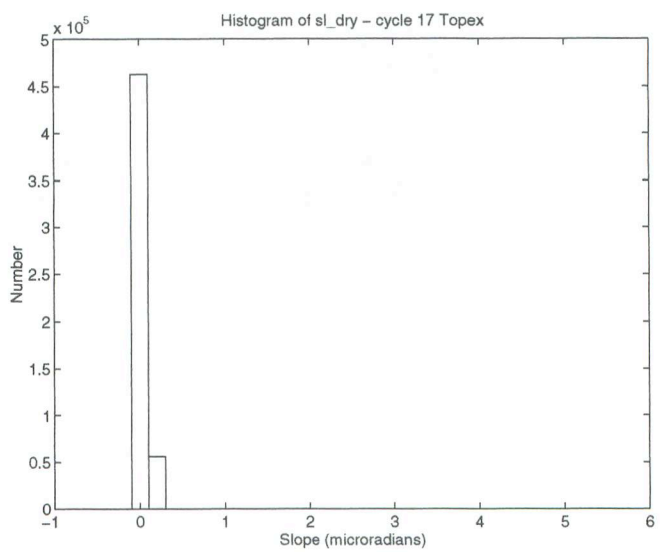

Figure A.6: Histogram of dry troposphere correction slopes

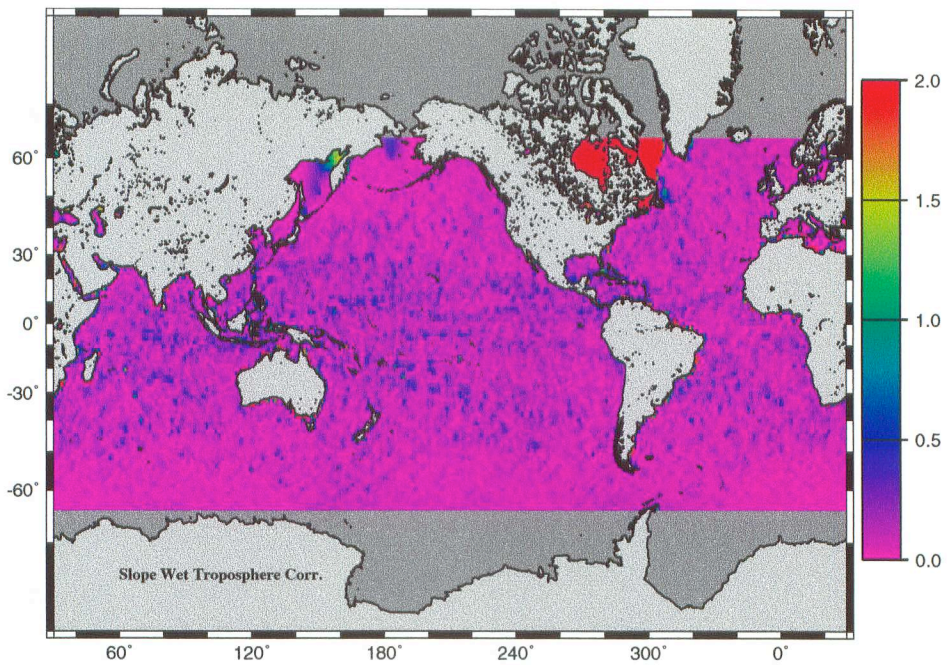

Figure A.7: Map of wet troposphere correction slopes

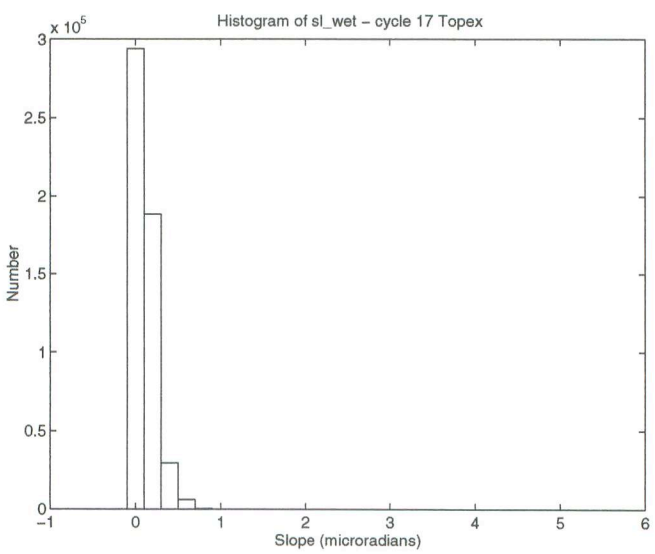

Figure A.8: Histogram of wet troposphere correction slopes

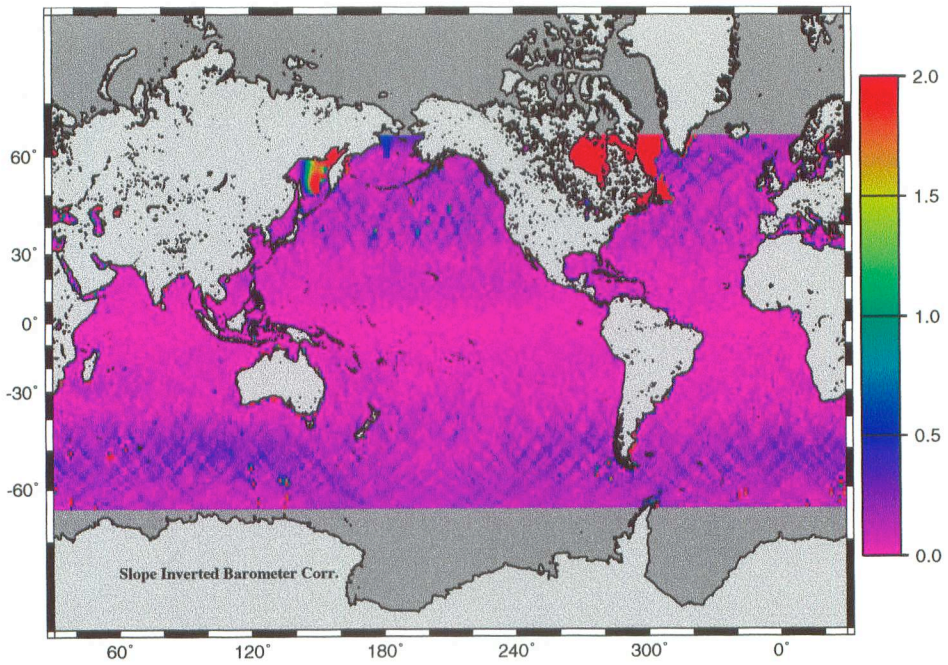

Figure A.9: Map of inverted barometer correction slopes

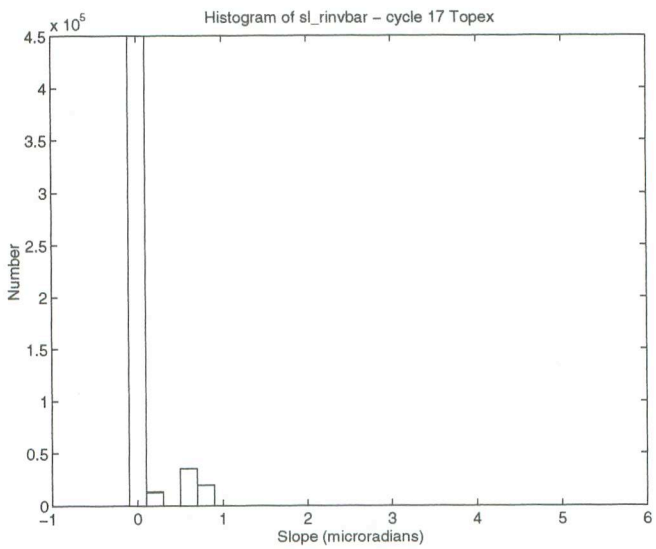

Figure A.10: Histogram of inverted barometer correction slopes

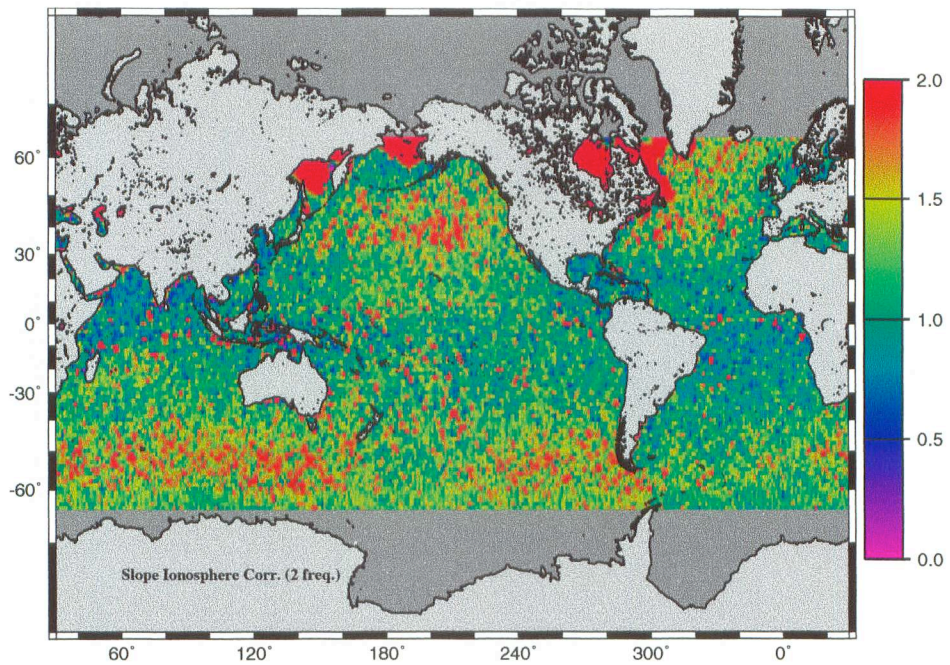

Figure A.11: Map of ionosphere correction slopes (TOPEX 2 freq.)

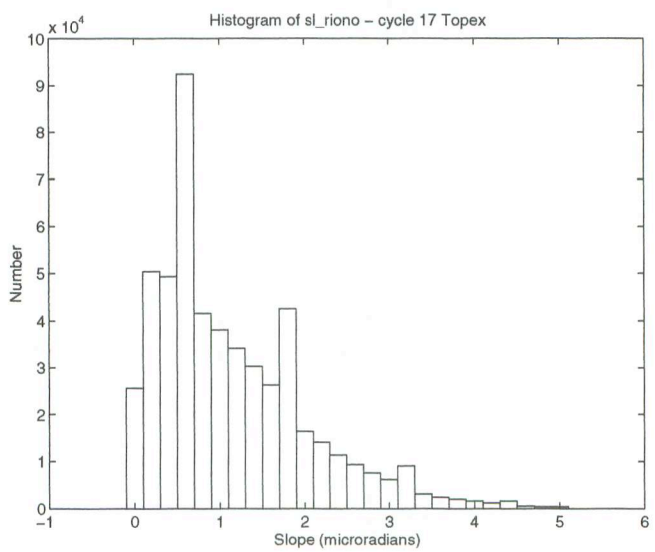

Figure A.12: Histogram of ionosphere correction slopes (TOPEX 2 freq.)

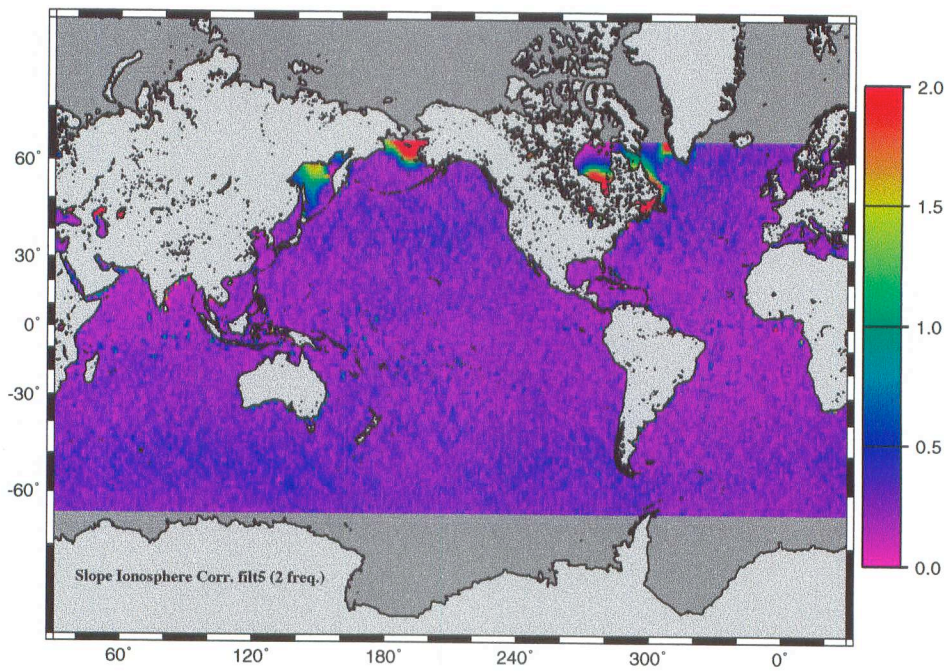

Figure A.13: Map of ionosphere correction slopes (TOPEX 2 freq.), filtered

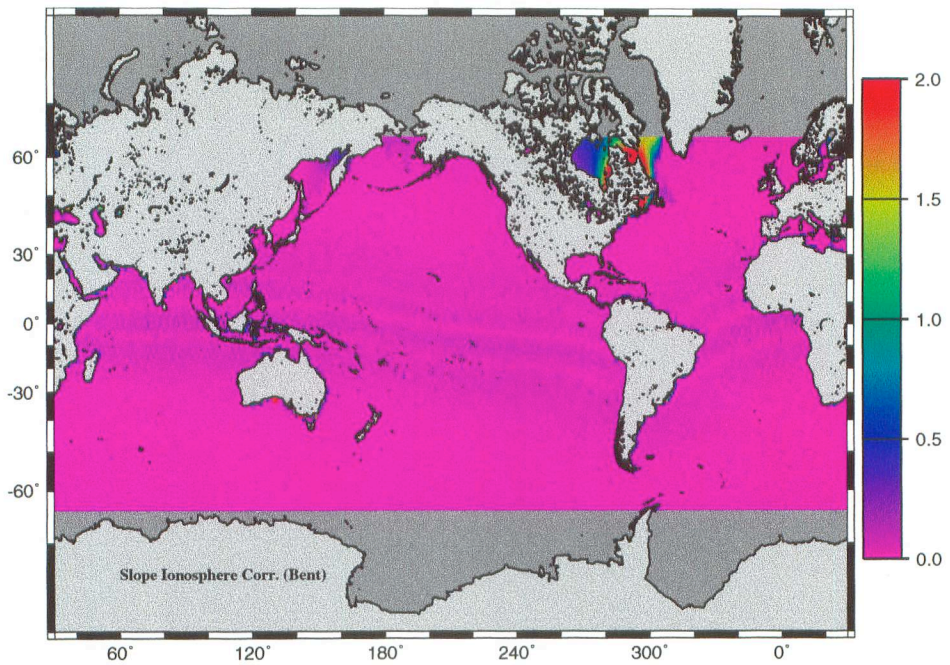

Figure A.14: Map of ionosphere correction slopes (Bent model)

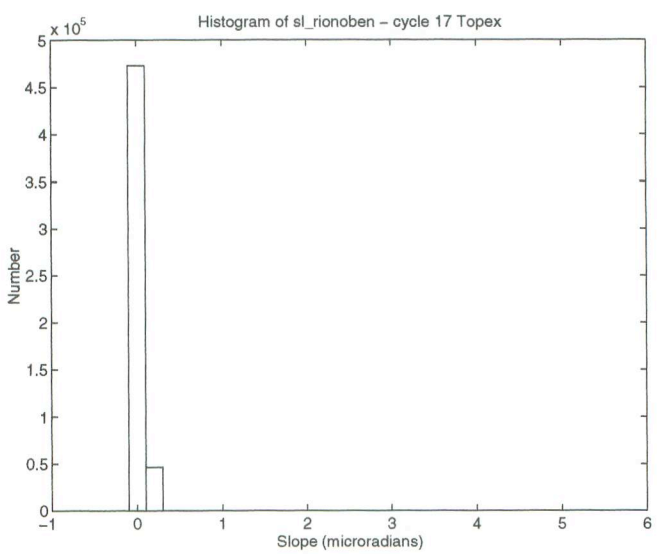

Figure A.15: Histogram of ionosphere correction slopes (Bent model)

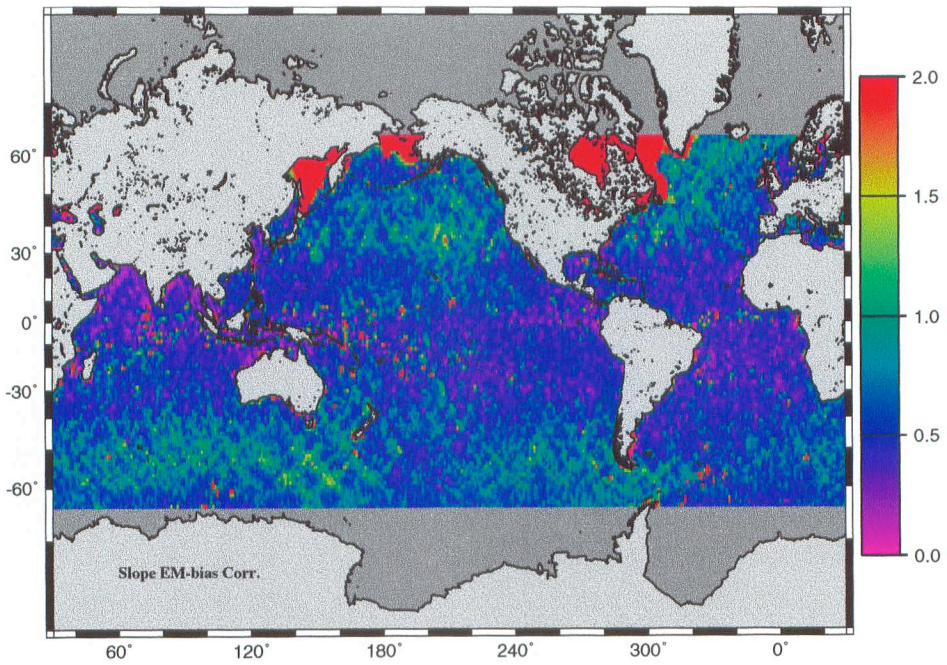

Figure A.16: Map of embias correction slopes

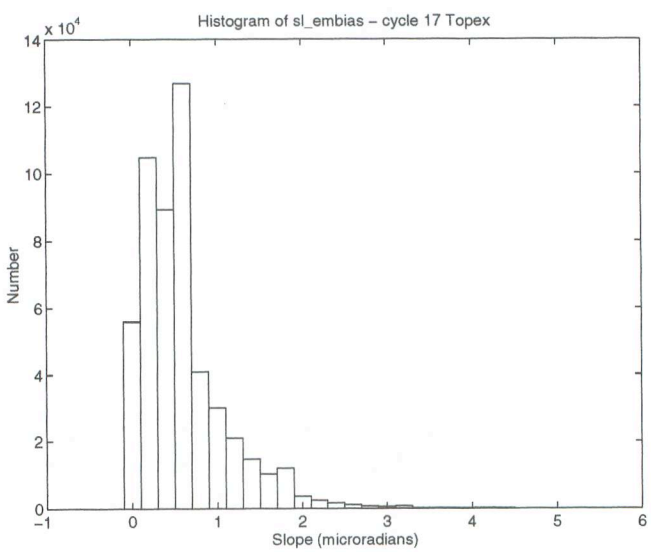

Figure A.17: Histogram of embias correction slopes

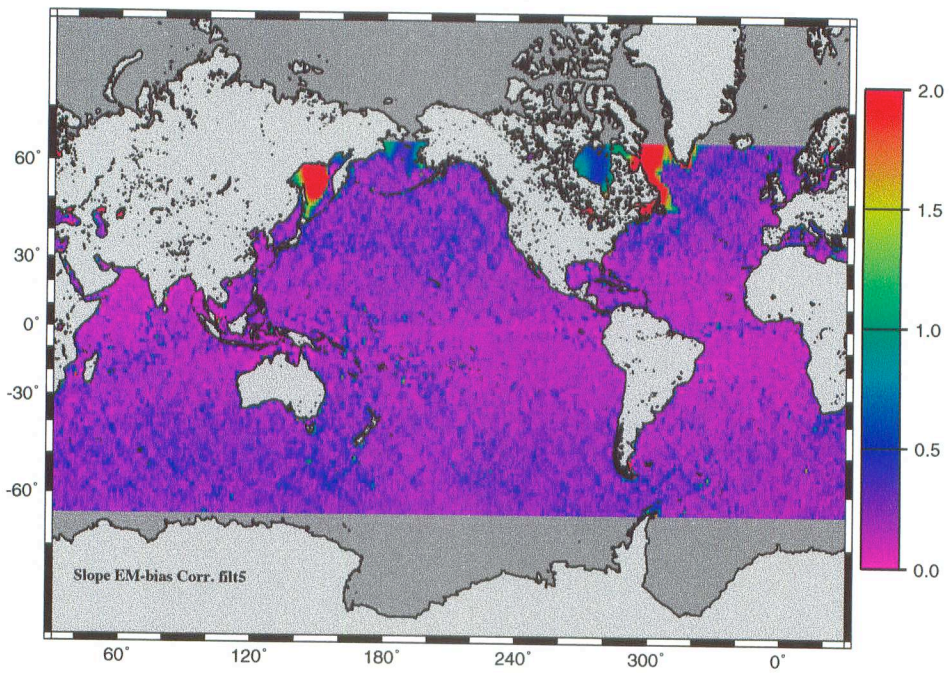

Figure A.18: Map of embias correction slopes, filtered

A.4 References

Sandwell, D. T. and B. Zhang, 1989. Global mesoscale variability from the Geosat Exact Repeat Mission: correlation with ocean depth. *J. Geophys. Res.*, **94**, 17,971-17,984.